UNIVERSITY OF
BIRMINGHAM

Modelling ice dynamic sea-level rise from the Antarctic Peninsula Ice Sheet

Clemens Schannwell

A thesis submitted to the University of Birmingham for the degree
of DOCTOR OF PHILOSOPHY.

School of Geography, Earth and Environmental Sciences
College of Life and Environmental Sciences
University of Birmingham
May 2017

Abstract

The Antarctic Peninsula (AP) has been one of the most rapidly warming regions on this planet. This warming has been accompanied by major glaciological changes such as tidewater glacier retreat, ice-shelf retreat and collapse alongside acceleration of outlet glaciers in response to ice-shelf removal. As faster flowing glaciers deliver more ice from the ice sheet's interior to the margins, the AP has been identified as an important contributor to global sea-level rise (SLR). However, comprehensive SLR projections of the AP induced by ice dynamics over the next three centuries are still lacking. The period to 2300 is selected as there are high quality climate forcing data available. This timeframe is also of particular interest for policy makers. In this thesis, numerical ice-sheet models are utilised to present scenario-based ice dynamic SLR projections for the AP.

A simple ice-sheet model specifically designed for the unique demands of the Antarctic Peninsula Ice Sheet (APIS) is employed in conjunction with parameterisations for grounding-line retreat and ice-shelf collapse timing to project SLR for the largest 199 ice-shelf tributary drainage basins. The employed scenario-based approach projects SLR of up to 9.4 mm by 2200, and up to 19 mm by 2300. The main contributor to SLR are outlet glaciers feeding George VI Ice Shelf, accounting for >75% of the total SLR in some model runs.

These results are then extended to include tidewater glacier contributions to provide ice-sheet-wide projections. Grounding-line and ice-shelf collapse parameterisations are updated to give an improved estimate of SLR projections. By including contributions from tidewater glaciers, SLR projections increase by a factor of at least two. Combined SLR projections to 2300 from the AP rise to between 11-32 mm, depending on the emission scenario.

The updated SLR projections are then compared with SLR projections from more sophisticated ice-sheet models for the Larsen C and George VI embayments. While all models agree well with each other in terms of absolute SLR projections by 2300, the simple ice-sheet model in conjunction with the statistical grounding-line retreat parameterisation fails to simulate the correct grounding-line retreat pattern in some areas. Simulations with the more sophisticated models under more realistic forcing reveal that there is very limited SLR potential from Larsen C Ice Shelf (<3 mm). Rather, George VI Ice Shelf holds the most SLR potential of all fringing ice shelves in the AP, contributing up to 22 mm to 2300 with even more ice at risk.

Acknowledgements

First and foremost I would like to thank my supervisor Nick Barrand for his continuous support and enthusiasm for this research. His guidance, ideas and encouragement over the last three years are greatly appreciated. I would also like to thank Richard Hindmarsh at the British Antarctic Survey (BAS) for allowing me to work with his ice-sheet model and for helping me to get my modelling career kickstarted.

Owing to Nick's constant encouragement, I had the opportunity to visit and work with some of the leading scientists in glaciology across the globe. Thanks to Valentina Radic for hosting me at the University of British Columbia (UBC), Canada, and for your advice on all issues related to climate data processing. As an ice-sheet modeller, you do not often go out to do fieldwork. So I am especially grateful to Noel, for letting me tag along onto fieldwork during my stay in Canada. This is what glaciology is really about. I am also deeply grateful to Steph Cornford at the University of Bristol and Dave Pollard at Pennsylvania State University for introducing me to and letting me use their state-of-the-art ice-sheet models. Thanks for answering all my pesky questions about ice-sheet modelling during my stay and your patience with my numerous follow-up questions later on.

I am also grateful to the School of Geography, Earth and Environmental Sciences (GEES) at the University of Birmingham for funding this PhD project. By joining GEES, I was lucky enough to meet many great people. Thanks to my officemates and friends in Birmingham, especially Tasos, Simon, Daniel, Leigh, Colin, Michael and the rest of the Bayern Abrantes team. You made the last three years a lot more pleasant. I am sure a piece of silverware is coming our way pretty soon.

Last but certainly not least, I would like to thank my parents and especially Daniela. This would all not have been possible without your unconditional support throughout the last three years and beyond.

Contents

Abstract i

Acknowledgements ii

Contents iii

List of acronyms v

List of figures vi

List of tables xi

List of mathematical symbols xii

1 Introduction 1
- 1.1 Thesis motivation and structure . . . 5
- 1.2 Ice sheet mass balance . . . 9
  - 1.2.1 Surface mass balance . . . 12
  - 1.2.2 Basal melting . . . 17
  - 1.2.3 Dynamics . . . 20
- 1.3 Ice-sheet modelling . . . 26
  - 1.3.1 Conservation laws . . . 28
  - 1.3.2 Force balance approximations . . . 31

2 Ice-dynamic sea-level rise projections from ice-shelf tributary glaciers 34
- 2.1 Introduction . . . 34
- 2.2 Methods . . . 40
  - 2.2.1 Ice-sheet model description . . . 40
  - 2.2.2 Climate forcing . . . 42
  - 2.2.3 Grounding-line retreat parameterisation . . . 48
  - 2.2.4 Experimental setup . . . 54
- 2.3 Results . . . 55
  - 2.3.1 Projected sea-level rise to 2200 . . . 56
  - 2.3.2 Projected sea-level rise to 2300 . . . 59
  - 2.3.3 Relevance of removed grounded ice . . . 61
  - 2.3.4 Regional ice dynamic thinning pattern . . . 62

2.3.5 Temporal partitioning of sea-level rise . . . 63
2.3.6 Steady state sea-level rise simulations . . . 66
2.4 Discussion . . . 67
2.4.1 Timing of ice-shelf collapse . . . 68
2.4.2 Grounding-line parameterisation . . . 69
2.5 Conclusions . . . 71

3 Future sea-level rise from tidewater and ice-shelf tributary glaciers of the Antarctic Peninsula 73
3.1 Introduction . . . 73
3.2 Data and methods . . . 76
3.2.1 Climate data and preprocessing . . . 76
3.2.2 Tidewater glaciers . . . 80
3.2.3 Ice-shelf tributary glaciers . . . 83
3.2.4 Model and experimental design . . . 88
3.3 Results and discussion . . . 88
3.3.1 Sea-level rise from tidewater glaciers . . . 88
3.3.2 Combined ice dynamical sea-level rise . . . 93
3.3.3 Uncertainty assessment . . . 97
3.4 Conclusions . . . 98

4 Sea-level projections from the Antarctic Peninsula Ice Sheet response to Larsen C and George VI ice shelf collapse 100
4.1 Introduction . . . 100
4.2 Methods . . . 103
4.2.1 Model description . . . 104
4.2.2 Experimental design . . . 106
4.2.3 Initialisation and spin up . . . 109
4.3 Results and discussion . . . 115
4.3.1 Experiment 1: Immediate ice-shelf collapse . . . 115
4.3.2 Experiment 2: Calving criterion . . . 123
4.4 Conclusions . . . 131

5 Conclusions 133
5.1 Summary of the main findings . . . 133
5.2 Limitations and scope for further research . . . 137

Bibliography 143

List of Acronyms

AIS	Antarctic ice sheet
AOGCM	atmopshere-ocean-gobal circulation model
AP	Antarctic Peninsula
APIS	Antarctic Peninsula Ice Sheet
ASS	Amundsen Sea Sector
BAS-APISM	British Antarctic Survey Antarctic Peninsula Ice Sheet Model
CDW	circumpolar deep water
CMIP5	Coupled Model Intercomparison Project Phase 5
DInSAR	differential satellite radar interferometry
DJF	December-January-February
EAIS	East Antarctic ice sheet
ECMWF	European Centre for Medium Range Weather Forecast
ERSST	Extended Reconstructed Sea Surface Temperature
FS	full-Stokes
GCM	global circulation model
GOC	global ocean circulation model
HD	horizontal dimension
HOM	higher order model
IPCC	Intergovernmental Panel on Climate Change
ISMIP6	Ice Sheet Model Intercomparison Project 6
LIMA	Landsat Image Mosaic Antarctica
masl	meter above sea level
MISI	marine ice sheet instability
MVLR	multivariate linear regression
PIG	Pine Island Glacier
PSU3D	Penn State University 3D
RCM	regional climate model
RCP	Representative Concentration Pathway
SIA	shallow-ice approximation
SLE	sea-level equivalent
SLR	sea-level rise
SMB	surface mass balance
SSA	shallow-shelf approximation
VNIR	visible and near-infrared
WAIS	West Antarctic ice sheet
w.e.	water equivalent

List of Figures

1.1 Recent mass balance estimates for the Antarctic ice sheet. Width of the box indicates the time period studied and height represents the error estimate. The citations for each estimate is given in the key. [Image credit: Luke Trusel [2015], `http://www.realclimate.org/index.php/archives/2015/11/so-what-is-really-happening-in-antarctica/`, 15.02.2017] . . 2

1.2 Overview map of Antarctica's different regions [Image credit: Hugo Ahlenius, UNEP/GRIP-Arendal [2007], `http://www.grida.no/graphicslib/detail/antarctica-topographic-map_8716`, 15.02.2017]. 3

1.3 Overview map of the Antarctic Peninsula with velocity map overlay *Rignot et al.* (2011a). Outlet glacier names including glacier type mentioned in the text are marked. Tidewater glaciers are defined as glaciers flowing directly into the sea and ice-shelf tributary glaciers are defined as flowing into floating ice shelves. 4

1.4 Schematic of the coupled ice sheet-ice shelf system (from *Huybrechts*, 2009). 10

1.5 Averaged SMB (1989-2009) from RACMO2 for the AIS in kg m^{-2} a^{-1}. Dashed lines represent surface elevation contours for every 500 m (from *van den Broeke et al.*, 2011). 13

1.6 Averaged SMB (1979-2014) from RACMO2.3 for the AP in mm w.e. a^{-1}. Dots represent markers for SMB observation locations. Inner black line approximates outline of grounded ice and outer black line of floating ice (from *van Wessem et al.*, 2016). . . . 15

1.7 Basal melt rates of Antarctic ice shelves overlaid on a 2009 Moderate Resolution Imaging Spectroradiometer mosaic of Antarctica. Each circle graph is proportional in area to the mass loss from each shelf, partitioned between iceberg calving (hatch fill) and basal melting (black fill) (from *Rignot et al.*, 2013). 18

1.8 Sketch of a marine ice sheet based on the geometry of Thwaites Glacier, West Antarctica. In upper panel, ice sheet is in equilibrium. In lower panel a small perturbation led to the ice sheet being engaged in MISI (from *Vaughan and Arthern*, 2007). 22

1.9 (a) Grounding-line flux q (red) and balance flux ax (blue) as a function of horizontal distance x. Vertical lines are steady state grounding lines (green for stable and yellow for unstable) and arrows indicate likely directions of the grounding line between the steady states. (b) Corresponding steady state ice sheet profiles (green for stable and red for unstable)[from *Joughin and Alley* (2011), adapted from *Schoof* (2007)]. 24
1.10 Flow regimes in an ice sheet-ice shelf system. In the grounded ice sheet vertical shear dominates, whereas in the floating ice shelf plug flow dominates. In the vicinity of the grounding line a transitional pattern is present (from *Greve and Blatter*, 2009). 28
1.11 Sketch of grounded ice flow regime (SIA), ice-shelf flow regime (SSA), and flow regime as modelled in hybrid models (SIA+SSA) or ice streams - grounded glaciers with very little basal drag (from *Kirchner et al.*, 2011). 33

2.1 Landsat Image Mosaic of Antarctica (LIMA) of AP region (`http://lima.usgs.gov/index.php`) with surface ice velocity from *Rignot et al.* (2011a) overlain. Red outlines depict 460 largest drainage basins, and black lines show ice shelf subdivisions. Map approximates ice sheet model domain. Lower left corner in polar stereographic coordinates is at -2611350, 239850 and upper right corner at -1304550, 1669050. 43
2.2 Smoothed (5-year running mean) mean annual near-surface air temperatures from 14 GCMs for ice-sheet model domain. Upper panel shows temperatures to 2100 for the (a) 'low emission' and (b) 'high emission' scenarios. Lower panel shows temperatures to 2300 for the (c) 'low emission' and (d) 'high emission' scenarios. A full list of GCMs can be found under: `http://cmip-pcmdi.llnl.gov/cmip5/citation.html`. 44
2.3 Ice-shelf collapse timing derived using the -5°C isotherm for all 10 ice-shelf entities. Ice-shelf abbreviations are as follows: LB = Larsen B Ice Shelf, LCN = Larsen C Ice Shelf North, LCS = Larsen C Ice Shelf South, LDN = Larsen D Ice Shelf North, LDC = Larsen D Ice Shelf Central, LDS = Larsen D Ice Shelf South, GVIN = George VI Ice Shelf North, GVIC = George VI Ice Shelf Central, GVIS = George VI Ice Shelf South, STA = Stange Ice Shelf 45
2.4 Ice-shelf collapse timing derived using the -9°C isotherm for all 10 ice-shelf entities. Ice-shelf abbreviations are the same as in Figure 2.3. 46
2.5 (a) Map as in Figure 2.1, including 'Location' variable (pink). Red cross approximates location of inset map. Inset map shows sample drainage basin of area (black) used for velocity acceleration in statistical model. (b) Displays initial acceleration curve with triangles approximating the starting position of basin acceleration curves in (d). (c) Shows the distribution of residuals of the MVLR. 53

2.6 SLR curves to 2200, forced by using the -5°C isotherm (a-c) and -9°C isotherm (d-f) for RCP4.5 emission scenario. Crosses denote multi-model mean ice-shelf collapse timings. Black line shows multi-model mean SLR curve. SLR projections from individual GCMs have the same colour as in Figure 2.3. 57
2.7 SLR curves to 2200, forced by using the -5°C isotherm (a-c) and -9°C isotherm (d-f) for RCP8.5 emission scenario. Crosses denote multi-model mean ice-shelf collapse timings. Black line shows multi-model mean SLR curve. SLR projections from individual GCMs have the same colour as in Figure 2.3. 58
2.8 SLR curves to 2300, forced by using the -5°C isotherm (a-c) and -9°C isotherm (d-f) for RCP4.5 emission scenario. Crosses denote multi-model mean ice-shelf collapse timings. Black line shows multi-model mean SLR curve. SLR projections from individual GCMs have the same colour as in Figure 2.3. 60
2.9 SLR curves to 2300, forced by using the -5°C isotherm (a-c) and -9°C isotherm (d-f) for RCP8.5 emission scenario. Crosses denote multi-model mean ice-shelf collapse timings. Black line shows multi-model mean SLR curve. SLR projections from individual GCMs have the same colour as in Figure 2.3. 61
2.10 Multi-model mean thinning pattern using the high emission scenario and (a) the -5°C isotherm and (b) -9°C isotherm. Black boxes approximate location of inset map. 63
2.11 Temporal partitioning of SLR from the coldest (upper two panels) and warmest (lower two panels) GCM runs to 2200, using the -9°C isotherm high emission scenario with no running mean. 64
2.12 Temporal partitioning of SLR from the coldest (upper two panels) and warmest (lower two panels) GCM runs to 2300, using the -9°C isotherm high emission scenario with no running mean. 65

3.1 Near-surface temperature bias in comparison to ERA Interim from 1979-2005. Dashed black line indicates multi-model mean (2.0±2.6°C). 77
3.2 Location map of the AP and meteorological stations. Full names and details are provided in Table 3.1. Climate stations are denoted with a bullseye symbol, automatic weather stations with an unfilled circle symbol. Limbert station is off the map and not displayed (adapted from *Barrand et al.*, 2013a). 79
3.3 Ocean temperature bias in comparison to ERSST v4 from 1979-2005 for each GCM. Dashed black line indicates multi-model mean (-0.6±0.7°C). 80
3.4 (a) Gamma distributions used in grounding-line retreat parameterisation for different mean adjustment times (M_{ad}). (b) Sample of 100 random step-response functions for corresponding $M_{ad} = 20$ curve in (a). 85
3.5 Multi-model mean ocean temperatures for the ice-sheet model domain for RCP4.5 (blue line) and RCP8.5 (red line). Shading shows ($\pm 1\sigma$) uncertainty. 89

3.6 SLR projection from tidewater glaciers permitting calving front retreat to 2100 (a) and to 2300 (b). Shading shows ($\pm 1\sigma$) uncertainty. 90
3.7 Multi-model mean melt day projections for all ice shelves for the RCP4.5 (solid blue line) and RCP8.5 (solid red line) scenarios. Shading shows ($\pm 1\sigma$) uncertainty. Dashed blue lines and dashed red lines denote ice-shelf collapse timing for the RCP4.5 and RCP8.5 scenarios, respectively. Dashed black line approximates collapse threshold. Note that for Larsen B Ice Shelf (Scar Inlet) collapse timing for both scenarios is forecasted for the same year. The dip in melt days at 2100 is due to a number of GCM projections only extending to 2100. 92
3.8 Combined SLR for RCP4.5 (a) and RCP8.5 (b) scenarios. Red and blue lines correspond to combined maximum and combined minimum projection. Dashed blue lines approximate timing of ice-shelf collapse. Error bars are displayed where available. 94

4.1 (a) Location map of the AP including locations of Larsen C and George VI ice shelves and localities mentioned (adapted from *Barrand et al.*, 2013a). (b) Bedrock elevations below sea level for the AP from BEDMAP2 (*Fretwell et al.*, 2013). Black polygons denote ice-sheet model domains. Grey boxes approximate locations of zoom-ins. 102
4.2 Near-surface temperature bias for the baseline period 1980-2005 in GCMs for RCP4.5 projections. Dashed black line indicates multi-model mean (-3.1±2.0°C). The selected forcing is highlighted by the red box. 107
4.3 Near-surface temperature bias for the baseline period 1980-2005 in GCMs for the RCP8.5 projections. Dashed black line indicates multi-model mean (-2.8±1.7°C). The selected forcing is highlighted by the red box. 108
4.4 L-curve analysis to select Tikhonov parameters λ_ϕ and λ_C: (a) 3-D scatter plot of the model-data misfit J_m as a function of the regularisation terms J_C^{reg} and J_ϕ^{reg}. (b) 2-D cross section for variable λ_ϕ and λ_C fixed at 10^{-1} Pa^{-2} m^6 a^{-4}. (c) Reverse case with constant λ_ϕ at 10^9 m^4 a^{-2} and λ_C varying. The units of J_m and J_C^{reg} are m^4 a^{-2} and Pa^2 m^{-2} a^2, respectively. J_ϕ^{reg} is unitless. Selected values are highlighted by red circles in (b) and (c). 110
4.5 Inferred basal traction fields C for the Larsen C (a,b) and George VI model domains (c,d). The black polygons show the respective drainage basin. Location of maps is approximated by grey boxes in Figure 4.1. 112
4.6 $\frac{\partial V}{\partial t}$ spin-up plot for BISICLES (solid lines) and PSU3D (dashed lines) at different horizontal resolutions. 114

4.7 Upper panel (a,b) shows SLR projections for BISICLES (solid lines), PSU3D (dashed lines), and BAS-APISM (dotted line). Lower panel (c,d) shows the derivative (rate of change) of the corresponding SLR projections in the upper panel (a,b). Grey shading displays uncertainty associated with SLR projections from BAS-APISM. Note different y-axis scales. 116
4.8 Dynamic thinning pattern averaged over the simulation period for the Larsen C embayment in (a) BAS-APISM, (b) PSU3D, and (c) BISICLES. 118
4.9 Dynamic thinning pattern averaged over the simulation period for the George VI embayment in (a) BAS-APISM, (b) PSU3D, and (c) BISICLES. 119
4.10 SLR projections for Larsen C (a) and George VI ice shelves (b) with corresponding area loss of grounded ice (c,d) and ice shelf area loss (e,f). 124
4.11 Comparison of modelled grounding-line positions for RCP8.5 scenario for Larsen C (a) and George VI embayments (b). Black outlines show drainage basins. 125
4.12 Dynamic thinning pattern averaged over the simulation period in the RCP8.5 scenario for Larsen C (a,c) and George VI embayments (b,d). Black outlines show drainage basins. 127
4.13 SLR projections using different basal sliding laws (a,b). Lower panel (c,d) shows the derivative (rate of change) of the corresponding SLR projections in the upper panel (a,b). Note different y-axis scales. . . 130
4.14 Comparison of modelled grounding-line positions with different basal sliding laws for Larsen C (a) and George VI embayments (b). Black outlines show drainage basins. 131

List of Tables

2.1 List of multivariate linear regression predictor variables for the AP grounding-line retreat parameterisation. Rank lists predictor variables in terms of their importance to overall model fit. 49

3.1 List of weather stations used to compute the statistical lapse rate. Exact locations are shown in Figure 3.2. Heights are in masl. Model Height refers to the elevation of the ERA-Interim pixel closest to the respective station. AWS = Automatic Weather Station. 78

3.2 Ice-shelf grounding-line retreat distances, mean buttressing factor (Θ), and the number of basins for each ice shelf entity. 87

4.1 Comparison of simulated grounding-line retreat at seven sample glaciers. Locations of glaciers are shown in Figure 1.3. GLCW = Gibbs-Lammers-Cole-Weyerhause glacier complex. 122

List of Mathematical Symbols

α_0	y-axis intercept
β_i	regression coefficient
ϵ_i	residual or prediction error
$\dot{\epsilon}$	longitudinal strain rate
η	ice viscosity
κ_i	thermal conductivity of ice
λ_C	Tikhonov parameter
λ_ϕ	Tikhonov parameter
Ω	Earth angular velocity
Φ	internal frictional heating
ρ_i	ice density
ρ_w	ocean water density
ρ_0	density of surface liquid
σ	Cauchy stress tensor
τ	deviatoric stress tensor
Θ	buttressing factor
Θ_γ	gamma distribution shape parameter

a	friction coefficient in Coulomb sliding law
$\bar{A}$	depth averaged rheological coefficient
b	bedrock elevation
BMB	basal melting
c_p	heat capacity of ice
C	basal drag coefficient
CMB	calving loss
$\frac{\mathrm{d}}{\mathrm{d}t}$	material derivative
d_b	depth of basal crevasses
d_s	depth of surface crevasses
d_w	water height in surface crevasse
D	strain-rate tensor
D_w	water depth at calving front
e_{si}	specific internal energy
ER_{ds}	erosion of drifting snow
f_h	heat flux vector
FC	modelled thickness change over a single time step
FMB	face melt loss
g	gravitational acceleration
h	ice thickness
h_{ab}	thickness above flotation
h_f	flotation thickness

h_{gl}	ice thickness at grounding line
H_c	critical thickness
J	objective function
J_m	misfit function
J_p	Tikhonov penalty function
J_C^{reg}	spatial gradient of C
J_ϕ^{reg}	spatial gradient of ϕ
k	gamma distribution shape parameter
m	Schoof flux formula exponent
M	ice mass
M_{ad}	mean adjustment time
M_a	annual surface accumulation
M_b	annual basal mass balance
M_c	annual calving mass loss
M_m	annual surface runoff mass loss
MB	synthetic mass balance
∇	nabla operator
n	Glenn's flow law exponent
$\vec{n}_{gl}$	unit normal to the grounding line
N	normal pressure in presence of ice shelf
N_0	ocean pressure whithout ice shelf present
N_e	effective pressure

OMB	oceanic sub-ice melting or freezing
P	precipitation
q	ice flux
q_{bgl}	buttressed grounding-line flux
q_{gl}	unbuttressed grounding-line flux
Q_{in}	ice discharge into the domain
Q_{out}	ice discharge out of domain
r	specific radiation power
R	melt available to fill surface crevasses
RU	meltwater runoff
s	surface elevation
SMB	annual surface mass balance
SU_{ds}	sublimation due to drifting snow
SU_s	surface sublimation
t	time
$tr()$	trace operator
T	ice temperature
T_o	ocean temperature
$\vec{u}$	2D horizontal velocity
u	ice velocity in x-direction
$\bar{u}$	column averaged velocity in x-direction
$\vec{v}$	3D velocity vector

v	ice velocity in y-direction
$\bar{v}$	column averaged velocity in y-direction
V_c	calving rate
x_{gl}	grounding-line retreat
X_i	predictor variable
z	ice velocity in z-direction

Chapter 1

Introduction

The Antarctic ice sheet (AIS) holds 61% of the planet's freshwater and thus presents the by far largest potential to raise global sea level. It covers an area of ∼14 million km^2 and holds ∼27 million m^3 of ice. This volume is equivalent to filling the Mediterranean Sea ∼7 times. If the AIS melted completely it would raise global sea level by ∼58 m (*Fretwell et al.*, 2013). Given this sea-level rise (SLR) potential, there is an increasing interest in whether the AIS is losing or gaining mass at the moment (e.g. *Shepherd et al.*, 2012; *Zwally et al.*, 2015; *Martín-Español et al.*, 2016). While there is a consensus that the second largest ice sheet on this planet - the Greenland ice sheet - is losing mass at an increasing rate (e.g *Enderlin et al.*, 2014; *Shfaqat et al.*, 2015), the situation is less clear for the AIS (e.g. *Shepherd et al.*, 2012; *Zwally et al.*, 2015; *Martín-Español et al.*, 2016). Even though the agreement between different ice-sheet-wide measurement techniques has improved in recent years (*Hanna et al.*, 2013), there is still a considerable spread across and within measurement techniques (Figure 1.1).

To extract information about the spatial mass balance pattern, the AIS is commonly divided into three regions (Figure 1.2): the West Antarctic ice sheet (WAIS), the East Antarctic ice sheet (EAIS), and the Antarctic Peninsula (AP). Despite

the observed spread (Figure 1.1), Antarctic mass balance studies generally agree on the broad spatial pattern, with the WAIS and AP losing mass and the EAIS gaining mass (e.g. *Shepherd et al.*, 2012; *Zwally et al.*, 2015; *Martín-Español et al.*, 2016). The exact magnitude of these gain/loss patterns however remain somewhat uncertain (e.g. *Zwally et al.*, 2015; *Martín-Español et al.*, 2016).

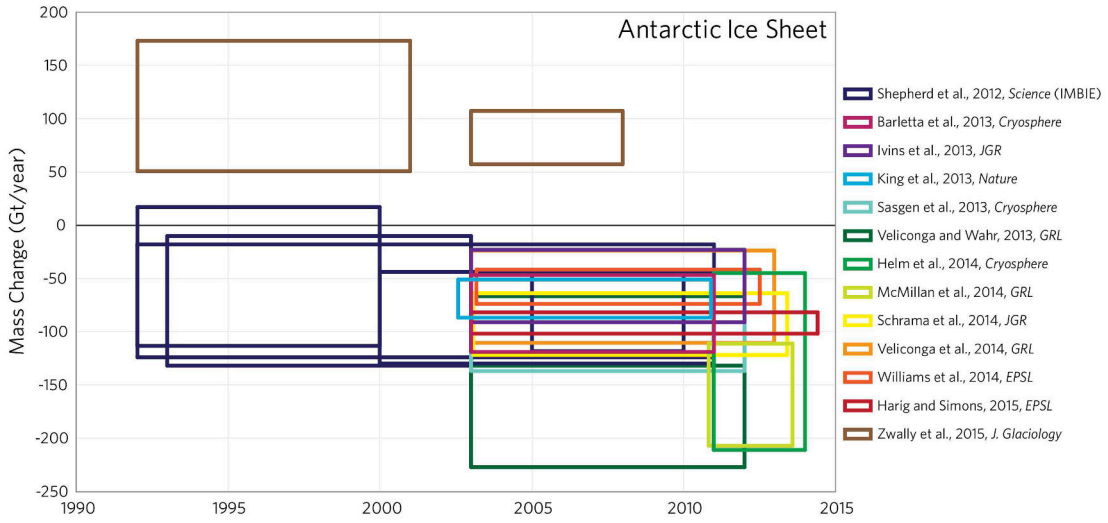

Figure 1.1: Recent mass balance estimates for the Antarctic ice sheet. Width of the box indicates the time period studied and height represents the error estimate. The citations for each estimate is given in the key. [Image credit: Luke Trusel [2015], `http://www.realclimate.org/index.php/archives/2015/11/so-what-is-really-happening-in-antarctica/`, 15.02.2017]

As part of an intercomparison between the different measurement techniques - radar altimetry, laser altimetry, input-output method, and gravimetry - *Shepherd et al.* (2012) estimate that the AIS contributed 0.2±0.15 mm a^{-1} to global SLR between 1992-2011. SLR contributions were moderate at 0.13±0.18 mm a^{-1} in the early part of the study period, but increased to 0.23±0.1 mm a^{-1} between 2005-2010. Ice loss hotspots are the Amundsen Sea Sector (ASS) in West Antarctica and the AP (e.g. *Shepherd et al.*, 2012; *Martín-Español et al.*, 2016). The observed accelerating

mass loss in these two regions is not due to increased surface melt, but instead has been attributed to a speed-up of outlet glaciers, resulting in an increased discharge of ice to the sea (e.g. *Martín-Español et al.*, 2016).

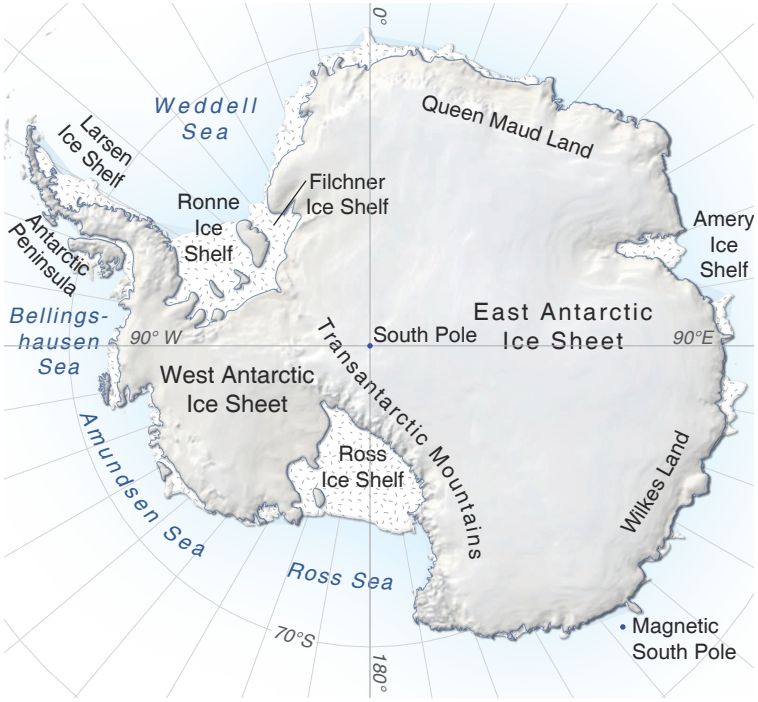

Figure 1.2: Overview map of Antarctica's different regions [Image credit: Hugo Ahlenius, UNEP/GRIP-Arendal [2007], `http://www.grida.no/graphicslib/detail/antarctica-topographic-map_8716`, 15.02.2017].

Despite only occupying 4% of the total AIS area (Figure 1.2), the AP is a major contributor to SLR, contributing ∼25% of the ice sheet's total mass loss (*Shepherd et al.*, 2012). Until the early 2000's, the AP was close to balance, but subsequent glaciological changes such as the collapse of Larsen B Ice Shelf (e.g. *Scambos et al.*, 2003), have led to the increasing contribution. While the northern AP was responsible for most of the SLR from this region between 2000-2007 (*Martín-Español et al.*, 2016), the spatial mass loss pattern has changed considerably in more recent years with the southern AP being the more dominant contributor (*Wouters et al.*,

2015; *Martín-Español et al.*, 2016), adding 0.16±0.02 mm a^{-1} to global SLR since 2009 (*Wouters et al.*, 2015).

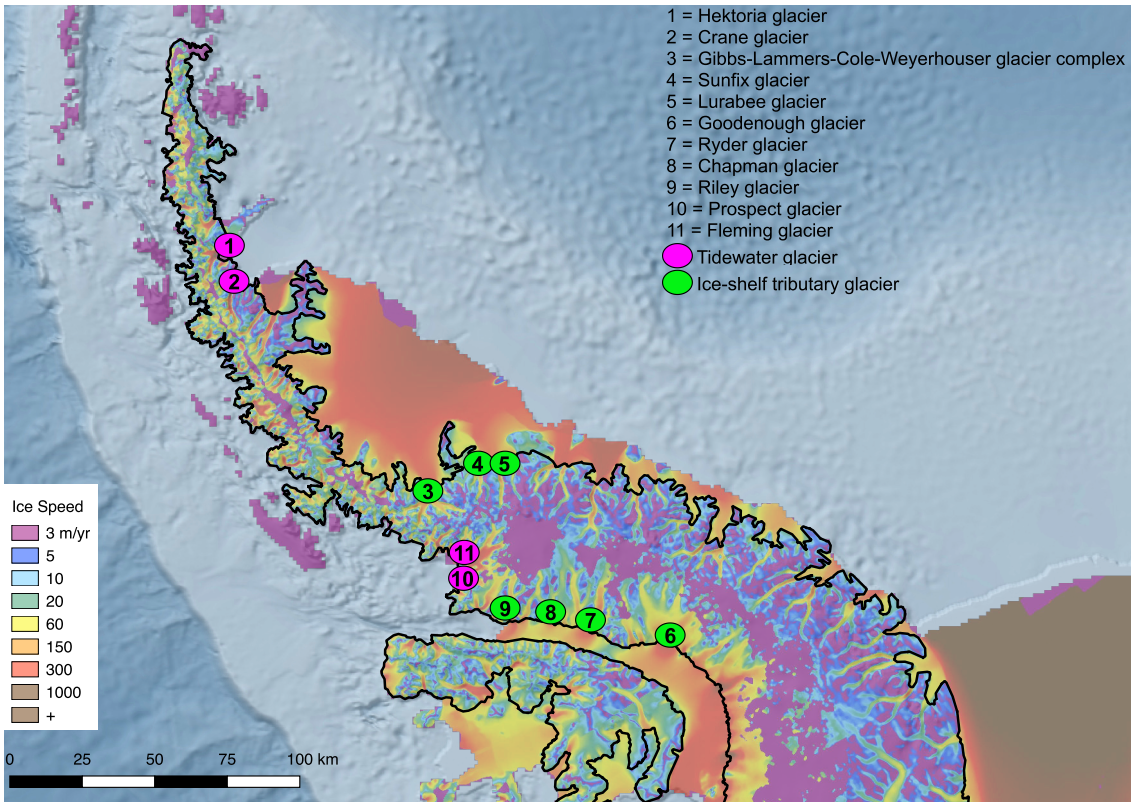

Figure 1.3: Overview map of the Antarctic Peninsula with velocity map overlay *Rignot et al.* (2011a). Outlet glacier names including glacier type mentioned in the text are marked. Tidewater glaciers are defined as glaciers flowing directly into the sea and ice-shelf tributary glaciers are defined as flowing into floating ice shelves.

1.1 Thesis motivation and structure

As a result of ice-shelf collapse events in the recent past (e.g. *Scambos et al.*, 2003), grounded ice upstream has accelerated, leading to an increased contribution to SLR (*Martín-Español et al.*, 2016), making the peninsula one of the largest contributor to SLR in Antarctica (*Shepherd et al.*, 2012; *Martín-Español et al.*, 2016). Based on observations, this increasing trend has even accelerated in more recent years (e.g. *Wouters et al.*, 2015). SLR contributions of the region are dominated by ice dynamics (*Martín-Español et al.*, 2016; *Wouters et al.*, 2015), while SMB has remained stable over the last four decades (*Lenaerts et al.*, 2012; *van Wessem et al.*, 2016). With more warming projected over the next centuries, further ice-shelf collapse and more ice dynamic SLR from the Antarctic Peninsula Ice Sheet (APIS) may be expected. Projections of ice dynamic SLR have been focussed on the ASS (*Favier et al.*, 2014; *Joughin et al.*, 2014) with very few and only simple projections existing for the AP, to date (e.g. *Barrand et al.*, 2013b). Motivated by the lack of projections, the primary goal of this thesis is to quantify the ice dynamic SLR from APIS to 2300. This forecasting period was selected for two reasons: i) high quality climate data is available to 2300 and; ii) this timeframe is of particular interest for policy makers (e.g. through the Intergovernmental Panel on Climate Change (IPCC)). While the primary goal of this work has potentially far reaching consequences for densely populated areas located close to current coastlines, this thesis also aims to answer more glaciology focused research questions:

1. What is the upper bound for ice dynamic SLR contribution from the Antarctic Peninsula Ice Sheet (APIS) to 2300?

2. Which of the fringing ice shelves of the Antarctic Peninsula (AP) holds the highest potential for ice dynamic SLR?

3. Do the smaller tidewater glaciers in the north and west of the peninsula matter for ice dynamic SLR projections?

4. Can a simple but computationally cheap ice-sheet model produce similar result to more sophisticated ice-sheet models

The main tool to address these research questions is numerical ice-sheet modelling. To provide forcing to the models for future simulations, model outputs from global ocean circulation models (GOCs) and global circulation models (GCMs) are used. The next paragraphs describe in more detail the structure and motivation of the thesis' main chapters. Each of the chapters is designed to answer at least one of the questions raised above and they all contribute towards the primary goal of quantifying the ice dynamic SLR to 2300 from APIS.

The remainder of the first chapter is dedicated to introduce the main concepts on which the three experimental chapters (Chapters 2-4) are based. Firstly, the ice-sheet mass balance equation is presented, followed by a review of the main balance terms (SMB, basal melting, and ice dynamics) and their significance for Antarctica and the AP in particular. As this work's focus is on ice dynamic SLR, a more in depth introduction is given to ice dynamics. The last part of the first chapter is used to present the relevant equations for ice-sheet modelling and the various approximations that are utilised by the three ice-sheet models employed in this work. This should facilitate comparison between the ice-sheet models and highlights advantages and disadvantages of the various ice-flow approximations.

The main body of the thesis consists of three main experimental chapters (Chapters 2-4), followed by a conclusion chapter (Chapter 5) which summarises the key findings and discusses the scope for future work. In each of the three experimental chapters, the relevant literature is reviewed, and descriptions of the numerical ice-sheet models and forcing data, as well as methodology details, are provided. The research presented in this thesis has previously been published in the '*Journal*

of Geophysical Research - Earth Surface' (*Schannwell et al.*, 2015), and '*Earth and Planetary Science Letters*' (*Schannwell et al.*, 2016). These two publications compose Chapters 2 and 3, respectively. Chapter 4 is currently in preparation for publication. As different people contributed to each of the main experimental chapters, the following paragraph highlights the contribution from the author of this PhD thesis to each of the chapters.

In Chapters 2 and 3, the study was designed by Clemens Schannwell and Nicholas Barrand. Valentina Radic helped with the climate data processing and provided the initial mean monthly temperature datasets. Parameterisations of grounding-line retreat and ice-shelf collapse were developed by Clemens Schannwell. All simulations were carried out by Clemens Schannwell. The manuscript was written by Clemens Schannwell with Nicholas Barrand and Valentina Radic both contributing to the writing. In Chapter 4, Clemens Schannwell and Nick Barrand conceived the study and experiments. David Pollard and Stephen Cornford helped setting-up their respective ice-sheet model on the local cluster in Birmingham, UK. Clemens Schannwell carried out all simulations and did the climate data processing. The manuscript was written by Clemens Schannwell with comments from Nicholas Barrand, David Pollard, and Stephen Cornford significantly improving the initial version of the manuscript.

Chapter 2 builds on previous work by *Barrand et al.* (2013b) but increases the spatial coverage of the AP by increasing the modelled drainage basins from 20 to 199 drainage basins. In addition, more realistic forcing is used in the experiments. This chapter provides a first estimate of SLR projections from ice-shelf tributary glaciers from the AP to 2300 and gives an indication which of the fringing ice shelves holds the most ice dynamic SLR potential. The simple but computationally cheap ice-sheet model BAS-APISM is used to project ice dynamic SLR contribution from the 199 largest ice-shelf tributary drainage basins. As this ice-sheet model is based on the SIA and thus not capable of simulating the coupled sheet-shelf system,

a statistical model is presented to estimate grounding-line retreat in response to ice-shelf collapse. Ice-shelf collapse is estimated by tracking a pair of thermal viability limits in an ensemble of GCM projections for Representative Concentration Pathways (RCP)4.5 and 8.5. This approach provides a series of scenario-based projections for the AP to 2300.

Chapter 3 builds on the study presented in Chapter 2. Major improvements to the grounding-line parameterisation and ice-shelf collapse timing are presented. These improvements make the parameterisations more process-based and are derived from theoretical ice dynamics considerations. The ice-sheet model BAS-APISM is used to compute SLR projections. A new statistical framework for estimating grounding-line retreat in response to ice-shelf collapse is introduced. This approach scales the retreat to the amount of buttressing at the ice front for each drainage basins. Ice-shelf collapse timing is not determined by tracking thermal viability limits, but is instead based on the total number of melt days in a calendar year - a more direct and physically-based parameterisation. In addition to the 199 ice-shelf tributary glaciers modelled, the projections also include the 235 largest tidewater glaciers. This allows the evaluation of the importance of SLR contributions from tidewater glaciers against contributions from ice-shelf tributary glaciers. Moreover, due to the increased spatial coverage an upper bound for ice dynamic SLR can be presented.

Chapter 4 compares SLR projections for the Larsen C and George VI ice shelf embayments computed with the simple BAS-APISM to projections from two state-of-the-art ice sheet-ice shelf models (PSU3D, BISICLES), capable of simulating the full sheet-shelf system. Larsen C ice shelf was selected for the model intercomparison because it is hypothesised to be under the most immediate threat of collapsing. George VI ice shelf was chosen because of its marine-based sectors which may be susceptible to MISI. In addition to the model intercomparison, this chapter presents results from the sheet-shelf system with more realistic forcing where ice-shelf collapse and subsequent tidewater glacier retreat is forced with a physically-based

calving relation (*Benn et al.*, 2007a). This experimental set-up permits the investigation of ice dynamics processes that the simple ice-sheet model BAS-APISM is not able to simulate due to the implemented ice-flow approximation. Additionally, conclusions can be drawn as to how important these processes are for ice-dynamic SLR projections and how well the grounding-line parameterisation works across the pensinula.

Chapter 5 presents a summary of the main conclusions drawn from the studies in Chapters 2-4. This is followed by a discussion of the limitations of the presented research and also offers scope for future work.

1.2 Ice sheet mass balance

The AIS consists of two distinct zones. The largest part is supported at the bottom by different types of bedrock material and is referred to as ice sheet. When the ice sheet reaches the ocean and starts to float according to Archimedes' principle, an ice shelf is formed. Large parts of the AIS are fringed by ice shelves. The transition point at which the ice sheet starts to float is called the grounding line (Figure 1.4). Most of the AIS is fringed by ice shelves. The point at which the ice becomes afloat is called the grounding line. Often assumed to be a distinct boundary for simplicity, this grounding zone can span several kilometers in reality (*Brunt et al.*, 2010). The grounding zone is defined as the region of the ice sheet where conditions vary from grounded ice sheet to freely floating ice shelf e.g. through tidal forcing (*Brunt et al.*, 2010).

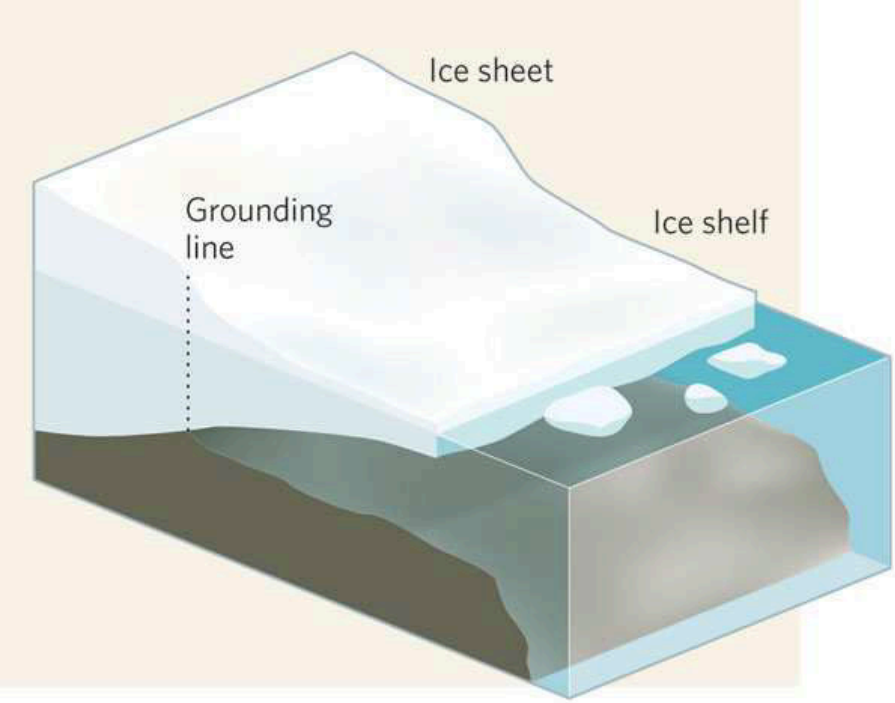

Figure 1.4: Schematic of the coupled ice sheet-ice shelf system (from *Huybrechts*, 2009).

In order to estimate SLR contributions from ice sheets such as the AIS, their mass balance needs to be determined. Mass balance is defined as the net product of mass gains and mass losses (*Hagen and Reeh*, 2004; *Cuffey and Paterson*, 2010). Ice-sheet-wide this can be determined by integrating the local mass balance over the total area of the ice sheet and subtracting the loss through potential vertical boundaries such as calving fronts. This can be expressed as

$$\frac{\partial M}{\partial t} = M_a - M_m - M_c \pm M_b \tag{1.1}$$

where M is ice mass, t is time usually taken as one year, M_a is the annual surface accumulation, M_m is the annual loss due to surface runoff, M_c is the annual loss due to calving of icebergs, and M_b is the annual balance at the base of the ice sheet (*Hagen and Reeh*, 2004). The terms M_a and M_m are commonly combined to

represent the surface mass balance (SMB), simplifying equation 1.1 to

$$\frac{\partial M}{\partial t} = SMB - M_c \pm M_b \tag{1.2}$$

In the grounded ice sheet, the basal mass balance (M_b), commonly assumed to be equal to the geothermal heat flux, is often neglected as mass balance is dominated by SMB and ice discharge to the ocean (M_c or often D for discharge). This simplification cannot be made for ice shelves where the basal mass balance plays a pivotal role for the overall mass budget (e.g. *Pritchard et al.*, 2012; *Rignot et al.*, 2013). However, any mass loss from ice shelves has negligible direct ramifications for SLR as the ice already displaces its own weight of ocean water. For the mass balance of an ice shelf only, ignoring any mass loss from the grounded ice, equation 1.2 needs to be modified to account for the ice influx at the grounding line from the grounded ice sheet. This equation then reads

$$\frac{\partial M}{\partial t} = SMB - Q_{out} + Q_{in} \pm M_b \tag{1.3}$$

where Q_{out} is the calving flux denoted by M_c before, and Q_{in} is the influx of ice at the grounding line from the grounded ice.

From equations 1.1-1.3 it can be seen that an ice sheet-ice shelf system can lose mass through three main processes: a negative SMB, an increase in ice discharge (D or M_c), and a negative basal mass balance. The next sections will review the importance of each of these processes to the overall mass budget of the AIS with a special focus on the AP. Only the mass balance of the coupled ice sheet-ice shelf system is considered in this thesis.

1.2.1 Surface mass balance

One potential source for mass loss of the AIS is due to a negative SMB (equation 1.2). The SMB is defined as the sum of surface accumulation (M_a in equation 1.1) and surface ablation (M_m in equation 1.1). On smaller glaciers and ice caps, this quantity can be measured *in situ*, but on a continental scale the SMB is commonly deduced from global or regional climate models (*van de Berg et al.*, 2006; *van den Broeke et al.*, 2011; *Lenaerts et al.*, 2012). Other methods such as passive microwave emissions of snow accumulation (assuming no ablation) have also been used (*Arthern et al.*, 2006; *Vaughan et al.*, 1999). However, early SMB estimate efforts for the AIS were solely based on the interpolation of *in situ* measurements (e.g. *Giovinetto*, 1985; *Giovinetto et al.*, 1989). These SMB maps provided first insights into the spatial variability of the SMB across the AIS. One of the shortcomings of these maps was that only a long-term averaged snapshot of the ice-sheet-wide SMB was presented. Moreover, most *in situ* measurements are near the Antarctic coastline, making SMB interpolations for the interior highly uncertain (e.g. *Arthern et al.*, 2006). Even today the paucity of *in situ* SMB measurements in the interior still presents a challenge for SMB model validation (*van de Berg et al.*, 2006; *van Wessem et al.*, 2016).

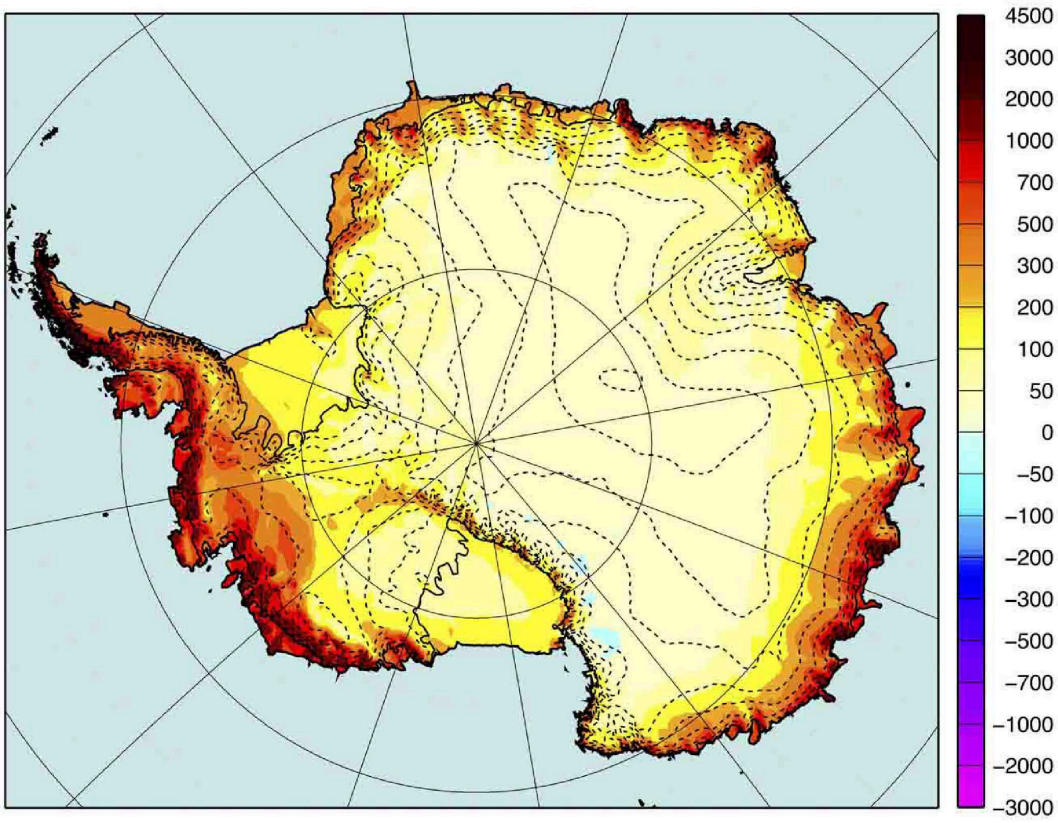

Figure 1.5: Averaged SMB (1989-2009) from RACMO2 for the AIS in kg m^{-2} a^{-1}. Dashed lines represent surface elevation contours for every 500 m (from *van den Broeke et al.*, 2011).

In order to provide SMB fields, SMB models solve the surface energy balance equation:

$$SMB = \int_{year} (P - SU_s - RU - ER_{ds} - SU_{ds})dt \tag{1.4}$$

where P is precipitation (snow and rain), SU_s is surface sublimation, RU is meltwater runoff, ER_{ds} is erosion by drifting snow, and SU_{ds} represents sublimation due to drifting snow (e.g. *Lenaerts et al.*, 2012; *Ligtenberg et al.*, 2013; *van Wessem et al.*, 2016). All of the previous SMB maps (e.g. *Bromwich et al.*, 2004; *van de Berg et al.*, 2006; *Arthern et al.*, 2006; *Lenaerts et al.*, 2012), including those based on *in situ* measurements (e.g. *Giovinetto*, 1985; *Giovinetto et al.*, 1989; *Giovinetto and Zwally*, 2000), reveal the same broad-scale SMB pattern for the AIS. Precipitation

is highest near the coastline, but decrease within a few hundred kilometers of the coastline to <500 mm water equivalent (w.e.). (Figure 1.5). Zones of high accumulation (>1000 mm w.e.) are located in the AP region and in coastal West Antarctica (e.g. *Lenaerts et al.*, 2012). The integrated ice-sheet-wide SMB lies between 2288-2572 Gt a^{-1} depending on the method and study period (*Vaughan et al.*, 1999; *Giovinetto and Zwally*, 2000; *Bromwich et al.*, 2004; *van de Berg et al.*, 2006; *Arthern et al.*, 2006; *Lenaerts et al.*, 2012), making the SMB, or more precisely snowfall, the most important mass input to the AIS. In comparison to snowfall (P in equation 1.4), all other components of the surface energy balance equation are of secondary importance (*Ligtenberg et al.*, 2013). On the continental scale there is very little melt (<0.5% of the AIS), with the AP the only region to have significant surface melt. On intra-annual and inter-annual timescales, snowfall is highly variable, but between 1979-2010 the ice-sheet integrated SMB has shown no significant trends (*Lenaerts et al.*, 2012). This lack of a trend in the SMB is expected to change in the future. SMB projections with the regional climate model (RCM) RACMO suggest snowfall is likely to increase by up to 550 Gt a^{-1} by 2200 (*Ligtenberg et al.*, 2013), resulting in a sea-level drop of up to 120 mm over the next two centuries. The main reason for this projected rise is the increased water vapor holding capacity of the Antarctic atmosphere due to the expected warming. This is in accordance with the Clausius-Clapeyron relation that gives an increase of 7 % K^{-1} (*Held and Soden*, 2006). In response to the warming, rainfall, snowmelt, and sublimation are also projected to increase, but the rise is an order of magnitude smaller than for snowfall. This trend of increasing snowfall with warming temperature is assumed to be valid for a temperature increase ∼6 K from present (*Ligtenberg et al.*, 2013). Beyond this temperature range, the trend may be reversed and snowmelt and sublimation may become the dominant terms in the surface energy balance equation (*DeConto and Pollard*, 2016).

As for the entire AIS, SMB for the Peninsula is dominated by precipitation (*van*

Lipzig et al., 2004; *van Wessem et al.*, 2016). Due to its mountainous topography, there are areas on the western side of the peninsula with extreme precipitation rates of up to 5000 mm w.e. a^{-1}, equivalent to ∼15 m of snowfall each year (*van Wessem et al.*, 2016). The mountain chain forming the spine of the AP provides a barrier that is almost perpendicular to the prevalent circumpolar westerlies, resulting in strong east-west gradients in SMB (*Turner et al.*, 2002; *van Wessem et al.*, 2016). While highest SMB values are observed on the upwind western side owing to orographic precipitation, SMB values on the downwind side drop to <300 mm w.e. a^{-1} (Figure 1.6).

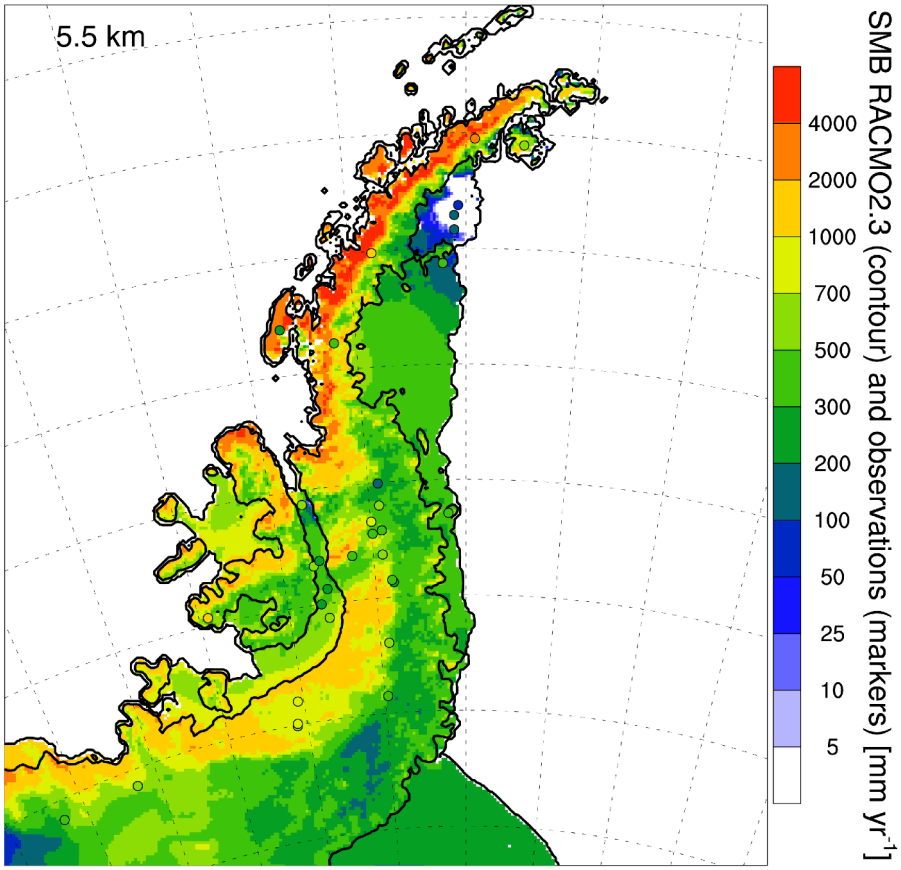

Figure 1.6: Averaged SMB (1979-2014) from RACMO2.3 for the AP in mm w.e. a^{-1}. Dots represent markers for SMB observation locations. Inner black line approximates outline of grounded ice and outer black line of floating ice (from *van Wessem et al.*, 2016).

Unlike the rest of the AIS, the AP's northerly location leads to widespread snow melt below 2000 meters above sea level (masl), with maxima of up to 500 mm w.e. a^{-1} over the north-eastern ice shelves. However, most of this meltwater refreezes in the snowpack and only a fraction is lost to the ocean as surface runoff (*van Wessem et al.*, 2016). The integrated SMB for the AP lies between 280-351 Gt a^{-1} (*van Lipzig et al.*, 2004; *van Wessem et al.*, 2016), accounting between ∼10-20% of the AIS-wide SMB. The spatial pattern of SMB follows the spatial pattern of snowfall and all other terms in equation 1.4 are of lesser importance. This is reflected in the integrated SMB for the western AP and the eastern AP. The SMB for the western AP (276±47 Gt a^{-1}) is ∼4 times larger than the SMB for the eastern AP (75±11 Gt a^{-1}). On inter-annual timescales, snowmelt and snowfall show high variability. No significant trend in the SMB was found for the entire AP between 1979-2014, but locally strong trends exist e.g. on Alexander Island (*Lenaerts et al.*, 2012; *van Wessem et al.*, 2016). In response to the expected continuing warming over the next centuries, SMB modelling (*Ligtenberg et al.*, 2013) as well as coupled ice sheet-SMB modelling (*Barrand et al.*, 2013b) studies suggest a negative contribution to SLR from the AP, as SMB projections are dominated by an increase in accumulation (*Ligtenberg et al.*, 2013; *Barrand et al.*, 2013b). However, the spread among the climate models is quite large, ranging from ∼0-18 mm of sea-level drop to 2200 (*Barrand et al.*, 2013b). Moreover, the horizontal resolution of the climate model used for the projections was 55 km which is adequate for the AIS, but may be underresolving the mountainous topography of the AP. It is important to note that these model projections are based on the SMB only and do not consider changes in ice dynamics. The effects of ice dynamics on the overall mass budget will be reviewed in the next sections.

1.2.2 Basal melting

For the grounded ice sheet, basal melting presents a negligible source of mass loss with the exception of areas with high geothermal heat flux (*Alley et al.*, 2015) . For ice shelves however, basal melting plays a direct and crucial role for their respective mass budget. As ice shelves are already afloat, the only SLR contribution from mass loss of ice shelves is due to the density difference between meteoric ice and freshwater (*Shepherd et al.*, 2010). Thus, the SLR from all Antarctic ice shelves due to either iceberg calving or thickness changes is small, with 6.3±3.0 μm a^{-1} between 1994-2004 (*Shepherd et al.*, 2010).

Ice shelves provide an important interface between the AIS and the surrounding ocean. Approximately 80% of Antarctic ice is drained through ice shelves (*Pritchard et al.*, 2012). Ice shelves are often contained in embayments and although mostly afloat, run aground on ice rises, ice rumples or islands. These pinning points and drag from side walls provide a backforce commonly referred to as buttressing in glaciology. This buttressing force modulates the flow of the grounded ice upstream by restraining ice flow across the grounding line (*Schoof* , 2007; *Goldberg et al.*, 2009). As ice shelves thin through basal melting, they detach from these local pinning points and buttressing is reduced, often leading to acceleration of the grounded ice upstream. Therefore, even though the direct contribution to SLR through basal melting is small, it still influences the grounded ice upstream and hence global SLR. Up until a few years ago, it was commonly believed that iceberg calving was the most dominant ablation process for ice shelves, with basal melting only contributing between 10-28% of the total mass loss (*Jacobs et al.*, 1992; *Cuffey and Paterson*, 2010; *Rignot et al.*, 2013). Based on the concept of mass conservation, *Rignot et al.* (2013) showed that instead of iceberg calving, basal melting is the most important ablation process (Figure 1.7). According to this study, ice shelves around Antarctica lose about 1325±235 Gt a^{-1} due to basal melting and 1089±139 Gt a^{-1}

through iceberg calving. This equals an average thinning rate from basal melting of 0.85±0.1 m a^{-1} across all ice shelves. Highest melt rates occur in the AP region and West Antarctica (Figure 1.7), where basal melting underneath some ice shelves accounts for >75% of the total mass loss (*Rignot et al.*, 2013; *Depoorter et al.*, 2013).

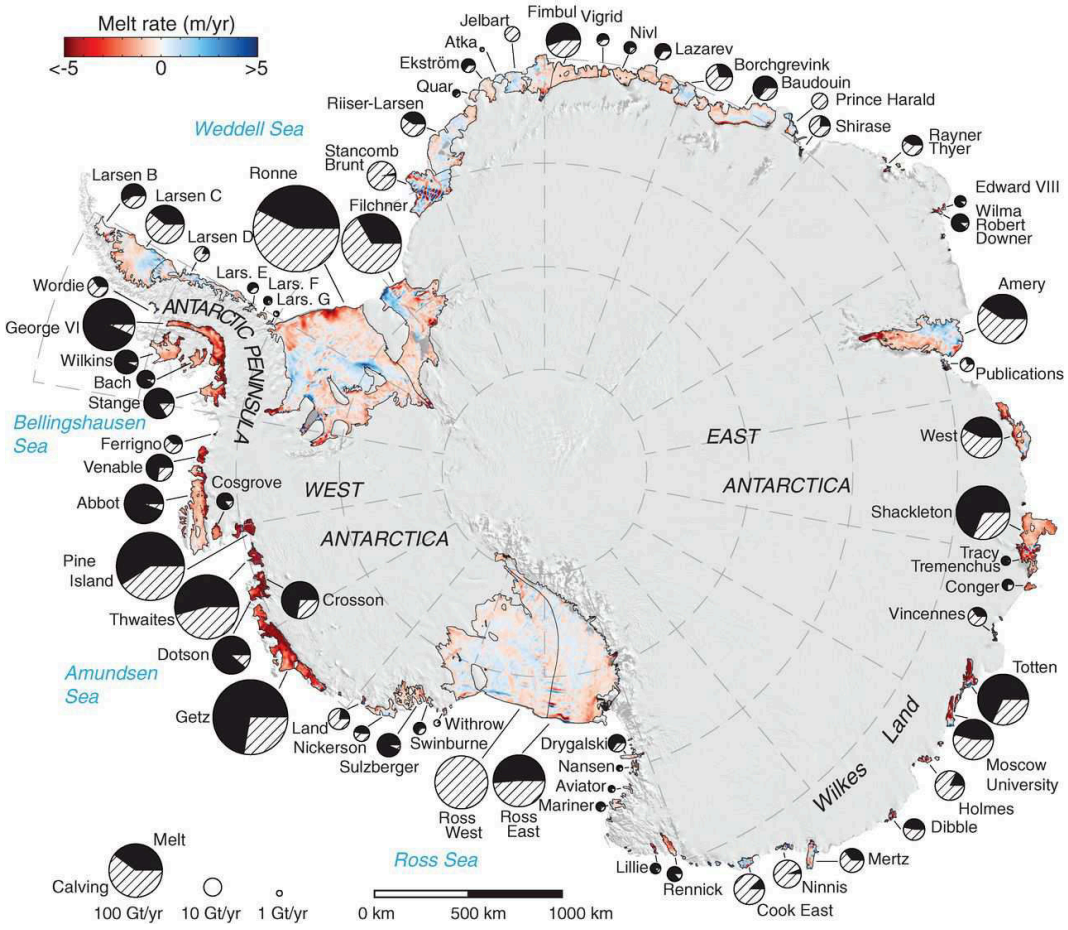

Figure 1.7: Basal melt rates of Antarctic ice shelves overlaid on a 2009 Moderate Resolution Imaging Spectroradiometer mosaic of Antarctica. Each circle graph is proportional in area to the mass loss from each shelf, partitioned between iceberg calving (hatch fill) and basal melting (black fill) (from *Rignot et al.*, 2013).

Under individual ice shelves basal melt is highest near the grounding lines (e.g. *Payne et al.*, 2007) and decreases away from the grounding line, even turning

negative, leading to accretion of ice on some ice shelves (*Rignot et al.*, 2013; *McGrath et al.*, 2014; *Kulessa et al.*, 2014). High basal melt rates are associated with more heat supply (*Holland et al.*, 2008; *Pritchard et al.*, 2012; *Rignot et al.*, 2013). Heat is often supplied by incursions of circumpolar deep water (CDW) onto the continental shelf (*Holland et al.*, 2008; *Pritchard et al.*, 2012). This water mass is characterised by its relative warm temperatures (>1°C), high salinity and high density. Most susceptible to these CDW incursions are areas located at the head of deep bathymetric troughs. At depths deeper than ∼300 m, the CDW can be up to 4°C above freezing, resulting in very high basal melt rates in these regions. For example, melt rates near the grounding line at Pine Island Glacier (PIG), West Antarctica, can reach values of ∼100 m a^{-1} (*Payne et al.*, 2007). The magnitude of basal melt rates caused by the delivery of warm CDW to the shelf can however vary considerably over intra-annual and inter-annual timescales (*Thoma et al.*, 2008). This is due to the fact that CDW flow to the inner shelf has been linked to regional wind forcing and atmospheric circulation which can vary over time, providing more or less favourable conditions for CDW incursion to take place (*Thoma et al.*, 2008; *Pritchard et al.*, 2012).

It is projected that ocean temperatures are likely to increase by 0.5-0.6°C to 2200 for Antarctica, delivering even more heat to ice shelves and potentially leading to a significant increase in ice mass loss as a result (*Yin et al.*, 2011; *DeConto and Pollard*, 2016). Warming is expected to be highest for West Antarctica where a warming of 1°C is projected (*Yin et al.*, 2011). The projected warming is however highly dependent on the emission scenario chosen and the model selection. Moreover, due to the coarse spatial resolution of the fully coupled atmosphere-ocean-global climate model (AOGCM), the models used for the projections are not capable to resolve ocean temperatures on a local to regional scale (*Yin et al.*, 2011; *DeConto and Pollard*, 2016).

Basal melt rates in the AP are significantly higher than the Antarctica-wide average.

The average thinning for all AP ice shelves through basal melt is 1.5±0.6 m a^{-1} (*Rignot et al.*, 2013). Ice shelves experiencing the highest basal melt rates are Wordie Ice Shelf and George VI Ice Shelf with thinning rates of 23.6±10 m a^{-1} and 3.8±0.7 m a^{-1}, respectively. Overall, ice shelves on the eastern side exhibit much lower basal melt rates then their counterparts on the western side. The reason for this spatially heterogeneous melt pattern is that warm water very rarely enters the ice-shelf cavity on the eastern side of the AP e.g. Larsen C Ice Shelf (*Nicholls et al.*, 2004, 2012; *Holland et al.*, 2015). Observations of widespread marine ice accretion under Larsen C Ice Shelf suggest that these conditions have been prevalent for some time (*McGrath et al.*, 2014; *Holland et al.*, 2015). In contrast to this, CDW with a temperature in excess of 1°C floods the entire cavities on the western ice shelves (e.g. George VI Ice Shelf), supplying heat to drive vigorous basal melting (*Jenkins and Jacobs*, 2008). These high basal melt rates have led to an imbalance of most ice shelves on the western side of the AP, resulting in significant surface lowering and thinning in this region (*Fricker and Padman*, 2012; *Paolo et al.*, 2015). While projections of ocean temperatures on the local to regional scale are still lacking, simulations from AOGCMs indicate that ocean temperature and thus basal melt rates should increase over the course of the next few centuries (*Yin et al.*, 2011; *DeConto and Pollard*, 2016). This trend may have already started in the second half of the 20th century, during which near surface ocean temperatures have risen by >1°C (*Meredith and King*, 2005).

1.2.3 Dynamics

As briefly mentioned in section 1.2.2, fringing ice shelves provide a certain backstress (henceforth buttressing) that is transmitted upstream to the grounded ice (*Schoof*, 2007; *Goldberg et al.*, 2009; *Fürst et al.*, 2016). This ice-shelf buttressing restrains ice flow across the grounding line and is defined as the mechanical effect of an ice shelf

on the state of stress at the grounding line (*Gudmundsson*, 2013). Buttressing can originate from shearing or marginal stress between an ice shelf and its embayment walls (*Thomas et al.*, 2004; *Borstad et al.*, 2013; *Fürst et al.*, 2016) or areas where it runs locally aground (e.g. ice rises, ice rumples and islands). In theory, for a freely floating ice shelf without any pinning points or drag from side walls, the buttressing force would be zero. This means mass loss from such an ice shelf would not have any effect on the grounded ice upstream (*Schoof*, 2007; *Gudmundsson*, 2013). In reality, however, ice shelves always provide some buttressing to the grounded ice. Due to the observed thinning of ice shelves in the recent past (*Fricker and Padman*, 2012; *Rignot et al.*, 2013; *Paolo et al.*, 2015), the buttressing force of these ice shelves has diminished. In the light of more projected warming (e.g. *DeConto and Pollard*, 2016), this trend is expected to continue over the next centuries. In response to the reduced buttressing, grounded ice upstream has accelerated, thinned, and is discharging more ice into the ocean, contributing directly to global SLR (e.g. *Rott et al.*, 2011; *Scambos et al.*, 2014; *Mouginot et al.*, 2014; *Wouters et al.*, 2015). Thinning at the grounding line may lead to its retreat, resulting in a loss of basal friction underneath formerly grounded ice, causing even more acceleration (*Joughin and Alley*, 2011). This type of SLR contribution is the main focus of this thesis and will be referred to throughout the work as 'ice dynamic SLR contribution'.

This process is the single most contributing source to global SLR from the AIS at the moment. The largest contributor to overall SLR in the Antarctic are outlet glaciers of the ASS (*Martín-Español et al.*, 2016). In this region, warm waters have eroded the ice shelf, resulting in a loss of buttressing. Due to the reduction in the restraining force, many major outlet glaciers in this section have sped up in recent decades (*Mouginot et al.*, 2014; *Rignot et al.*, 2014). While in the ASS, the loss of buttressing has been more or less gradual, caused by constant thinning and retreat of the ice shelf, a more dramatic loss of buttressing presented the collapse event of Larsen B Ice Shelf, AP, in 2002 (*De Rydt et al.*, 2015). This collapse event

demonstrated for the first time unambiguously the effect of a buttressing ice shelf, as grounded ice upstream sped up eightfold in response to the complete removal of the ice shelf (*Rignot et al.*, 2004; *Scambos et al.*, 2004; *Rott et al.*, 2007). Outlet glaciers are still adjusting to the new boundary conditions ∼15 years after ice-shelf collapse (*Scambos et al.*, 2014).

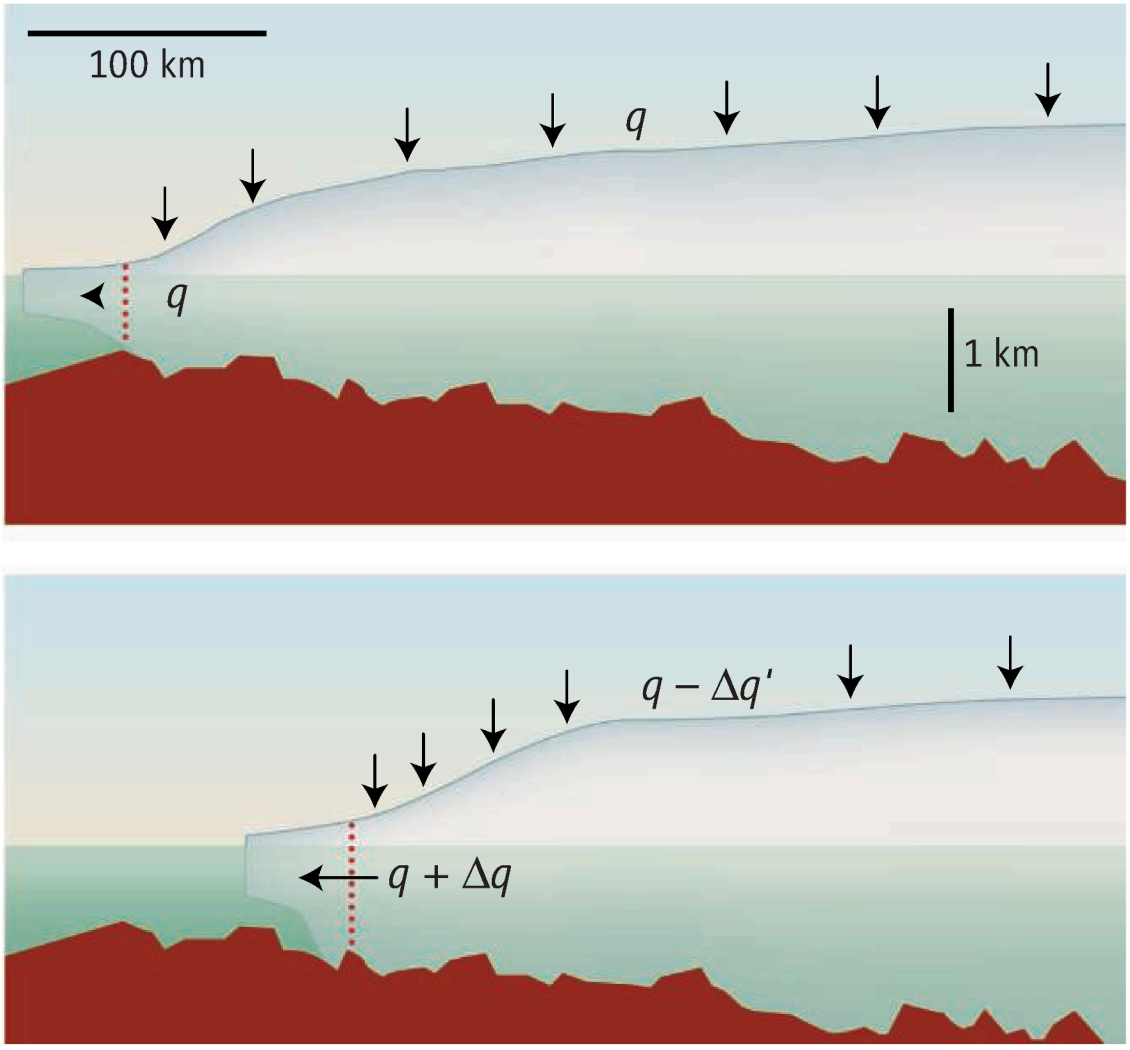

Figure 1.8: Sketch of a marine ice sheet based on the geometry of Thwaites Glacier, West Antarctica. In upper panel, ice sheet is in equilibrium. In lower panel a small perturbation led to the ice sheet being engaged in MISI (from *Vaughan and Arthern*, 2007).

The magnitude of the response of the grounded ice to ice-shelf removal may vary from region to region. In certain geometric settings, a loss of buttressing can lead to a runaway retreat of the grounded ice, often referred to as marine ice sheet instability (MISI) (*Weertman*, 1974; *Thomas and Bentley*, 1978; *Schoof*, 2007). A marine ice sheet is characterised by basal topography located below sea level that slopes down inland from the coast (Figure 1.8). The prime example for such a marine ice sheet is the WAIS.

Theory has shown that ice discharge across the grounding line increases nonlinearly (*Schoof*, 2007) with ice thickness ($q \propto h_{gl}^5$, where h_{gl} is ice thickness at grounding line). In steady state, grounding-line flux q must match the balance flux ax e.g. $q = ax$, where a is the spatially invariant accumulation rate and x is the upstream catchment length. Steady state is reached wherever this condition is met. Considering an undulating basal topography as in Figure 1.9b, steady state is reached at three locations, indicated by the blue and red lines in Figure 1.9a. Two of these steady states are stable (green vertical line) and one steady state is unstable (yellow vertical line). If the glacier front rests on a forward bedrock slope (Figure 1.9b, green lines), a small perturbation causing a retreat (e.g. by decreasing a), reduces the thickness at the grounding line. This leads to $q < ax$ due to the fact that $q \propto h_{gl}^5$. As a consequence of that, the grounding line advances back to its initial position. In a similar way, if the perturbation induces advance (e.g. increasing a), ice thickness at the grounding line increases and $q > ax$, resulting in a grounding-line retreat to its initial position. This situation is called a stable steady state. This stable situation changes when the ice sheet rests on a marine bedrock which slopes down inland (reverse sloping bed). In this case, a perturbation causing retreat leads to thicker ice at the grounding line, causing $q > ax$ and thus promoting even further retreat until a new steady state position is reached (Figure 1.9b, upper green geometry). Conversely, a perturbation inducing advance slows down ice discharge across the grounding line ($q < ax$), promoting further

advance. This positive feedback mechanism corresponds to an unstable steady state.

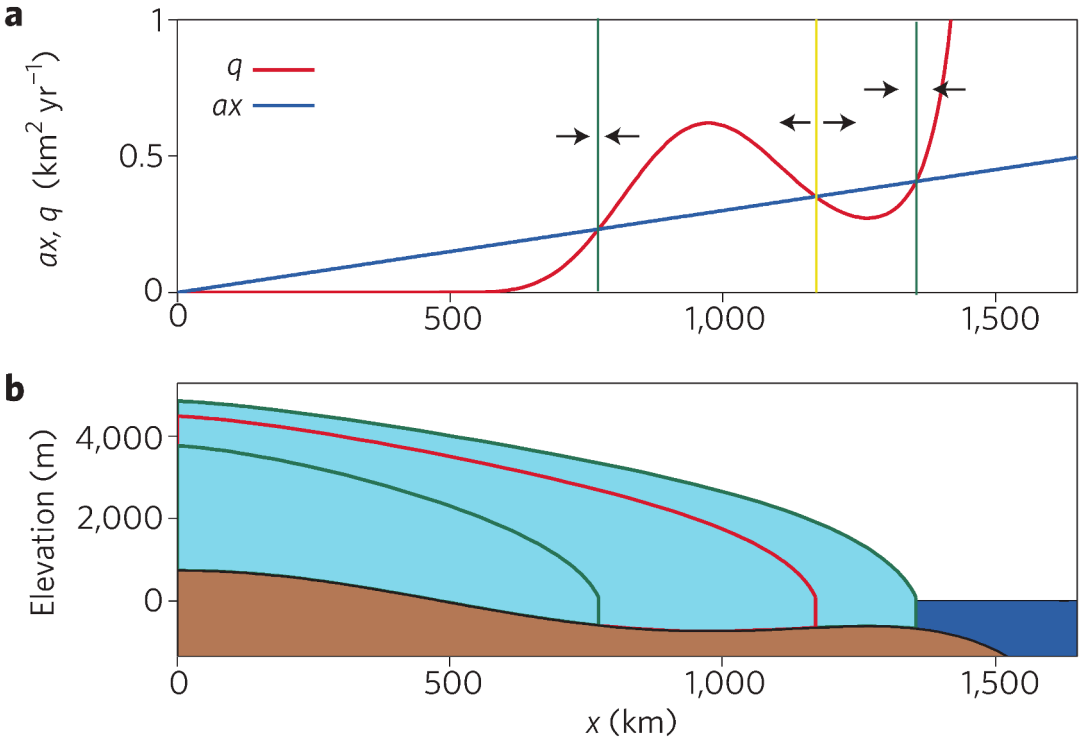

Figure 1.9: (a) Grounding-line flux q (red) and balance flux ax (blue) as a function of horizontal distance x. Vertical lines are steady state grounding lines (green for stable and yellow for unstable) and arrows indicate likely directions of the grounding line between the steady states. (b) Corresponding steady state ice sheet profiles (green for stable and red for unstable)[from *Joughin and Alley* (2011), adapted from *Schoof* (2007)].

Schoof's (2007) analysis is based on a flow field that varies primarily in the along-flow direction. This means the problem can be reduced to a problem in one horizontal dimension (1HD). It applies to a marine ice sheet with an unconfined ice shelf (no buttressing), but marine ice sheets can be stable as long as ice shelves provide sufficient buttressing to stabilise the system (*Gudmundsson*, 2013). *Gudmundsson et al.* (2012) showed that the 1HD concept cannot be readily

expanded to two horizontal dimensions as complex 2D buttressing starts to act e.g. through lateral stresses. They found that marine ice sheets on reverse sloping beds are not unconditionally unstable, but may in fact have stable steady state positions on such a bedrock configuration due to these 2D buttressing effects.

One region to have been affected by MISI is the ASS. The ASS is part of the WAIS, the region of the AIS contributing the most to overall SLR (*Rignot et al.*, 2008; *Shepherd et al.*, 2012; *Martín-Español et al.*, 2016). The main source for this high overall contribution is the dynamic thinning experienced in the ASS (*Martín-Español et al.*, 2016). Since 1973, ice discharge from the ASS has increased by 77% (*Mouginot et al.*, 2014). Because of that, the ASS has received a lot of attention in recent years (e.g. *Joughin et al.*, 2010; *Mouginot et al.*, 2014; *Rignot et al.*, 2014; *Nias et al.*, 2016; *Joughin et al.*, 2016) in an attempt to determine whether MISI has already been initiated or not. Assuming that current bedrock topography maps are accurate, recent ice-sheet modelling efforts suggest that the ASS may indeed already be engaged in MISI (*Favier et al.*, 2014; *Joughin et al.*, 2014). The region will most likely continue to retreat for at least the next 20 years, and thus continue to be a crucial contributor to global SLR beyond this (*Favier et al.*, 2014; *Joughin et al.*, 2014; *Cornford et al.*, 2015; *Ritz et al.*, 2015; *DeConto and Pollard*, 2016). While *Cornford et al.* (2015) project SLR from the ASS to be between 1.5-5 cm and 5.0-15 cm by 2100 and 2200, respectively, *Ritz et al.* (2015) project SLR of 25 cm and 48 cm by 2100 and 2200, respectively. The discrepancy between the projected SLR contributions originate primarily from the model set-up rather than the applied forcing which is similar in both studies. In the ice-sheet model of *Ritz et al.* (2015) grounding-line retreat is not explicitly simulated, but is parameterised through a combination of a statistical model and theoretical ice dynamical considerations. In comparison, *Cornford et al.* (2015) simulate grounding-line retreat explicitly. However, the simpler model set-up employed by *Ritz et al.* (2015) permits using a calibrated ensemble approach for the projections.

This allows to assign a probability to each of the presented SLR projections. Due to the computationally more expensive model set-up employed by *Cornford et al.* (2015), the authors are limited to a few simulation for each emission scenario. This highlights the fact that projections can vary considerably depending on the selection of the ice-sheet model.

The AP is another region of the AIS where SLR contributions in the recent past are primarily due to ice dynamics (*Martín-Español et al.*, 2016). Owing to a number of ice-shelf collapse events in recent decades (Larsen Inlet Ice Shelf (1989), Prince Gustav Ice Shelf (1995), Larsen A Ice Shelf (1995), Larsen B Ice Shelf (2002) (*Rott et al.*, 1996; *Scambos et al.*, 2000, 2004)) alongside ice-shelf thinning and retreat, the AP's ice dynamic contribution to SLR has increased substantially since the early 2000s. Mass loss was highest in the northern AP between 2003-2005, immediately following the major collapse event of Larsen B Ice Shelf. Since then, mass loss has been relatively constant (*Rott et al.*, 2014; *Martín-Español et al.*, 2016). This trend of ice dynamic loss in the northern AP has been more than offset by an increasing contribution from the southern AP (*Wouters et al.*, 2015; *Martín-Español et al.*, 2016), where mass loss rates increased from -16±5 Gt a^{-1} between 2007-2009 to -39±6 Gt a^{-1} during 2010-2013 (*Wouters et al.*, 2015; *Martín-Español et al.*, 2016). Despite the identification of the importance of ice dynamic SLR contribution from the AP, realistic SLR projections are still lacking (*Barrand et al.*, 2013b). In the light of the projected increase in atmospheric and oceanic temperatures, the importance of ice dynamic SLR contributions may even increase as more ice shelves are expected to collapse.

1.3 Ice-sheet modelling

In order to be able to make projections of future SLR in response to ice-shelf collapse, numerical ice-sheet models are required. Force balance approximation

for the grounded ice (*Hutter*, 1983) and floating ice (*Morland and Zainuddin*, 1987; *MacAyeal*, 1989) have been around for quite some time, but numerical models that are capable of modelling the coupled ice sheet-ice shelf system are still limited in number, even though more of these models have emerged in recent years (*Winkelmann et al.*, 2011; *Larour et al.*, 2012; *Pollard and DeConto*, 2012a; *Cornford et al.*, 2013; *Pattyn*, 2017). If the full system momentum balance (henceforth full-Stokes (FS) models) was solved in these numerical models, there would not be any problems with mechanical coupling the ice shelf with the ice sheet, as the general equation of motion (equation 1.6) applies to both the ice sheet and the ice shelf equally. However, due to computational limitations continental scale simulations using FS models are still unfeasible and ice-sheet models rely on an approximate force balance for prognostic simulations. Such simplifications are permissible provided that the essential physics are retained (*Van der Veen and Payne*, 2004). Even though grounded and floating ice have the same fundamental rheology, large scale-flow regime and scaled equations of motion (approximation to the force balance) differ (e.g. *Pollard and DeConto*, 2009). Flow in grounded ice is dominated by vertical shear ($\frac{du}{dz}$) due to basal resistance provided by the underlying bedrock (Figure 1.10), whereas ice flow of floating ice is dominated by horizontal stretching ($\frac{du}{dx}$) determined non-locally by the floating ice thickness distribution (e.g. *Pollard and DeConto*, 2009, 2012a). Ice flow in the transition zone close to the grounding line (Figure 1.4) changes from sheet flow to shelf flow and is characterised by a combination of the flow regimes (Figure 1.10). One of the main challenges in ice-sheet modelling is how to combine these different flow regimes together in coupled ice sheet-ice shelf models (*Vieli and Payne*, 2005; *Pollard and DeConto*, 2009; *Pattyn et al.*, 2013; *Bernales et al.*, 2017).

In this chapter, a brief overview of different approximations implemented in numerical ice-sheet models is presented. Focus is given to different approximations to the force balance implemented in the ice-sheet models used in this thesis. For

completion, equations for conservation of mass and conservation of energy are also provided. In all presented ice-sheet model simulations in this thesis the temperature is assumed to be constant and the ice temperature evolution equation is not solved unless stated otherwise.

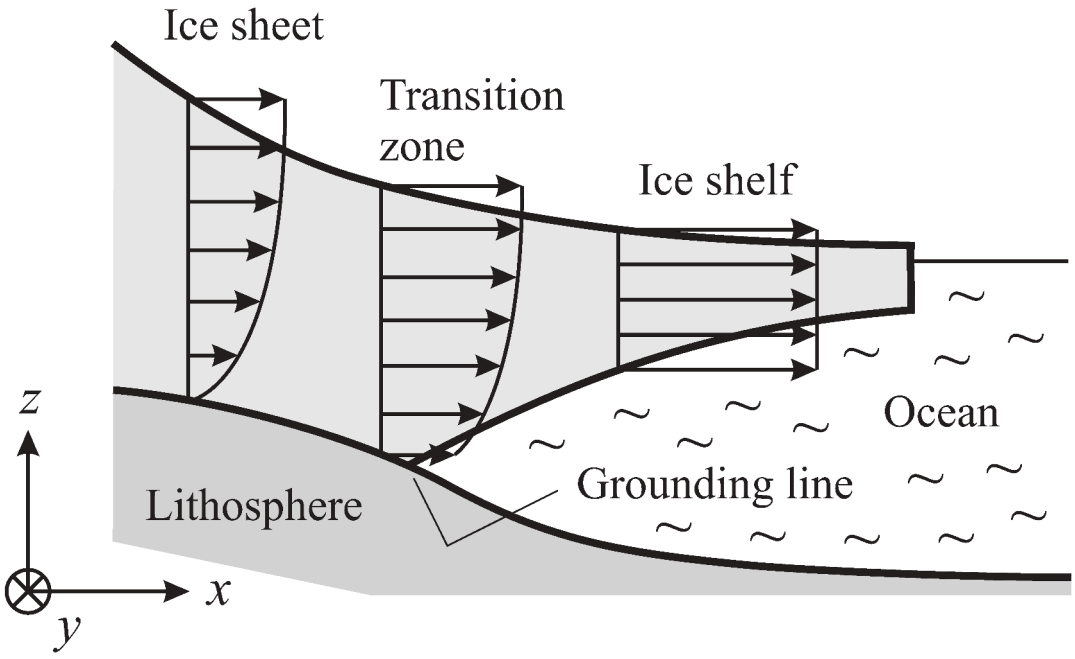

Figure 1.10: Flow regimes in an ice sheet-ice shelf system. In the grounded ice sheet vertical shear dominates, whereas in the floating ice shelf plug flow dominates. In the vicinity of the grounding line a transitional pattern is present (from *Greve and Blatter*, 2009).

1.3.1 Conservation laws

In ice-sheet modelling three conservation laws are typically used (*Slingerland and Kump*, 2011; *Van der Veen*, 2013):

- **conservation of mass:** the time rate of mass change in a control volume equals the mass rate into the volume minus the mass rate out
- **conservation of momentum:** the time rate of momentum change in

a control volume equals the momentum rate into the volume minus the momentum rate out

- **conservation of internal energy:** the energy retains a constant value in all the changes of the motion form.

The corresponding balance equations of mass, momentum, and internal energy read (*Greve and Blatter*, 2009)

$$\frac{\mathrm{d}\rho_i}{\mathrm{d}t} = -\rho_i \nabla \cdot \vec{v}, \tag{1.5}$$

$$\rho_i \frac{\mathrm{d}v}{\mathrm{d}t} = \nabla \cdot \sigma + \underbrace{\rho_i g}_{\text{gravity}} - \underbrace{2\rho_i \Omega \times \vec{v}}_{\text{Coriolis}}, \tag{1.6}$$

$$\rho_i \frac{\mathrm{d}e_{si}}{\mathrm{d}t} = -\nabla \cdot f_h + \underbrace{tr(\sigma \cdot D)}_{\text{dissipation power}} + \rho_i r. \tag{1.7}$$

Here $\frac{\mathrm{d}}{\mathrm{d}t}$ is the material derivative, ρ_i is the ice density, $\vec{v}$ is the 3D ice velocity vector, σ is the Cauchy stress tensor, g is the gravitational acceleration, Ω is the Earth angular velocity, e_{si} is the specific internal energy, f_h is the heat flux vector, D is the strain-rate tensor, and r is the specific radiation power.

When modelling ice flow several approximations can be made to simplify equations 1.5-1.7. Firstly, ice is assumed to be an incompressible material, so that ice density is constant ($\rho_i = const$ and $\frac{\mathrm{d}\rho_i}{\mathrm{d}t} = 0$). Moreover, ice is a very viscous fluid and a simple scaling shows that acceleration ($\rho_i \frac{\mathrm{d}v}{\mathrm{d}t}$) and Coriolis force ($2\rho_i \Omega \times v$) can be neglected for ice flow. Finally, constitutive equations can be inserted for internal energy e_{si}, heat flux f_h and dissipation power $tr(\sigma \cdot D)$. Thus, equations (1.5), (1.6), and (1.7) become (*Greve and Blatter*, 2009)

$$\nabla \cdot \vec{v} = 0, \tag{1.8}$$

$$\nabla \cdot \sigma + \rho_i g = 0, \tag{1.9}$$

$$\rho_i c_p \frac{\mathrm{d}T}{\mathrm{d}t} = \nabla \cdot (\kappa_i \nabla T) + \Phi, \tag{1.10}$$

where c_p is the heat capacity of ice, κ_i is the thermal conductivity of ice, T is the ice temperature, and Φ is the internal frictional heating due to deformation.
Since the temperature equation is ignored in the ice-sheet models presented here and the equation of linear momentum (equation 1.9) only provides a diagnostic equation (time independent), the continuity equation (equation 1.8) is required for any prognostic simulations (*Van der Veen and Payne*, 2004). In component form, equation 1.8 can be written as

$$\frac{\partial u}{\partial x} + \frac{\partial v}{\partial y} + \frac{\partial w}{\partial z} = 0, \tag{1.11}$$

here x,y,z represent a 3D Cartesian coordinate system, with x being the along ice flow axis, y the across flow axis, and z the vertical axis. The corresponding velocity components are u, v, and w, respectively. To introduce time dependence, the vertically integrated form of equation 1.11 is combined with mass balance terms at the upper and lower boundary (also referred to as kinematic boundary condition) to give the transport equation (*Greve and Blatter*, 2009; *Pattyn et al.*, 2013)

$$\frac{\partial h}{\partial t} = -\frac{\partial(\bar{u}h)}{\partial x} - \frac{\partial(\bar{v}h)}{\partial y} + SMB - BMB - OMB - CMB - FMB, \tag{1.12}$$

where $\bar{u}$ and $\bar{v}$ are column averaged horizontal velocities, SMB is surface mass balance, BMB is basal melting (if grounded), OMB is oceanic sub-ice melting or freezing (if floating), CMB is calving loss (floating edge), and FMB is face melt loss (floating or tidewater vertical face). It is noteworthy that this is just one variant of the ice thickness equation (*Pollard and DeConto*, 2012a) and other slightly different notations exist (e.g. *Van der Veen*, 2013).

1.3.2 Force balance approximations

To facilitate comparison between the different force balance approximations, the equation of linear momentum (equation 1.9) is written in component form, assuming gravitation only acts in the vertical direction (z-direction).

$$\frac{\partial \sigma_{xx}}{\partial x} + \frac{\partial \sigma_{xy}}{\partial y} + \frac{\partial \sigma_{xz}}{\partial z} = 0, \tag{1.13}$$

$$\frac{\partial \sigma_{yx}}{\partial x} + \frac{\partial \sigma_{yy}}{\partial y} + \frac{\partial \sigma_{yz}}{\partial z} = 0, \tag{1.14}$$

$$\frac{\partial \sigma_{zx}}{\partial x} + \frac{\partial \sigma_{zy}}{\partial y} + \frac{\partial \sigma_{zz}}{\partial z} = \rho_i g. \tag{1.15}$$

This set of equations presents the equations for Stokes flow. FS models (e.g. Elmer/Ice (*Gagliardini et al.*, 2013)) solve this system of equations.
Higher order models (HOM) such as BISICLES (*Cornford et al.*, 2013) use the so called hydrostatic approximation in the vertical direction. This means resistive stresses in the vertical are neglected, simplifying equations 1.13-1.15 as follows (*Blatter*, 1995; *Pattyn*, 2003)

$$\frac{\partial \sigma_{xx}}{\partial x} + \frac{\partial \sigma_{xy}}{\partial y} + \frac{\partial \sigma_{xz}}{\partial z} = 0, \tag{1.16}$$

$$\frac{\partial \sigma_{yx}}{\partial x} + \frac{\partial \sigma_{yy}}{\partial y} + \frac{\partial \sigma_{yz}}{\partial z} = 0, \tag{1.17}$$

$$\frac{\partial \sigma_{zz}}{\partial z} = \rho_i g. \tag{1.18}$$

A simpler approximation describing the flow of floating ice is the shallow-shelf approximation (SSA). This approximation makes the additional assumption that vertical shear terms can be neglected (Figure 1.11), reducing equations 1.16-1.18 even further to

$$\frac{\partial \sigma_{xx}}{\partial x} + \frac{\partial \sigma_{xy}}{\partial y} = 0, \tag{1.19}$$

$$\frac{\partial \sigma_{yx}}{\partial x} + \frac{\partial \sigma_{yy}}{\partial y} = 0, \tag{1.20}$$

$$\frac{\partial \sigma_{zz}}{\partial z} = \rho_i g. \tag{1.21}$$

The simplest and most commonly used approximation for grounded ice is the shallow-ice approximation (SIA). In addition to the hydrostatic approximation, longitudinal stresses are ignored. Furthermore, normal stresses are equal to the negative pressure (*Greve and Blatter*, 2009). Applying all these assumptions to equations 1.13-1.15 and substituting an expression for hydrostatic pressure leads to the following equations

$$\frac{\partial \tau_{xz}}{\partial z} = \rho_i g \frac{\partial s}{\partial x}, \tag{1.22}$$

$$\frac{\partial \tau_{yz}}{\partial z} = \rho_i g \frac{\partial s}{\partial y}, \tag{1.23}$$

where τ_{xz} and τ_{yz} are the deviatoric vertical shear stresses and s is the surface elevation. This set of equations is valid for an ice sheet with a small aspect ratio (e.g. thickness scale much smaller than length scale). The main computational advantage of the SIA is that all stress and velocity components are determined locally. The main disadvantage of the SIA is that it is not valid in some key areas for ice-sheet modelling such as ice divides and grounding lines (*Hutter*, 1983; *Baral et al.*, 2001).

To model the coupled sheet-shelf system, HOM models or hybrid models are necessary. Hybrid models couple SIA and SSA through a heuristic rule and hence are capable of simulating the coupled sheet-shelf system (Figure 1.11). The Penn State University 3D (PSU3D) ice-sheet model is based on such coupling. Previous studies have shown that in order to resolve grounding-line motion accurately, a relatively fine mesh resolution is required in the transition zone (*Durand et al.*, 2009; *Gladstone et al.*, 2010; *Pattyn et al.*, 2012; *Cornford et al.*, 2015). To circumvent this fine mesh resolution requirement and loss of computational time, PSU3D incorporates an internal flux boundary condition at the grounding line using

Schoof's (2007) semi analytical solution (henceforth Schoof's flux formula) for ice flux across the grounding line given by

$$q_{bgl} = \left[\frac{\bar{A} \left(\rho_i g\right)^{n+1} \left(1 - \frac{\rho_i}{\rho_w}\right)^n}{4^n C} \right]^{\frac{1}{m+1}} \Theta^{\frac{n}{m+1}} \; h_{gl}{}^{\frac{m+n+3}{m+1}} \tag{1.24}$$

where Θ is the normalised buttressing factor, h_{gl} is ice thickness at the grounding line, $\bar{A}$ is the depth averaged rheological coefficient in Glen's flow law, ρ_w is the ocean water density, n is 3, m is 1/3, and C is the basal drag coefficient. Implementation of this internal boundary condition is based on a heuristic rule (e.g. *Pollard and DeConto*, 2009, 2012a). In this work three ice-sheet models are used: British Antarctic Survey Antarctic Peninsula Ice Sheet Model (BAS-APISM) - an SIA ice-sheet model (*Barrand et al.*, 2013b), PSU3D - a hybrid ice-sheet model (*Pollard and DeConto*, 2012a), and BISICLES - a HOM in terms of the stress balance (*Cornford et al.*, 2013).

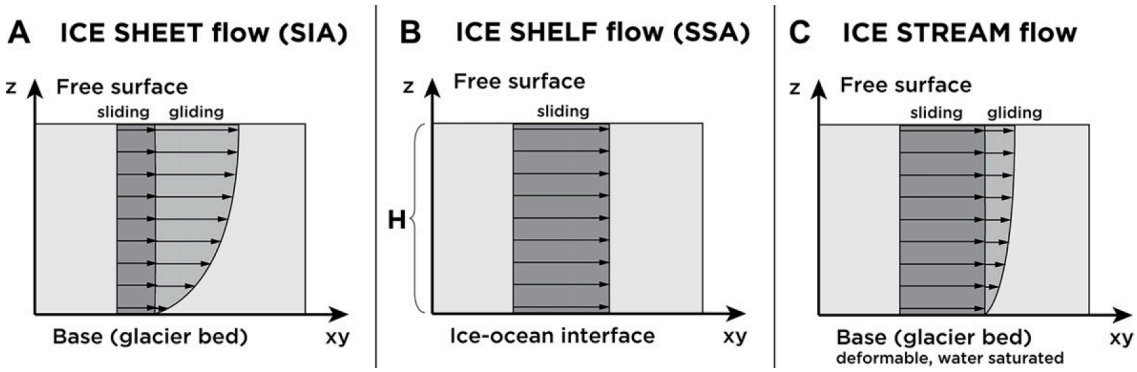

Figure 1.11: Sketch of grounded ice flow regime (SIA), ice-shelf flow regime (SSA), and flow regime as modelled in hybrid models (SIA+SSA) or ice streams - grounded glaciers with very little basal drag (from *Kirchner et al.*, 2011).

Chapter 2

Ice-dynamic sea-level rise projections from ice-shelf tributary glaciers[†]

2.1 Introduction

Over the last century, the AP region has warmed by 3.7±1.6°C (*Vaughan et al.*, 2003). This warming has been accompanied by a variety of responses, such as receding glacier fronts (*Cook et al.*, 2005), rising ocean temperatures (*Meredith and King*, 2005), prolonged melt season duration (*Vaughan*, 2006; *Barrand et al.*, 2013a; *Luckman et al.*, 2014), increased snowfall (*Turner et al.*, 2013), and retreat and disintegration of major fringing ice shelves (e.g. *Rott et al.*, 1996; *Scambos et al.*, 2000; *Cook and Vaughan*, 2010). This removal of ice shelves has led to speed-up (e.g. *De Angelis and Skvarca*, 2003; *Rott et al.*, 2011) and subsequent dynamic thinning of outlet glaciers (e.g. *Rignot et al.*, 2004; *Pritchard et al.*, 2009), contributing

[†]An edited version of this chapter was published by AGU. Copyright (2015) American Geophysical Union.

to SLR. Up until 2009, SLR contributions from APIS ($\sim$0.07 mm a^{-1}) and its surrounding islands were similar in magnitude to regional land-ice contributions from Alaska and the Canadian Arctic (*Hock et al.*, 2009; *Jacob et al.*, 2012; *Sasgen et al.*, 2013; *McMillan et al.*, 2014). However, recent studies suggest that mass loss in the southern APIS has accelerated dramatically since 2010, contributing $\sim$0.15 mm a^{-1} to overall SLR (*Wouters et al.*, 2015). This recent dramatic increase in mass loss has been attributed to ice dynamical processes. Efforts to project SLR from this region have been mostly restricted to glaciers and ice caps of Antarctic and sub-Antarctic islands and were exclusively based on modelling the SMB without consideration of glacier flow and iceberg calving (e.g. *Radic and Hock*, 2011; *Radic et al.*, 2014). Using temperature and precipitation scenarios from an ensemble of GCMs, these projections suggest that the surface mass loss of glaciers and ice caps on Antarctic and sub-Antarctic islands will continue over the next 100 years and could contribute between 5-40 mm sea-level equivalent (SLE; henceforth all SLR projections are given in mm SLE) by the end of the 21st century (*Radic and Hock*, 2011; *Radic et al.*, 2014). However, these projections do not include ice dynamic contributions to SLR following future ice-shelf collapse and therefore will most likely underestimate the actual SLR contribution from the AP.

Given the short response times of outlet glaciers in the AP (*Barrand et al.*, 2013b), ice dynamic SLR contributions resulting from continuing and future ice-shelf retreats will exceed those from surface mass loss on decadal time scales (e.g. *Rignot et al.*, 2005). *Scambos et al.* (2014) estimated the SLR contribution from glacier speed-up, inland thinning, and retreat of the grounding line (point where glacier ice becomes afloat) following the collapse of Larsen B Ice Shelf at 0.03 mm a^{-1}. It is expected that this contribution will diminish over time until outlet glaciers have adjusted to the new boundary conditions (*Schoof*, 2007). The timescale for adjustment back to steady state conditions following ice-shelf collapse is unknown, but presently outlet glaciers formerly feeding into Larsen A Ice Shelf are still

thinning, ∼20 years after ice shelf collapse, albeit at a decreasing rate (*Rott et al.*, 2014).

Modelling ice dynamic SLR following ice-shelf breakup requires knowledge of: i) the initial position of the grounding line; ii) the timing of ice-shelf collapse; and, iii) migration of the grounding line following ice-shelf breakup.

Locating the position of the grounding line is not straightforward as the grounding line may be a gradual transition from grounded to floating ice conditions (*Corr et al.*, 2001; *Brunt et al.*, 2010). The length of this transitional zone is typically in the order of a few km across the grounding line (*Brunt et al.*, 2010). Owing to the scale and inaccessibility of the grounding zone, remote sensing techniques are commonly used to map the position of the grounding line. In general, two differing types of remote sensing techniques are used to estimate the grounding-line position: dynamic mapping using differential satellite radar interferometry (DInSAR) (e.g. *Brunt et al.*, 2010; *Rignot et al.*, 2011a) or 'static' mapping using visible and near-infrared band (VNIR) satellite imagery (e.g. *Scambos et al.*, 2007; *Fricker et al.*). However, each method maps a different point in the transitional zone. Dynamic mapping approximates the landward limit of the ice flexure zone as the position of the grounding line, whereas static mapping approximates the break in surface slope as the position of the grounding line (*Brunt et al.*, 2010). In the absence of *in situ* grounding-line positions (*Horgan and Anandakrishnan*, 2006; *Pattyn et al.*, 2013), intercomparison of remote sensing techniques suggests that positions can deviate by ∼10 km in Antarctica, with higher deviations possible in lightly grounded areas (*Fricker et al.*; *Rignot et al.*, 2011a). The best agreement is reached in areas of slow moving ice, steep slopes and relatively simple surface topography (*Fricker et al.*; *Rignot et al.*, 2011a).

The position of the grounding line is expected to change in response to ice-shelf collapse (e.g. *Rott et al.*, 2002; *Rignot et al.*, 2004; *Schoof*, 2007). Therefore, knowledge of the timing of future ice-shelf collapse and understanding the processes

governing ice-shelf instability are vital. Most of the abrupt ice-shelf breakup events in the past have been linked to a warming climate (*Cook and Vaughan*, 2010). In addition, satellite observations have shown that Antarctic ice shelves have experienced increased melting at their base (e.g. *Shepherd et al.*, 2003, 2010; *Rignot et al.*, 2013). Under larger ice shelves, cold and dense high-salinity shelf water intrudes into the ice-shelf cavity. Due to the increased pressure with depth, the freezing temperature of seawater is lowered. This leaves the high-salinity shelf water with heat available to melt the base of the ice shelf, releasing cold and fresh meltwater at depth. As this meltwater rises, the increasing temperature results in the meltwater becoming supercooled and freezing onto the base of the ice shelf. In contrast, smaller ice shelves are directly influenced by CDW upwelling from the deep ocean (*Holland et al.*, 2008). CDW is a relatively warm (over 1°C) and dense deep water mass with the potential to cause high melt rates at the bottom of ice shelves (*Rignot and Jacobs*, 2002; *Holland et al.*, 2008). Typically, CDW intrudes into the ice-shelf cavity along bathymetric troughs, driving melt at the underside of the ice shelf. Many major outlet glaciers are located at the head of these eroded troughs and are therefore susceptible to CDW intrusions (*Pritchard et al.*, 2012). However, it is still poorly understood what controls these CDW intrusions.

In the AP region some fringing ice shelves might be vulnerable to CDW intrusions e.g. George VI Ice Shelf (e.g. *Jenkins and Jacobs*, 2008), but the scarcity of *in situ* oceanographic data makes testing this hypothesis difficult. The most recent retreat and collapse of Larsen B Ice Shelf has been attributed to increased surface ponding and enhanced surface crevasse fracture (*Scambos et al.*, 2000; *van den Broeke*, 2005). However, prior to final disintegration, Larsen B Ice Shelf had experienced a period of increased thinning, leaving the ice shelf vulnerable to hydrofracturing. *Shepherd et al.* (2003) suggested that this increased thinning was ocean-induced, warmer ocean water leading to higher basal melt rates. Other studies have suggested that at least part of the observed ice shelf thinning could be attributed to firn-air

compaction (e.g. *Holland et al.*, 2011; *Munneke et al.*, 2014). *Holland et al.* (2015) estimate that basal melting (and/or ice flux divergence) and firn-air compaction contribute about equally to the present-day surface lowering of Larsen C Ice Shelf. They argue that for this particular ice shelf at least two different forcings play a vital role in ice-shelf instability with other factors such as the stress field and marine ice most likely also influencing the ice shelf's stability (*Kulessa et al.*, 2014; *Jansen et al.*, 2015).

Due to the complexity of the governing processes leading to ice-shelf instability, data-led proxy approaches have previously been used to estimate the timing of ice-shelf collapse (e.g. *Vaughan and Doake*, 1996; *Fyke et al.*, 2010). Most commonly accepted is the approach that the geographical distribution of ice shelves in the AP region follows a climatic viability limit. The concept of a thermal limit of viability for ice shelves was first introduced by *Mercer* (1978) who observed that the geographical extent of ice shelves around the AP follows the 0°C isotherm of the warmest month of the year. As the density of available surface air temperature data improved, this thermal viability limit was slightly adjusted. *Vaughan and Doake* (1996) suggested the -5°C mean annual near-surface air temperature isotherm as the thermal viability limit. *Morris and Vaughan* (2003) then further refined the thermal viability limit based on observations that showed stable configurations for ice shelves south of the -9°C isotherm, no ice shelves present north of the -5°C isotherm, and ice shelves situated between these isotherms showing progressive retreat.

To provide more realistic SLR projections from ice dynamic adjustment following ice-shelf collapse, ice-sheet models need to account for the expected migration of the grounding line (e.g. *Pattyn et al.*, 2013). This problem can be tackled twofold; either by modelling the complete system of grounded and floating ice sheet and tracking the grounding line over time, or, by modelling the grounded ice only and parameterising the expected grounding-line migration. Modelling

ice sheet dynamics in full requires calculations of the 3-D equations of fluid flow (Stokes equations). To reduce complexity and permit more computationally efficient ice-sheet models, ice flow approximations are commonly used (e.g. *Hindmarsh*, 2004; *Pattyn et al.*, 2013). Ice flow in the grounded ice sheet is dominated by vertical shear and controlled by basal drag (except for ice streams), whereas in the floating ice sheet, ice flow is dominated by longitudinal stretching and experiences negligible amount of basal traction (e.g. *Schoof*, 2007; *Pollard and DeConto*, 2012a). Several ice flow approximations are available for the two different flow regimes, representing various levels of sophistication. If ice flow approximations are used in the ice-sheet model, both ice flow regimes require mechanical coupling to allow explicit grounding-line migration modelling (e.g. *Goldberg et al.*, 2009; *Pattyn et al.*, 2013). Even then the migration rate of the grounding line and its positional accuracy vary greatly across ice-sheet models. These discrepancies reflect differences in the sophistication of the mechanical ice-flow model, the numerical implementation of the ice-sheet model, and the grid resolution (e.g. *Vieli and Payne*, 2005; *Cornford et al.*, 2013). The level of complexity can be greatly reduced by only modelling the grounded ice sheet with the most commonly used SIA (*Hutter*, 1983). The challenge of having to mechanically couple two different ice flow regimes vanishes but since the SIA is not valid at ice divides and grounding lines, it automatically excludes explicit modelling of grounding-line migration. This necessitates the grounding-line migration to be parameterised (*Barrand et al.*, 2013a).

Modelling the mechanically coupled ice sheet-ice shelf system is more desirable as it is a more physically-based modelling approach. However, there are currently a very limited number of plane-view ice-sheet models that are capable of modelling grounding-line migration explicitly (e.g. *Winkelmann et al.*, 2011; *Pollard and DeConto*, 2012a; *Cornford et al.*, 2013). Of these models, even fewer have been used to run prognostic simulations under future climate scenarios (*Joughin et al.*, 2010). This is mainly due to the issues outlined above and increasing levels of

system uncertainty (*Vaughan and Arthern*, 2007). Additionally, the required fine grid resolution at the grounding line (≤100 m) (*Durand et al.*, 2009; *Cornford et al.*, 2013) and a lack of high resolution input data (e.g. BEDMAP2 has a grid resolution of 1 km; *Fretwell et al.*, 2013) render modelling of the coupled ice sheet-ice shelf system for APIS infeasible.

In the context of the rapid warming in the AP region, the ice dynamical response to ice-shelf collapse has started to be a significant contributor to eustatic SLR. Based on climate projections, this SLR contribution may become even more important over the next centuries. In this chapter, we compute the volume response of 210 ice-shelf tributary drainage basins (comprising ∼62% of the area of the AP) following ice-shelf collapse events. Ice-shelf collapse timing is estimated from GCM ensemble temperature projections for two different climate scenarios and grounding-line retreat is parameterised using a new statistical model. In the absence of process-based predictions of ice-shelf collapse timing, this series of scenario-based projections provides an estimate of the ice dynamical SLR from APIS over the next 300 years. The projected SLR modelled by our experiments should be understood as an upper (-9°C isotherm) and lower bound (-5°C isotherm) for each simulation.

2.2 Methods

2.2.1 Ice-sheet model description

While the rugged topography of the AP might suggest the use of a full-system ice-sheet model, the high computational cost and poorly known ice thickness distribution prevent such an application. Furthermore, in the absence of high-resolution input data, grounding-line migration modelling will be beset by

significant and compounding errors at every time step (*Schoof*, 2007). Instead, a modelling framework and strategy are devised to utilize the best currently available ice-sheet model of the AP (*Barrand et al.*, 2013b), its constituent boundary condition datasets, and a statistical parameterisation of grounding-line retreat. The volume evolution of the grounded portion of the AP is modelled following imposition of an empirical-statistical estimate of grounding-line retreat following ice-shelf collapse (see section 2.2.3). BAS-APISM is described in brief here, and the reader is referred to *Barrand et al.* (2013b) and references therein for a more detailed description of the model numerics.

BAS-APISM models ice flow by solving a linearised SIA equation, providing a scaling to the Stokes equations. This approach is appropriate to the grounded ice portion of APIS and permits low computational cost and a large ensemble of scenario calculations. The model is initialized using a combined altimetric and velocity initialization, taking advantage of the highest-quality observational boundary condition datasets (*Barrand et al.*, 2013b) and permitting a steady state starting condition. The use of a linearised diffusion-type ice sheet equation allows the flux perturbation equation to be solely ice flux-based. This negates the need to estimate the rate factor or specify whether or not basal sliding is occurring. As ice thickness appears just once as a divisor in one term of the perturbation equation (equation 16 in *Barrand et al.* (2013b)), the linearised approach is less sensitive to errors in ice thickness than traditional SIA-based models. This is important for the AP where detailed ice thickness measurements are not always available (*Fretwell et al.*, 2013). The linear nature of the flux perturbation equation also allows for superposable solutions, meaning that individual drainage basins can be modelled separately. SLR contributions from each modelled basin may then be summed to provide an ice-sheet-wide contribution. BAS-APISM omits horizontal stress gradients (membrane-like stresses (*Hindmarsh*, 2009)) which is expected to introduce errors in SLR projections over the early decades following imposed

grounding-line retreat (*Williams et al.*, 2012). It is estimated that these errors will decay several decades after the perturbation (*Barrand et al.*, 2013b).

2.2.2 Climate forcing

To estimate the timing of future ice-shelf collapse, ensemble near-surface air temperature projections from 14 GCMs that participated in the Coupled Model Intercomparison Project Phase 5 (CMIP5) (*Taylor et al.*, 2011) were used. Each GCM was forced using the emission scenarios 'business as usual' (RCP4.5) and 'high emission' (RCP8.5). Present-day temperature fields for the period 1979-2005 were represented by ERA-Interim climate reanalysis bi-linearly interpolated to a 0.5° x 0.5° grid. Following the bias correction approach of *Radic et al.* (2014) we shift the future monthly temperature time series for each GCM grid cell in the domain by the average bias for each month between the GCM and ERA-Interim temperatures over the period 1979-2005. In this way we corrected seasonality in the GCM temperature relative to seasonality in the reanalysis. The bias corrected GCM temperature fields were then bi-linearly interpolated to the ice sheet model grid (900 m). It is important to note that ERA-Interim reanalysis temperature fields are not bias free. *Jones and Lister* (2014) compared mean monthly ERA-Interim near-surface air temperature fields in Antarctica with mean monthly temperature records from 40 Antarctic weather stations and found that ERA-Interim displays a strong warm bias (up to 5°C) in the interior of the ice sheet and a cold bias in coastal areas (up to -6°C). For the AP, the picture is less homogeneous. At 6 of the 10 weather stations ERA-Interim shows a cold bias (up to -3.2°C) for the period 1979-2013 with an average cold bias for all 10 stations of -0.8°C. For more information on the selected GCMs and the method, the reader is referred to *Radic et al.* (2014).

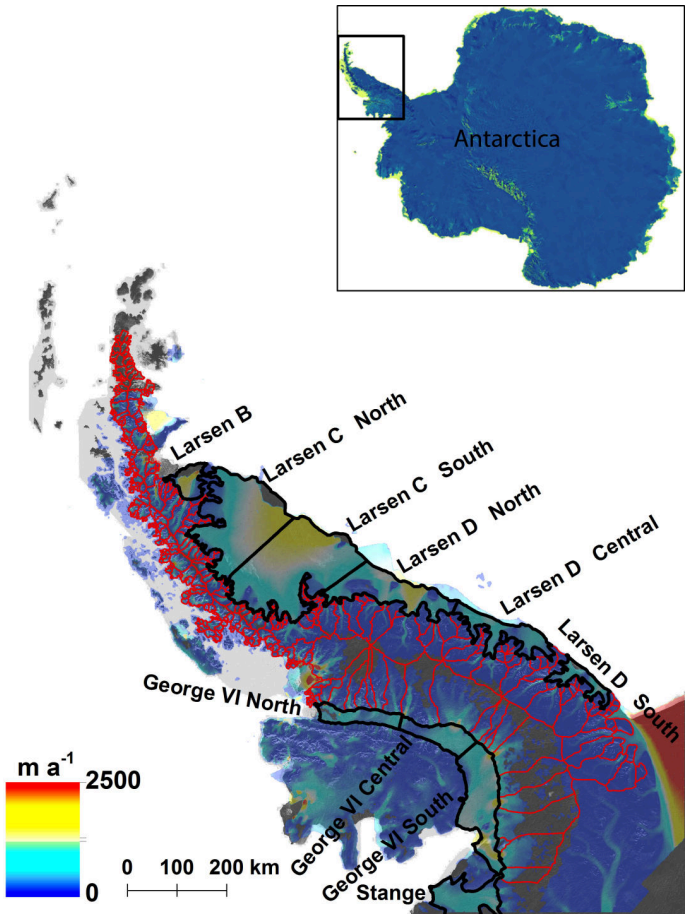

Figure 2.1: Landsat Image Mosaic of Antarctica (LIMA) of AP region (`http://lima.usgs.gov/index.php`) with surface ice velocity from *Rignot et al.* (2011a) overlain. Red outlines depict 460 largest drainage basins, and black lines show ice shelf subdivisions. Map approximates ice sheet model domain. Lower left corner in polar stereographic coordinates is at -2611350, 239850 and upper right corner at -1304550, 1669050.

In order to estimate ice-shelf collapse timing, the empirically-based ice-shelf viability limits - the -5°C and the -9°C mean annual isotherms - were tracked in the interpolated temperature fields. To allow for partial ice-shelf collapse, the major fringing ice shelves were divided into sub-entities, based on the N-S extent of each ice shelf. This results in one subdivision for Scar Inlet, two for Larsen C Ice Shelf, three for Larsen D Ice Shelf, three for George VI Ice Shelf, and one for Stange Ice Shelf (Figure 2.1).

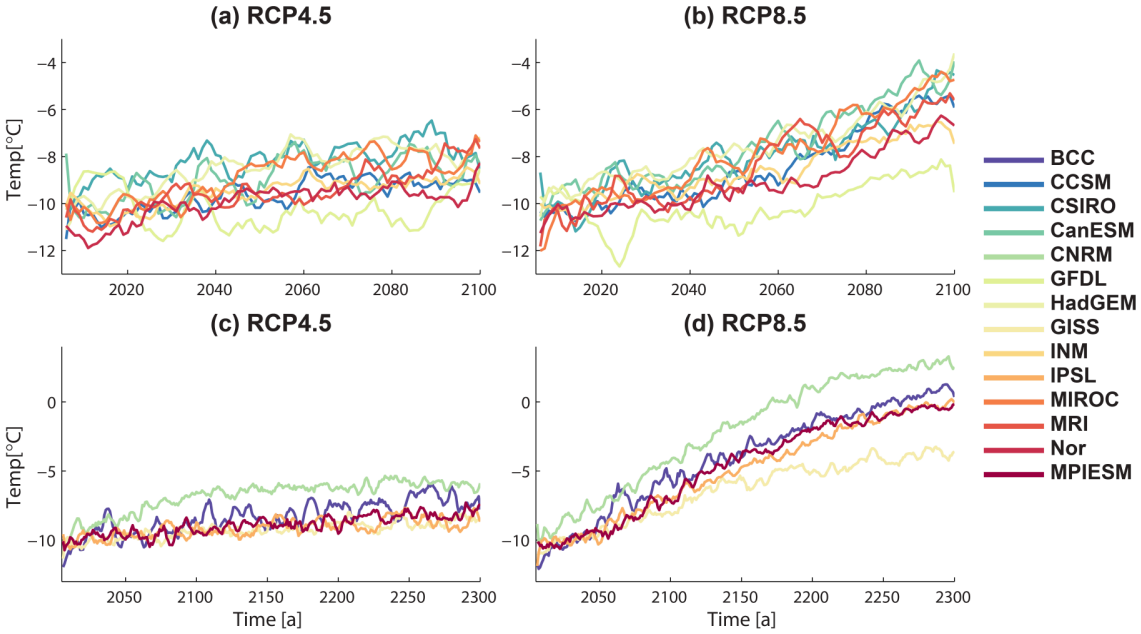

Figure 2.2: Smoothed (5-year running mean) mean annual near-surface air temperatures from 14 GCMs for ice-sheet model domain. Upper panel shows temperatures to 2100 for the (a) 'low emission' and (b) 'high emission' scenarios. Lower panel shows temperatures to 2300 for the (c) 'low emission' and (d) 'high emission' scenarios. A full list of GCMs can be found under: `http://cmip-pcmdi.llnl.gov/cmip5/citation.html`.

To our knowledge, no publication has investigated the lag time between passing of the thermal limit of viability and collapse of the ice shelf. Thus, three timing scenarios were used to estimate the timing of future ice-shelf collapse for the isotherms. Scenario 1 assumes immediate collapse of the ice-shelf sub-entity, if the entire ice-shelf sub-entity is located north of the respective limit of viability for one calendar year (no running mean scenario); Scenario 2 applies a 4-year running mean; and Scenario 3 applies an 8-year running mean. Scenarios 2 and 3 therefore require that the viability limit is south of the ice-shelf sub-entity for 4 and 8 consecutive calendar years respectively.

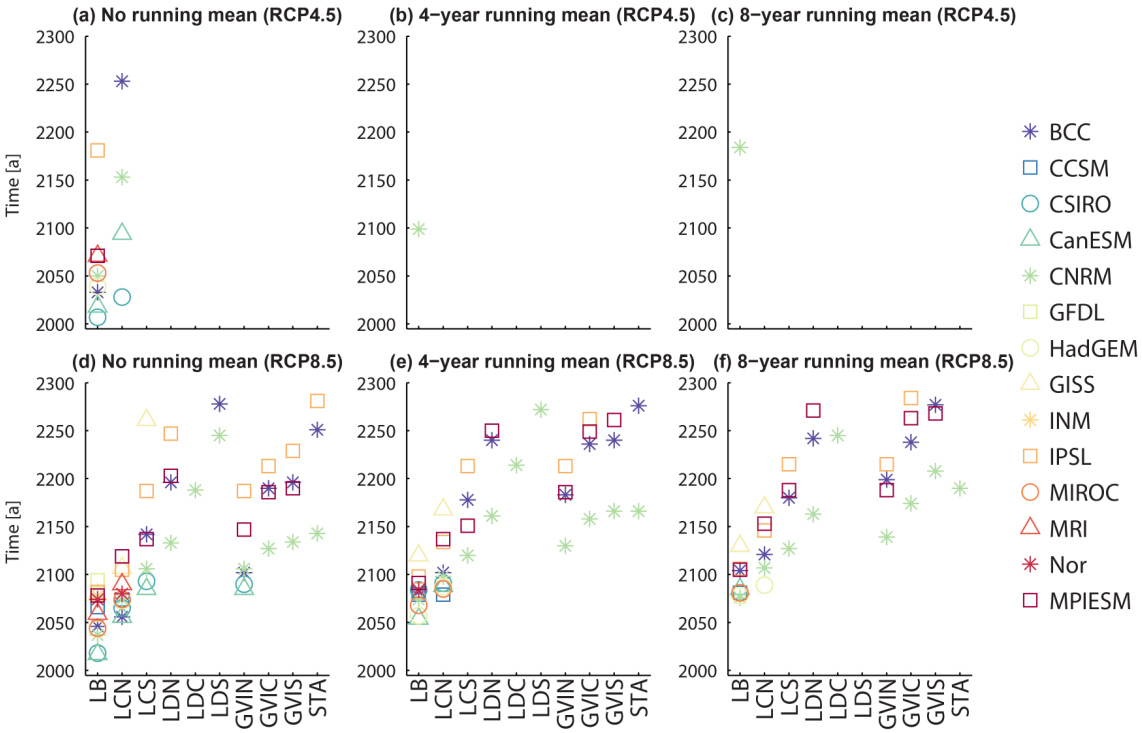

Figure 2.3: Ice-shelf collapse timing derived using the -5°C isotherm for all 10 ice-shelf entities. Ice-shelf abbreviations are as follows: LB = Larsen B Ice Shelf, LCN = Larsen C Ice Shelf North, LCS = Larsen C Ice Shelf South, LDN = Larsen D Ice Shelf North, LDC = Larsen D Ice Shelf Central, LDS = Larsen D Ice Shelf South, GVIN = George VI Ice Shelf North, GVIC = George VI Ice Shelf Central, GVIS = George VI Ice Shelf South, STA = Stange Ice Shelf

Mean annual temperature projections for the ice-sheet model domain are shown in Figure 2.2. The range in mean annual temperature across the GCMs is large, with temperature differences in excess of 4°C due to a number of cold/warm GCM runs (Figure 2.2b,d). In particular, GFDL displays a strong cold bias in the RCP8.5 scenario compared to the rest of the GCMs (Figure 2.2b). Nevertheless, the range modelled across both projection periods and emission scenarios are very similar (standard deviation ∼1.0°C), with the exception of Figure 2.2d where the range increases to 1.7°C. Air temperature projections show the expected steeper rise in the RCP8.5 scenario than in RCP4.5 (Figure 2.2b,d). For the GCMs spanning until

2300, the steepest temperature rise is observed in the 21st century before the rate of warming decreases during the latter two centuries (Figure 2.2d).

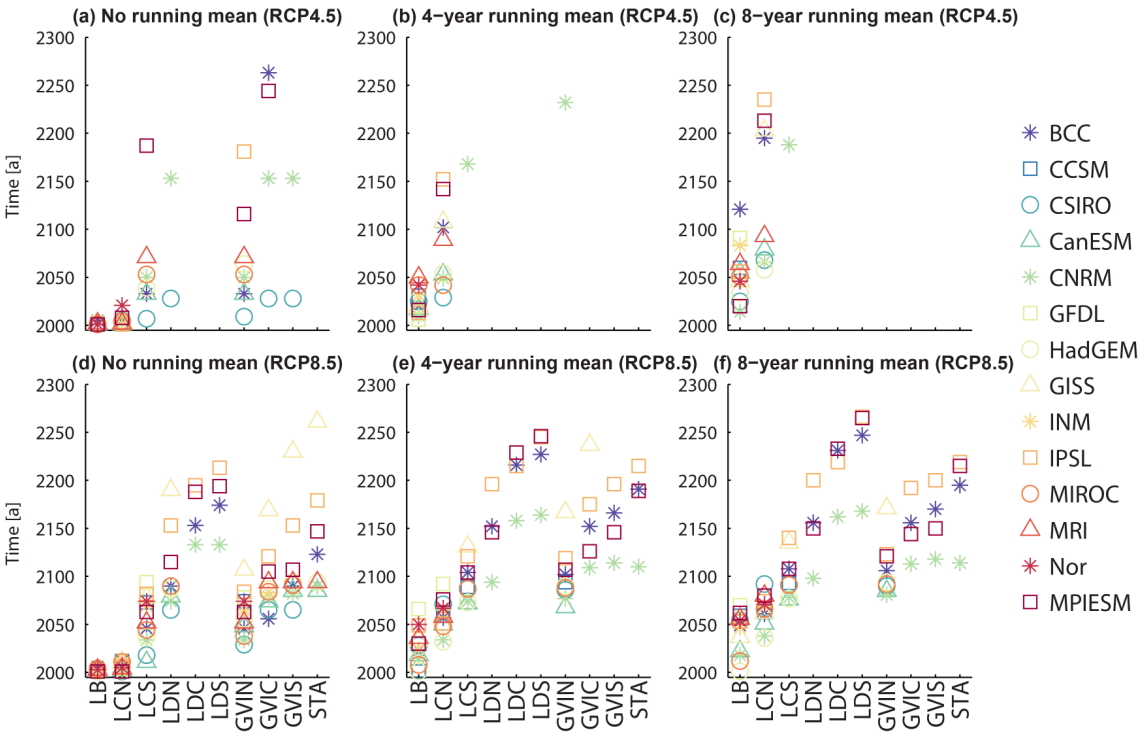

Figure 2.4: Ice-shelf collapse timing derived using the -9°C isotherm for all 10 ice-shelf entities. Ice-shelf abbreviations are the same as in Figure 2.3.

Differences in mean annual temperatures also propagate into ice-shelf collapse timing. There are significant differences in collapse timing within and across collapse timing scenarios. Predicted ice-shelf collapse can vary by more than 100 years for some ice shelves (e.g. Figure 2.3d, Stange Ice Shelf). Typically, GCMs estimate similar ice-shelf collapse timings up until 2050 from when they start to diverge, though this trend is not uniform across different scenarios. Judging from the ice-shelf collapse timings in Figure 2.4d-f, the majority of the GCMs appear to capture the east-west temperature gradient across the AP (collapses are predicted earlier for ice shelves on the west coast compared to those at similar latitudes in the east).

Using output fields from AOGCMs as forcing for standalone ice sheet simulations is common practice, but increases uncertainties in SLR projections (*Nowicki et al.*, 2016). A long standing problem in standalone ice-sheet simulations when forcing is provided by AOGCMs (e.g. CMIP5 AOGCMs) is that the AOGCMs treat the ice sheet as static (e.g. *Nowicki et al.*, 2016). This assumption is valid for decadal to century time scale simulations (*Edwards et al.*, 2014) if the ice sheet is near steady state. However, as AIS is losing mass at an increasing rate (e.g *Shepherd et al.*, 2012), this mismatch between ice-sheet model and model forcing reduces the confidence in SLR projections. At the surface, where either near-surface temperatures are used to derive the SMB, or the SMB is directly supplied, the SMB-Elevation (*Cuffey and Paterson*, 2010) feedback is not accounted for in the AOGCMs. This feedback means that as the ice sheet thins, the lower surface elevations lead to warmer temperatures and hence more surface melt. Such a change in ice sheet surface elevation can also affect the regional atmospheric circulation, either accelerating or slowing down ice mass loss (*Ridley et al.*, 2005). Over the course of the year, the surface albedo of an ice sheet can vary substantially (*Box et al.*, 2012), resulting in a positive radiation feedback that promotes further atmospheric warming and melting. In addition to the neglected processes at the top of the ice sheet, freshwater fluxes are not simulated in AOGCMs (*Nowicki et al.*, 2016). The freshening of the ocean water can lead to a modified density structure and may be strong enough to suppress convection. While the importance of this freshening effect is still under debate (*Hu et al.*, 2009; *Yang et al.*, 2016), *Yang et al.* (2016) suggest that freshwater influx from the Greenland ice sheet has already led to reduced deep convection in the Labrador Sea. Due to the importance of syncing model and forcing to improve confidence in SLR projections, the glaciology community has launched the Ice Sheet Model Intercomparison Project 6 (ISMIP6) in close collaboration with CMIP6 to investigate the ramifications of using coupled ice sheet AOGCMs instead of standalone ice-sheet model simulations forced with

AOGCMs with static ice sheets (*Nowicki et al.*, 2016).

2.2.3 Grounding-line retreat parameterisation

This section describes in detail the method used to estimate grounding-line retreat for all ice-shelf tributary drainage basins in response to ice-shelf collapse. In the first part, we develop a multivariate linear regression (MVLR) model and evaluate the model performance. In the second part, we use the results of our statistical model in conjunction with a simple speed-up scenario of tributary glaciers following ice-shelf collapse to estimate the final grounding line retreat for each individual drainage basin.

To map changes in grounding-line position, two grounding-line mapping products were used: 1) MOA (*Scambos et al.*, 2007) and 2) MEaSUREs (*Rignot et al.*, 2011a). For 189 of the mapped 193 drainage basins, there was a 8-10 year time differential between the data-sets, allowing detection of positional changes between 1994 and 2004. Positional changes were mapped at five locations along each drainage basin front at equal intervals and were then averaged. This was repeated for all 193 drainage basins. The mean positional change of these 193 drainage basins then served as the dependent variable for the statistical model. A range of independent variables was used to predict the value of the dependent variable. The selection of the predictor variables was based on observations from drainage basins of the AP presently adjusting to recent ice-shelf removal (*Rott et al.*, 2014; *Scambos et al.*, 2014; *Cook et al.*, 2014) and on theoretical ice dynamical considerations (*Schoof*, 2007; *Goldberg et al.*, 2009), affecting grounding line position. Table 2.1 comprises a list of all the variables. The variables are divided into a geometric class and an ice dynamical class. Drainage basins presently adjusting to ice-shelf removal have typically experienced larger grounding-line retreat than other basins. Therefore, a variable whether or not ice-shelf collapse occurred in between the grounding-line

mappings was included. In addition to this, a geographical variable ('Location') was included which divides the AP into four sub-regions (Figure 2.5a) and accounts for the reported spatially variable area loss of marine terminating glaciers in the AP region (*Cook et al.*, 2014; *Scambos et al.*, 2014).

Predictor variable	**Variable type**	**Class type**	**Rank**
Basin class	nonmetric	geometric	1
Ice-shelf collapse	nonmetric	ice dynamical	2
Basin ice velocity	metric	ice dynamical	3
Basin front	nonmetric	geometric	4
Location	nonmetric	-	5
Bedrock slope	metric	ice dynamical	6
Ice thickness at grounding line	metric	ice dynamical	7
Bedrock elevation at grounding line	metric	ice dynamical	8
Basin size	metric	geometric	9

Table 2.1: List of multivariate linear regression predictor variables for the AP grounding-line retreat parameterisation. Rank lists predictor variables in terms of their importance to overall model fit.

Following ice-shelf collapse, recent observations of the glaciers draining into the Prince-Gustav-Channel and the Larsen A embayment suggest the magnitude of the ice dynamic adjustment to be a function of glacier size, glacier geometry, mass turnover, and subglacial topography (*Rott et al.*, 2014; *Scambos et al.*, 2014). As shown by *Schoof* (2007), mass turnover of marine terminating outlet glaciers strongly depends on the ice thickness at the grounding line. The importance of

the subglacial topography has also been demonstrated in theoretical ice dynamical considerations (*Schoof*, 2007; *Goldberg et al.*, 2009), showing that for a 2D marine ice sheet, there cannot be a stable grounding-line position on reverse bed slopes, thus promoting sustained grounding-line retreat. The 'basin front' and 'basin class' variables were derived from *Cook et al.* (2014) for the AP from 63-70°S and extended to all drainage basins south of 70°S. A detailed overview of individual drainage basin classes is provided by *Cook et al.* (2014). The ice thickness at the grounding line, bedrock elevation at the grounding line, and bedrock slope were derived from *Huss and Farinotti* (2014) for the AP from 63-70°S and, for all drainage basins south of 70°S from BEDMAP2 (*Fretwell et al.*, 2013). Both data sets had previously been bi-linearly interpolated onto the ice-sheet model grid.

As outlined above, the position of the grounding line is affected by a range of variables. Multivariate linear regression allows to examine the relationship between this set of variables and a dependent variable (grounding-line position). The statistical model has the form

$$Y = \alpha_0 + \beta_i X_i + \epsilon \qquad\qquad i = 1, ...9 \tag{2.1}$$

where α_0 is the intercept, β_i is the regression coefficient, X_i is a predictor variable, and ϵ is the residual or prediction error (*Hair et al.*, 1995). Since some of the mapped changes in grounding-line position may be erroneously large or small due to mislocation of the grounding line position of the mapping products, the regression was performed in a robust mode to reduce the effect of outliers on the results. The robust mode assigns a weight based on the bi-square weighting function

$$w = (abs(r) < 1) \times (1 - r^2)^2, \tag{2.2}$$

where value r in the weight function is

$$r = resid/(tune \times s \times \sqrt{1-h}). \tag{2.3}$$

Here $tune = 4.685$, $resid$ is the vector of residuals from the previous iteration, h is the vector of leverage values from a least-squares fit, and s is an estimate of the standard deviation of the error term computed by

$$s = MAD/0.6745, \tag{2.4}$$

where MAD is the median absolute deviation of the residuals from their median. Analysis of the residuals of our model reveals that the underlying assumptions of linearity, heteroscedasticity (presence of unequal variances), and the independence of the error terms are all complied by our MVLR (*Hair et al.*, 1995). Residuals of the model are not strictly normally distributed but display 'thin tail' in their distribution pattern, violating the assumption of normality of the error term distribution. This means that for extreme values, the predicted values are significantly under- or overestimated. However, only a relatively small number of drainage basins (<20 basins) are affected by this (Figure 2.5c). The correlation is significant at the 1% level but with a relatively low R^2 value of 0.22. The corresponding standard error of the analysis is 219 m a^{-1}. We tested the relative importance of each individual predictor variable to the overall model fit by leaving out one by one predictor in the model and calculating how the correlation changes. This reveals that the most important predictor variables are 'basin class', 'ice-shelf collapse', and 'ice velocity' (Table 2.1). However, up to rank 7, all variables contribute almost equally to the overall model fit. In comparison, the predictor variables 'bedrock elevation at the grounding line' and 'basin size' do not contribute significantly to the overall model fit. We still include them into our statistical model since we attribute their relative unimportance to the very heterogeneous

glaciological setting in the AP but they may be important locally. The quality of the model is significantly improved by only using the higher resolution bedrock topography and ice thickness data from *Huss and Farinotti* (2014) for the northern AP (63° - 70°S). In that case, the R^2 rises to 0.49 and the corresponding standard error reduces to 184 m a^{-1}. However, as there are almost no ice-shelf tributary drainage basins in this part of the AP, the results of the model would be skewed towards the other basin classes. To avoid this bias in our analysis, we rather accept the poorer model with less bias towards non-ice-shelf tributary drainage basins.

Given the annual positional changes estimated from the model, the following scenario is assumed for each of the 210 ice-shelf tributary drainage basins: In response to ice-shelf removal, tributary outlet glaciers will show an immediate speed-up. In the years following the initial acceleration, the outlet glaciers will slowly adjust to the new boundary conditions and the velocity acceleration will decay over time until pre-ice-shelf collapse velocities are restored. Similar behavior has been reported from drainage basins flowing into the former Larsen A and Larsen B embayments (e.g. *Rott et al.*, 2002, 2011; *Wuite et al.*, 2015). The time period it takes for each drainage basin to adjust to the new boundary conditions is defined as the adjustment period. The initial speed-up applied to each drainage basin is normalized on the basis of observations from outlet glaciers feeding into the former Larsen B Ice Shelf. *Rignot et al.* (2004) reported an 8-fold outlet glacier velocity increase as maximum. Thus, we apply an 8-fold initial velocity increase to the fastest flowing outlet glacier (820 m a^{-1}) and no acceleration to all drainage basins with velocities <15 m a^{-1}. For all the drainage basins with velocities between these bounds, the initial velocity acceleration is determined by fitting an exponential function through the upper and lower bounds (Figure 2.5b). The length of the adjustment period was also normalized, applying a maximum of 15 years to the drainage basin with the fastest ice velocity and 1 year to drainage basins with velocities <15 ma^{-1}. For all drainage basins with velocities between these bounds,

the adjustment period follows a linear curve fitted through the upper and lower bounds. The length of the adjustment period is reasonable, considering that recent observations from drainage basins formerly feeding into Larsen A Ice Shelf are still adjusting some 20 years after ice shelf disintegration (*Rott et al.*, 2014).

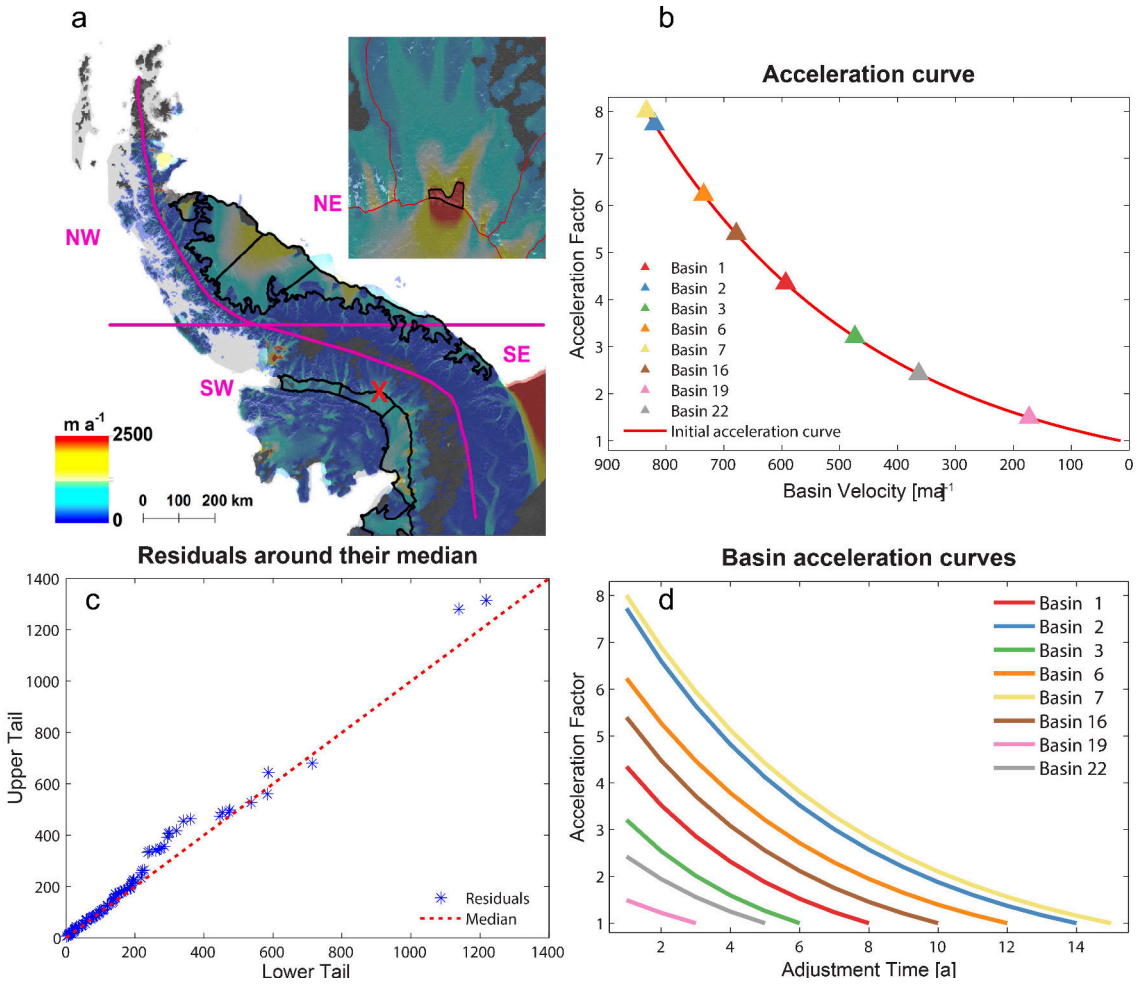

Figure 2.5: (a) Map as in Figure 2.1, including 'Location' variable (pink). Red cross approximates location of inset map. Inset map shows sample drainage basin of area (black) used for velocity acceleration in statistical model. (b) Displays initial acceleration curve with triangles approximating the starting position of basin acceleration curves in (d). (c) Shows the distribution of residuals of the MVLR.

Given initial acceleration and length of adjustment period, an exponential function is fitted through these two endpoints for each individual drainage basins. The exponential function was used to account for non-linearities in the system. Figure 2.5d shows acceleration curves for a number of sample drainage basins. Total grounding-line retreat rates are then calculated for each basin using the regression equation and multiplying the velocity coefficient by the calculated acceleration factor in each year. These annual retreat rates are then summed up to provide the final grounding-line retreat. This method results in an average grounding-line retreat of 1.4 km for all ice-shelf tributary drainage basins. The majority of the drainage basins show grounding-line retreat less than 1 km, with 5 drainage basins showing total grounding-line retreat >10 km and a maximum grounding-line retreat of 42 km (basin 7).

2.2.4 Experimental setup

As GCMs provide empirically-based ice-shelf breakup timing estimates for two different time periods (2000-2200 and 2000-2300), two sets of simulations were performed. Experiment 1 included the ice-shelf collapse timing of all 14 GCMs, allowing ice-shelf breakup to occur until 2100. Following ice-shelf breakup, each individual ice-shelf tributary drainage basin was simulated until 2200, providing at least a century to adjust to the new boundary conditions. Experiment 2 included the ice-shelf collapse timing of the 5 GCMs spanning to 2300 and allowing ice-shelf breakup until 2300. Each ice-shelf tributary basin's response to the imposed grounding-line retreat was then modelled until 2300, reducing the potential length of the adjustment period in comparison to Experiment 1. The grounding-line retreat was readily imposed by instantaneously forcing the thickness anomalies in the zones downstream of the prescribed new grounding line such that the original ice surface

plus anomaly are at sea level.

As an instantaneous grounding-line retreat is somewhat unrealistic, the same experiments were repeated enforcing a step-wise imposition of the estimated grounding-line retreat. Using the annual retreat rates derived from the statistical model, grounding-line retreat steps of 0.5, 1, 2, 3, 4, 5, 7.5, 10, 15, and 20 km were applied before the final maximum grounding-line retreat was imposed. In addition to modelled changes to 2300, each drainage basin was simulated until it reached steady state. Here, steady state is reached if the annual volume loss is <1% of the initial volume loss of the first year following ice-shelf collapse (the period when volume losses are greatest).

2.3 Results

The ice dynamical response of 199 ice-shelf tributary drainage basins following ice-shelf collapse was calculated. Eleven ice-shelf tributary drainage basins were omitted from the analysis due to negligible expected grounding-line retreat. Results from the step-wise grounding-line retreat implementation are not presented as they showed almost identical results as the simulations with the instantaneous grounding-line retreat implementation. This was because every drainage basin had at least 25 years to adjust to the grounding-line perturbation, effectively eliminating the effect of this implementation.

2.3.1 Projected sea-level rise to 2200

SLR rise projections are highly variable across all scenarios in Experiment 1 and largely depend on the chosen thermal viability limit, emission scenario, and delay in ice-shelf collapse (Figure 2.6, 2.7). Differences range from zero SLR contribution (Figure 2.6b,c), to a maximum projected SLR for a single GCM run of ∼18.0 mm by the end of the forecast period (Figure 2.6d). Even within the same thermal viability limit, projected SLR differences are large (up to ∼18.0 mm). Across running mean scenarios, SLR projections differ in multi-model mean (black lines, Figure 2.7d-f) as well as in variance (Figure 2.7d-f), even though there is an equal time interval between the running mean scenarios. In the model runs using the more conservative -5°C isotherm and the low emissions scenario (RCP4.5; Figure 2.6a-c), only 6 GCM runs predict any ice-shelf breakup before 2100. The multi-model mean SLR contribution is ∼0.2 mm (Figure 2.6a). This number more than doubles to ∼0.6 mm in the high emission scenario, with projected SLR from individual GCM runs as high as ∼2 mm (Figure 2.7a). This underlines the importance of the choice of GCM run in projecting SLR. The SLR curves in Figure 2.7a have up to three distinct steps, each marking the response to an ice-shelf breakup event. The rate of change in the SLR curve initiated by ice-shelf breakup however is not equidistant, showing that the SLR contribution will vary between individual ice shelves. This is caused by the differing grounding-line retreat imposed on each basin and the differing number of drainage basins affected by the respective ice-shelf breakup event.

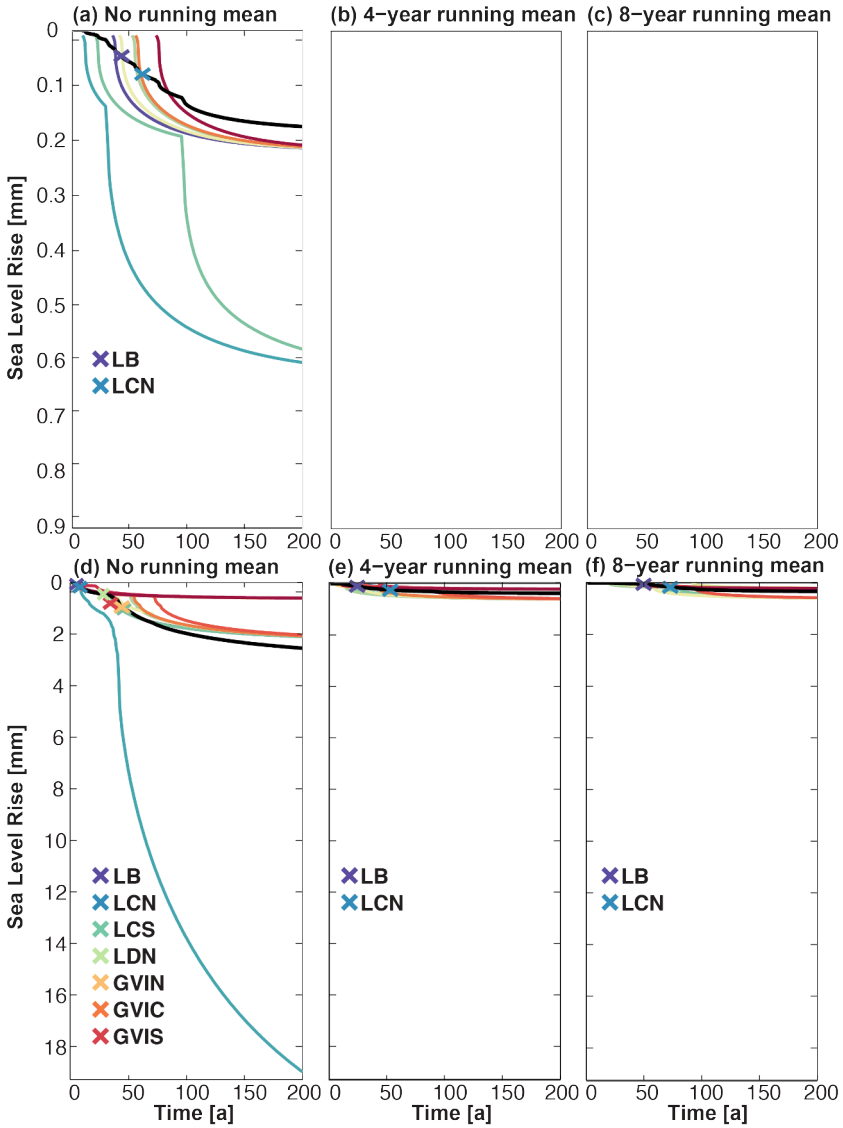

Figure 2.6: SLR curves to 2200, forced by using the -5°C isotherm (a-c) and -9°C isotherm (d-f) for RCP4.5 emission scenario. Crosses denote multi-model mean ice-shelf collapse timings. Black line shows multi-model mean SLR curve. SLR projections from individual GCMs have the same colour as in Figure 2.3.

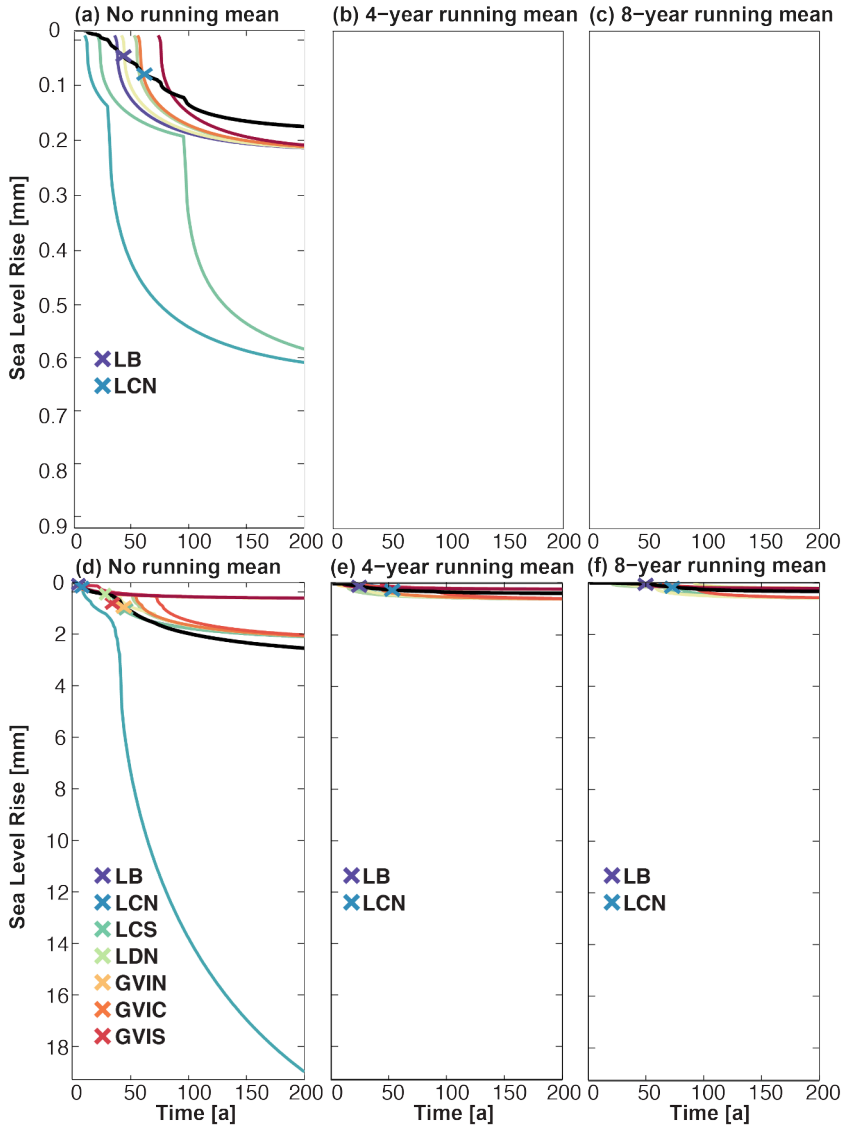

Figure 2.7: SLR curves to 2200, forced by using the -5°C isotherm (a-c) and -9°C isotherm (d-f) for RCP8.5 emission scenario. Crosses denote multi-model mean ice-shelf collapse timings. Black line shows multi-model mean SLR curve. SLR projections from individual GCMs have the same colour as in Figure 2.3.

The less conservative -9°C isotherm as the thermal viability limit provides higher SLR projections. The projections from the low emission scenario (Figure 2.6d-f) approximately follow the projected SLR using the high emission scenario and the -5°C isotherm (Figure 2.7a-c). However, one GCM run predicts the collapse of the entire George VI Ice Shelf system and thus a SLR that is ∼10 fold higher than in

any other GCM forcing (Figure 2.6d). This only occurs in the no running mean scenario, indicating a short (<4 years) but very warm period in that GCM run. Similar SLR projections are evident in the high emission scenario but across the majority of GCM runs (Figure 2.7d-f). Ice-shelf collapse of all but two Larsen D Ice Shelf entities is projected, raising the multi-model mean projection to ∼10 mm by the end of the forecast period (year 2200). The number of projected ice-shelf breakup events decreases with longer delay in ice shelf collapse and this leads to much reduced SLR projections (e.g. Figure 2.7d-f).

2.3.2 Projected sea-level rise to 2300

Results from Experiment 2 show a similar spread in projected SLR as in Experiment 1, ranging from ∼0.2 mm to ∼19 mm (Figure 2.8, 2.9). However, when corresponding scenarios are compared, projected SLR in Experiment 2 are larger. This is due to the extended simulation period allowing ice-shelf breakup to occur until 2300, though a reduction in participating GCM runs could also affect SLR projections by filtering out the extreme members, leading to a better consensus in SLR projection across GCM runs. Figure 2.9a-c suggests the former, as SLR curves do not start to lower before 2200. The difference in SLR projections between Experiments 1 and 2 varies, corroborating the particular (un)importance of certain ice shelves e.g. in the low emission scenario using the -5°C isotherm, projected SLR is similar (Figures 2.6a-c, 2.8a-c), whereas in the high emission scenario, projected SLR is ∼10 fold higher in Experiment 2 (Figures 2.7a-c, 2.9d-f).

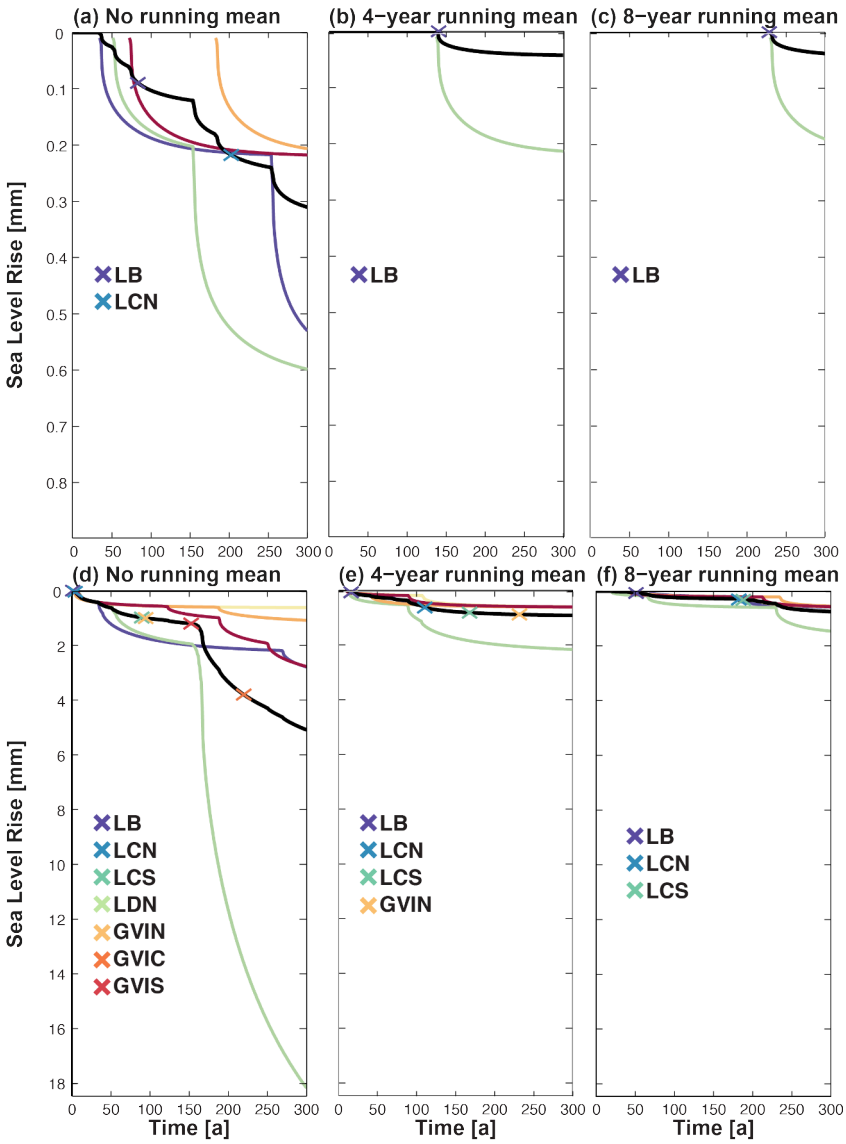

Figure 2.8: SLR curves to 2300, forced by using the -5°C isotherm (a-c) and -9°C isotherm (d-f) for RCP4.5 emission scenario. Crosses denote multi-model mean ice-shelf collapse timings. Black line shows multi-model mean SLR curve. SLR projections from individual GCMs have the same colour as in Figure 2.3.

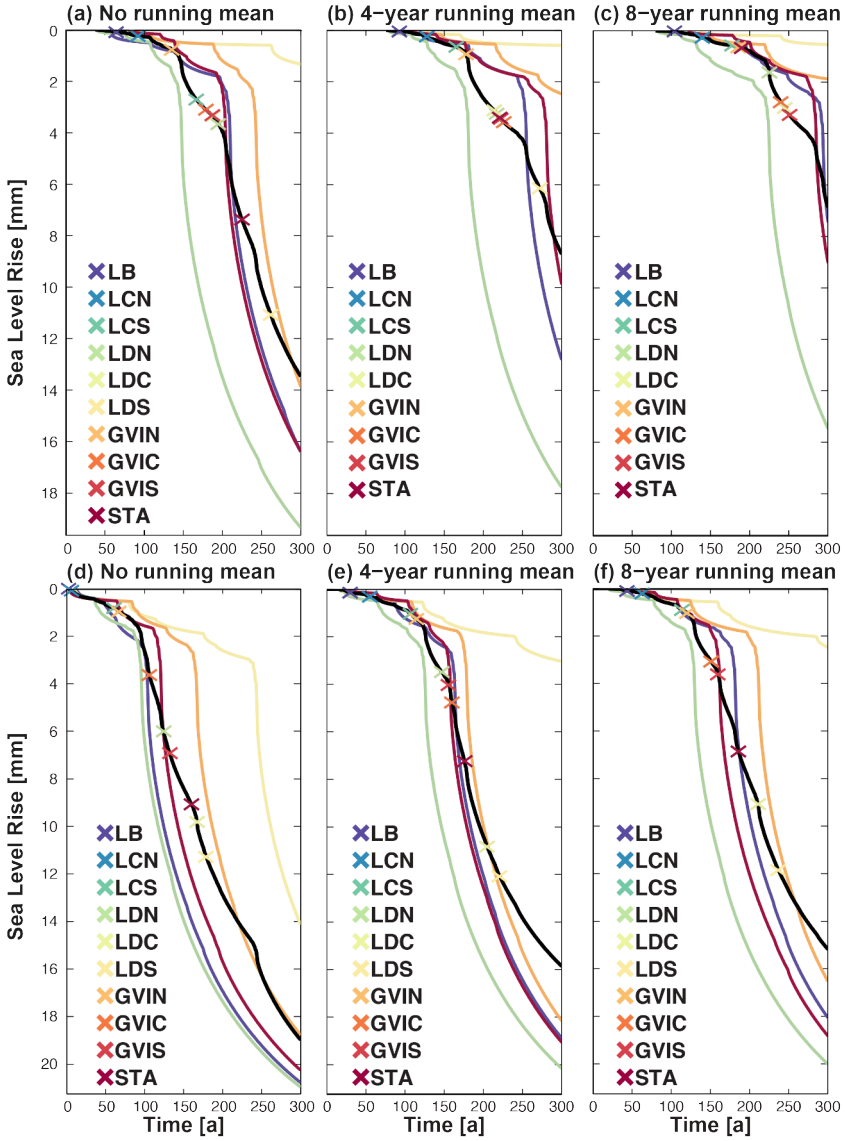

Figure 2.9: SLR curves to 2300, forced by using the -5°C isotherm (a-c) and -9°C isotherm (d-f) for RCP8.5 emission scenario. Crosses denote multi-model mean ice-shelf collapse timings. Black line shows multi-model mean SLR curve. SLR projections from individual GCMs have the same colour as in Figure 2.3.

2.3.3 Relevance of removed grounded ice

Not all of the projected SLR in Experiments 1 and 2 results from ice dynamic thinning following ice-shelf collapse but is in fact a result of grounded ice being

removed when the grounding-line retreat is applied. By design, grounding line retreat is imposed by instantaneously removing all grounded ice above sea level in the zones downstream of the prescribed new grounding line. As this ice is grounded at the time of removal, it contributes to overall SLR. We tested the importance of this process by using the coldest and warmest GCM runs of Experiments 1 and 2, and calculating the relative contribution of grounded ice removal to the overall SLR. Results show that the relative importance varies, accounting between 8.3% and 23.8% of the overall SLR. Higher percentages occur for smaller overall projected SLR but significantly decrease (∼9-10%) for SLR >10 mm. If the maximum grounding-line retreat is applied to each drainage basin, the contributions of grounded ice removal is ∼1.7 mm.

2.3.4 Regional ice dynamic thinning pattern

Ice dynamical thinning patterns are shown in Figure 2.10. In the -5°C isotherm simulations, ice dynamic thinning is limited to the northern part of the AP (Graham Land) (Figure 2.10a). Thinning rates are large locally (up to 442 m ice lost) but diminish within a few kilometers inland. However, thinning does propagate as far inland as ∼54 km. In the -9°C isotherm scenario, a similar thinning pattern is modelled in Graham Land. However, widespread thinning in excess of 200 m of ice lost (up to 492 m ice lost) occurs in the southern AP (Figure 2.10b). Thinning is also not limited to coastal areas but is transmitted much farther upstream in the southern AP, reaching a maximum inland extent of ∼136 km. Upstream of grounding lines along disintegrated ice shelves, thinning becomes more continuous, spreading well over the boundaries of drainage basins. This leads to coalescence of individual thinning patches and thus a more continuous thinning pattern (Figure 2.10b).

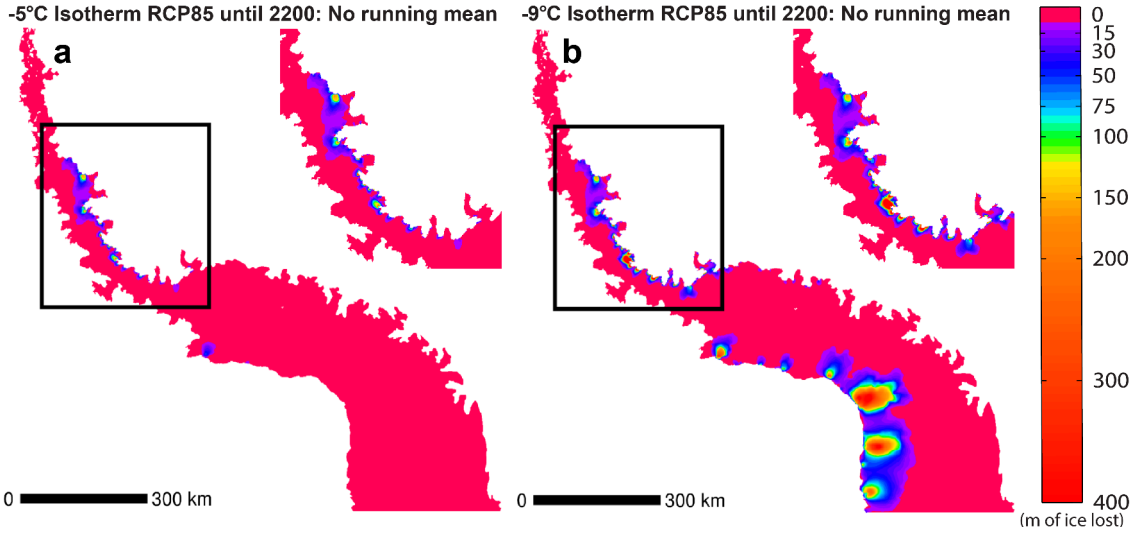

Figure 2.10: Multi-model mean thinning pattern using the high emission scenario and (a) the -5°C isotherm and (b) -9°C isotherm. Black boxes approximate location of inset map.

2.3.5 Temporal partitioning of sea-level rise

In order to assess the importance of ice-shelf entities, SLR contributions are split into intervals of 25 years for each individual ice shelf. If all ice shelves were to disintegrate, the two largest contributions to overall SLR are George VI Ice Shelf Central and George VI Ice Shelf South (Figures 2.11, 2.12). George VI Ice Shelf South comprises >75% of the total projected SLR in this scenario. However, in the first century of the simulation period, SLR contributions are evenly spread amongst the other ice shelves (Figures 2.11, 2.12).

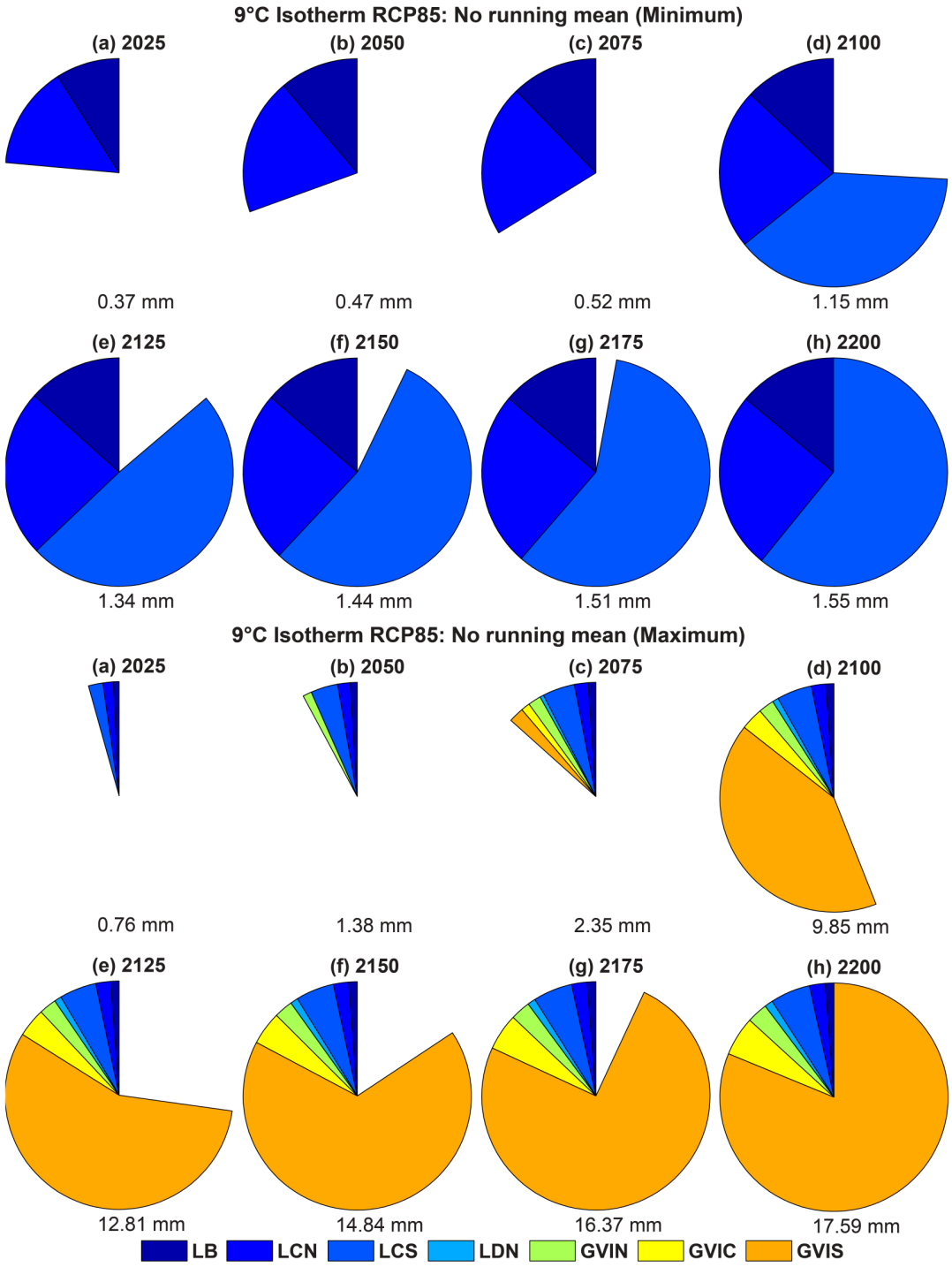

Figure 2.11: Temporal partitioning of SLR from the coldest (upper two panels) and warmest (lower two panels) GCM runs to 2200, using the -9°C isotherm high emission scenario with no running mean.

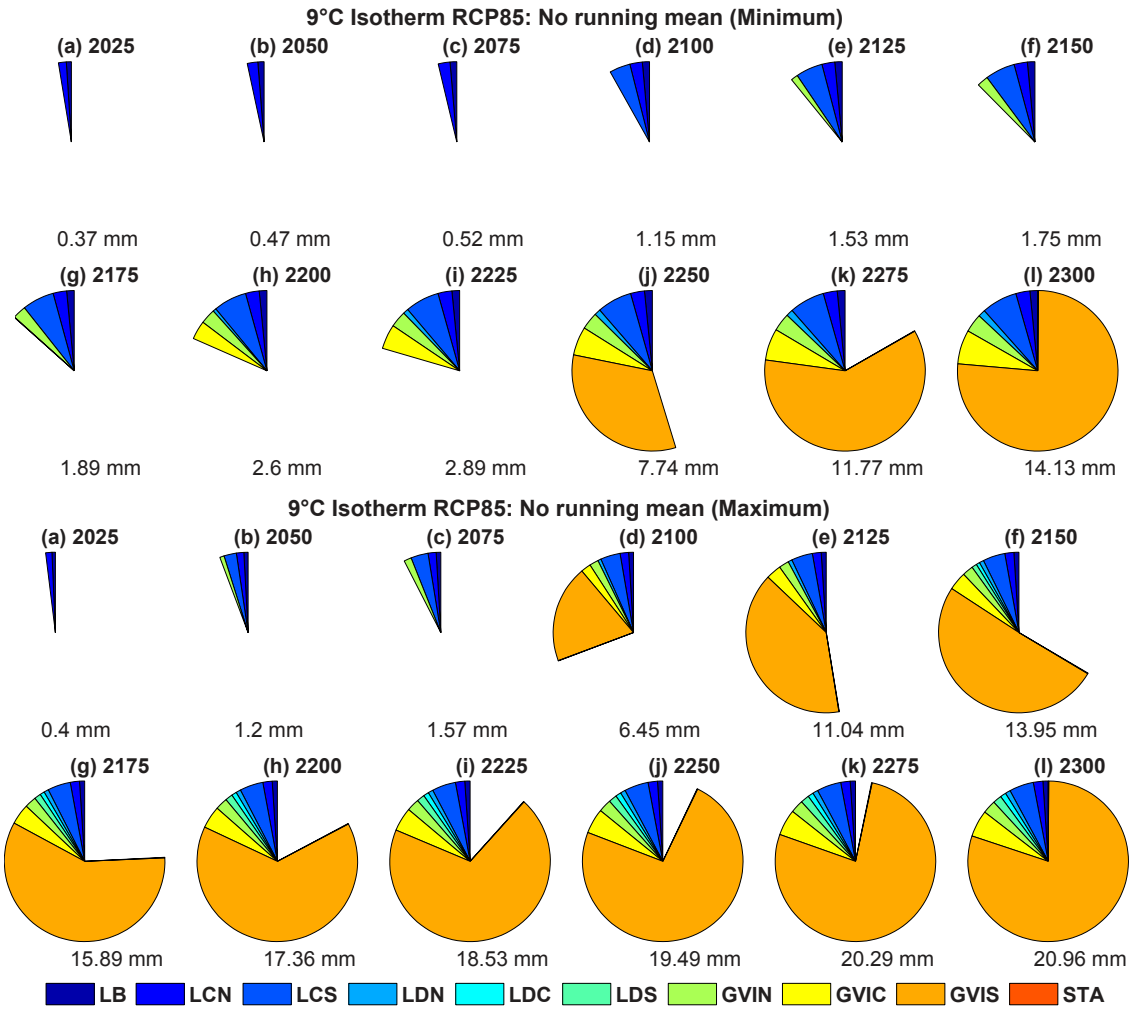

Figure 2.12: Temporal partitioning of SLR from the coldest (upper two panels) and warmest (lower two panels) GCM runs to 2300, using the -9°C isotherm high emission scenario with no running mean.

The observed spread in projected SLR between the warmest and coldest GCM run can be large (Figure 2.11), with the maximum projected SLR ∼11 fold higher than the minimum. This is unsurprising considering the importance of George VI Ice Shelf South and that it does not disintegrate in the coldest GCM (Figure 2.11). Drainage basins react quickly to the imposed grounding-line perturbation and SLR contributions are highest in the first decade following ice shelf collapse before mass losses begin to slow down (Figures 2.11, 2.12). Even though the rate of SLR decreases in subsequent time steps (Figures 2.11, 2.12), they do not reach steady state by the end of the simulation period.

2.3.6 Steady state sea-level rise simulations

Most SLR curves still display a rather steep slope at the end of the simulation period, indicating that drainage basins have not yet fully adjusted to the new imposed boundary conditions (Figure 2.9). To derive a maximum potential SLR from the imposed grounding-line retreat, each drainage basin was modelled to steady state (as defined in section 2.2.4). The experiment shows that 145 drainage basins did not reach steady state conditions within 100 years after imposition of the grounding-line perturbation. The mean adjustment period for all drainage basins is 175 years after imposition of the grounding-line perturbation, with adjustment periods as long as 602 years. The length of the adjustment period not only seems to be a function of the magnitude of the perturbation, but also a function of ice velocity, as the longest adjustment periods are almost evenly distributed between basins with either slow ice velocities or large imposed grounding-line perturbations. If all individual contributions are summed, steady state SLR amounts to ∼24.6 mm, ∼1.7 mm more than the maximum projected SLR from any of the simulations in Experiment 1 and 2.

2.4 Discussion

Projected SLR depends on a number of factors in our simulations, including: delay in ice-shelf collapse; emission scenario; the thermal limit of viability; and the quality of the input data. Therefore, the projected SLR modelled by these experiments should serve as an upper and lower bound for the more conservative -5°C isotherm threshold and the less conservative -9°C isotherm threshold respectively. The most representative SLR projections for each simulation are provided by the multi-model means (cyan lines in Figures 2.6, 2.7, 2.8, 2.9). The multi-model means for the no running mean simulations range from 0.19 mm to 9.4 mm in Experiment 1, and 0.31 mm to 19 mm in Experiment 2. If an ice density of 917 kg m^{-3} is assumed, this translates to a range of 69 Gt (0.35 Gt a^{-1}) to 3403 Gt (17 Gt a^{-1}) of ice lost for Experiment 1, and 112 Gt (0.37 Gt a^{-1}) to 6878 Gt (22.9 Gt a^{-1}) of ice lost for Experiment 2. For comparison, PIG in West Antarctica lost ice at a rate of $\sim$20 Gt a^{-1} between 1992 and 2011 (*Shepherd et al.*, 2012) and APIS as a whole lost mass at a rate of 24 $\pm$ 18 Gt a^{-1} between 2010-2013 (*McMillan et al.*, 2014). This means that the multi-model mean in the high emission scenarios of Experiments 1 and 2 provides a similar range as the entire contemporary mass loss of APIS. However, projected mass loss from individual GCM runs may exceed these values and project possible mass loss rates as high as 34.7 Gt a^{-1} over the next 200-300 years from ice dynamic thinning alone. Although the model spread in Experiments 1 and 2 provides an estimate of the uncertainties bars associated with the multi-model means, we discuss below the main sources of uncertainties in our experiments.

2.4.1 Timing of ice-shelf collapse

The ice-shelf collapse timing estimated from GCM runs using the pair of thermal viability limits follows the temperature pattern of the AP rather well. Given the prevalent east-west temperature divide in the AP (e.g. *Morris and Vaughan*, 2003), it is expected that ice shelves on the western side of the AP will disintegrate earlier than their counterparts on the eastern side at the same latitude. This pattern is captured throughout the GCM runs despite their initial coarse spatial resolution.

Although the concept of a thermal viability limit for ice shelves dates back to the 1970s (*Mercer*, 1978), little has been published on the time delay between passing of the thermal viability limit and ice-shelf disintegration. The length of the delay in the experiments is arbitrary but leads to significant changes in the estimated ice-shelf collapse timing (>50 years for some GCM runs). Most pronounced are these changes from scenario 1 (no time delay) to scenario 2 (4-year running mean). Despite the southward migration of the thermal viability limits, this migration does not occur gradually, but by step changes north or south from year to year. In some instances this may cause an early collapse in scenario 1 (Figure 2.6d) but no collapse in scenarios 2 and 3. Scenarios 2 and 3 provide more robust forecasts by being resistant to short ($\leq$4 years) anomalously warm periods. An important step towards improved future SLR projection efforts would be to include a more physically-based breakup mechanism.

To further test the robustness of the ice-shelf thermal viability tracking, we used the data from the ERA-Interim period 1979-2010 to estimate collapse timings of previous ice shelf breakup events. During the ERA-Interim period four ice shelves in the AP disintegrated: Prince Gustav Ice Shelf (1995); Larsen Inlet Ice Shelf (1989); Larsen A Ice Shelf (1995); and Larsen B Ice Shelf (2002) (e.g. *Rott et al.*, 1996; *Scambos et al.*, 2000, 2004). Using the same method as in our GCM projections, the results show that the -5°C isotherm does not forecast any collapse across all

three running mean scenarios during that period. In comparison, the -9°C isotherm suggests collapse of all four ice shelves in 1979 in scenario 1 (no running mean), collapse of Prince Gustav Ice Shelf and Larsen Inlet Ice Shelf in 1979 in scenario 2, and no ice-shelf collapse in scenario 3.

It is somewhat unsurprising that this method is incapable of estimating the exact ice-shelf collapse timing, considering that the ERA-Interim temperature data is beset by a considerable bias in the AP region (*Jones and Lister*, 2014). In the light of that, these results indicate that the -9 isotherm should be understood as a pessimistic scenario and the -5 isotherm as an optimistic scenario to estimate ice-shelf collapse. The actual collapse timing might lie somewhere in between these bounds. This is supported by the analysis of ERA-Interim temperature fields at the time of actual ice-shelf collapse, revealing an averaged mean annual temperature over the four ice shelves of -8.2°C. Instead of the thermal viability limits used in this paper, this new temperature threshold might be used as ice-shelf viability limit in future modelling experiments.

2.4.2 Grounding-line parameterisation

Despite including a variety of geometrical and ice dynamical variables into the statistical model, the overall model fit may be improved. We attribute this to a combination of the low accuracy of the mapped positional changes and the poor spatial resolution of input data (e.g. bedrock topography, ice thickness). However, where higher resolution input data was used (*Huss and Farinotti*, 2014), significant gains in the goodness of the fit were demonstrated. Nonetheless, grounding-line perturbation estimates derived from the model lie within a plausible range (0-45 km). Basing the expected grounding-line retreat on velocity leads to large grounding-line perturbation for all large and fast moving glaciers. This may result in an overemphasizing of ice velocity at the expense of other important ice

dynamical attributes such as ice thickness at the grounding line and bedrock slope. However, it is a necessary outcome of the quality and availability of input data to the statistical model. The relative importance of George VI Ice Shelf, which is based on ∼3 fold higher ice velocities than in any other drainage basins, may be overvalued in the experiments.

To investigate the sensitivity of the grounding-line retreat estimates to different acceleration factors, we perturbed the initial velocity acceleration by -20% and +20% in our speed-up scenario. The results of the sensitivity simulations provide very similar grounding-line retreat estimates compared to our reference simulation. The average grounding-line retreat is 1.4 km and 5 drainage basins show a grounding-line retreat >10 km for all three simulations. The most notable difference is in the maximum grounding-line retreats which are 35 km and 48 km for -20% and +20%, respectively (42 km for reference simulation).

We chose the -9°C isotherm RCP8.5 model run to test how much these differences affect our SLR projections. Instead of using our reference grounding line retreat estimates, we force our ice-sheet model by using the perturbed grounding-line retreat estimates. Since this model run shows the highest SLR projections, it provides the maximum uncertainty associated with our grounding line retreat estimates. For the model runs to 2200, the differences in mean SLR projection are between 0.1 mm to 2.3 mm (7% to 15%) with larger differences being modelled for larger mean SLR projections (Figure 2.7d). As mean SLR projections for the model runs to 2300 are larger than in the 2200 equivalent, absolute differences in mean SLR projections increase, ranging from 1.3 mm to 3.1 mm, but relative differences show a very similar range of 9% to 16%.

Using the perturbed grounding-line retreat estimates, we also investigated their effects on the adjustment period (the time it takes for drainage basins to reach steady state). Steady state is reached if the annual volume loss is <1% of the initial volume loss of the first year following ice-shelf collapse. The effects are negligible

as mean adjustment times for all drainage basins vary by 0.7 to 1.2 years (0.4% to 0.7%), while minimum adjustment time (12 years) and maximum adjustment time (602 years) are unaffected.

To further test the capabilities of the statistical model, we used the model to try and reproduce the grounding-line retreat rates experienced by drainage basins formerly feeding Larsen B Ice Shelf. Our mean computed grounding line retreat rate of ∼4.5 km agrees well with actual retreat rates derived from observations (*Riedl et al.*, 2004; *Rott et al.*, 2007). Satellite observations show that drainage basins of Hektoria and Crane glaciers (Figure 1.3) have experienced the most dramatic grounding-line retreat (e.g. *Wuite et al.*, 2015). This pattern is reproduced by our statistical model which computes grounding-line retreats of 56 km and 5 km for Hektoria and Crane glaciers, respectively. That the computed retreat rates do not match retreat rates from satellite observations is expected as we use input data (e.g. velocity, ice thickness, and bedrock topography) that was acquired years after the collapse of Larsen B Ice Shelf.

2.5 Conclusions

We have modelled the response of 199 ice-shelf tributary drainage basins to ice-shelf collapse and subsequent grounding-line retreat in the AP over the next 200-300 years. A total of 14 GCM projections with two emission scenarios and two thermal viability limits were used to estimate the timing of future ice-shelf collapse. The magnitude of the expected grounding-line retreat following ice shelf collapse was derived, using a statistical model and assuming immediate speed-up of tributary glaciers in response to ice-shelf collapse. Our modelling experiments have led to the following main conclusions:

1. Empirically-based ice-shelf collapse timing estimates vary across GCMs, emission scenarios, chosen thermal viability limits, and timing of delay in ice-shelf collapse. While timing differences across GCMs, emisssion scenarios, and chosen thermal viability limits were expected, our experiments reveal that the time lag between passing of the viability limit and actual disintegration of the ice shelf introduces differences in the timing of collapse of >50 years. As the collapse timing determines the timing of the application of the grounding-line perturbation, these differences propagate into the SLR projections, leading to a range of SLR projections for both experiments.

2. Owing to the application of a scenario-based approach to our simulations, each experiment provides a range of SLR projections. The most representative SLR projections for each simulation are provided by the multi-model means. Multi-model means project SLR between 0 mm to 9.4 mm for Experiment 1, and 0.04 mm to 19 mm for Experiment 2.

3. Major SLR projections are modelled in the years following ice-shelf collapse before they start to decay. The magnitude of the decay strongly depends on the applied grounding-line perturbation. In our simulations, drainage basins feeding into George VI Ice Shelf are by far contributing the most to overall SLR projections. Ice dynamic thinning in this region propagates as much as ∼135 km upstream of the initial grounding line position, whereas in the northern AP (Graham Land) thinning is limited to areas in the immediate vicinity of the initial grounding line.

4. Annual mass loss projected from ice dynamic simulations of the high emission scenario over the next 200-300 years is in a similar range to the contemporary mass loss of APIS derived from satellite observations, underlining the importance of the ice dynamic component to SLR on the centennial time scale.

Chapter 3

Future sea-level rise from tidewater and ice-shelf tributary glaciers of the Antarctic Peninsula[†]

3.1 Introduction

The AP is a mountainous and heavily glaciated region, dominated by glaciers flowing directly into the sea (henceforth tidewater glaciers) and into floating ice shelves (henceforth ice-shelf tributary glaciers). In response to the rapid warming experienced by this region over the last 50 years (*Vaughan et al.*, 2003), glaciers have contributed at an accelerated rate to global SLR in recent years (*Cook et al.*, 2005; *Wouters et al.*, 2015). In addition to an increase in near-surface air temperatures, surface waters of the surrounding ocean have warmed (*Meredith and King*, 2005). This ocean warming has been accompanied by an acceleration

[†]An edited version of this chapter was published by Elsevier. Copyright (2016) Elsevier.

(*Pritchard and Vaughan*, 2007) and retreat (*Cook et al.*, 2016) of tidewater glaciers, leading to increased ice discharge to the ocean.

Climatological changes have also affected ice-shelf tributary glaciers. Unlike tidewater glaciers, ice-shelf tributary glaciers do not flow directly into the ocean, but into a floating ice shelf. This extension of the grounded ice exerts backstress (buttressing force) on the grounded glacier upstream and thus restrains ice flow. If this buttressing force is reduced or removed, the grounded ice upstream will speed up, thin and discharge more ice into the ocean. This behaviour has been observed at several locations in the AP region (*Rott et al.*, 2002; *Scambos et al.*, 2004; *Rignot et al.*, 2004). Glaciers draining into the Prince-Gustav-Channel and Larsen A embayments are still adjusting to ice-shelf removal, some 20 years after ice-shelf collapse (*Rott et al.*, 2014; *Scambos et al.*, 2014), and are providing a significant portion to the region's SLR (*McMillan et al.*, 2014).

Abrupt ice-shelf collapse events in the past have been linked to a combination of atmospheric warming (*Vaughan and Doake*, 1996; *Scambos et al.*, 2000) and structural weakening as a result of increased basal melting (*Pritchard et al.*, 2012; *Holland et al.*, 2015). Ice-shelves are thought to be structurally weakened prior to collapse by i) hydrofracture of surface crevasses; and, ii) basal melting at the ice-ocean interface. In the latter process, warm ocean water erodes the underside of the ice shelf, thinning it and thus leaving the ice shelf more vulnerable to the process of hydrofracturing (*Shepherd et al.*, 2003). Hydrofracture of surface crevasses occurs primarily when sufficient meltwater is available at the surface of the ice shelf and can wedge open crevasses to cause catastrophic ice-shelf disintegration (*Scambos et al.*, 2004). Recent studies suggest that other ice-shelf weakening processes such as fracturing and weakening of shear margins may also be important and lead to a progressive weakening of the ice shelf prior to disintegration (*Khazendar et al.*, 2015; *Borstad et al.*, 2016). A prime example of this is the progressive mechanical weakening of the remnant Larsen B Ice Shelf over the last 15 years (*Borstad et al.*,

2016). The importance of these processes may, however, vary for individual ice shelves.

While projections of the SMB are forecasted to provide a negative contribution to sea level, this is expected to be offset by sea-level rise contributions from ice dynamical changes (*Barrand et al.*, 2013b). Owing to their short response times to ice dynamical perturbations (e.g. ice-shelf removal) in comparison to the rest of the AIS (*Barrand et al.*, 2013b), AP glaciers are projected to play an important role in the global SLR budget over the next century (*Barrand et al.*, 2013b; *Schannwell et al.*, 2015). Hitherto, ice-sheet modelling studies of the AP have focused on SLR projections from ice-shelf tributary glaciers, ignoring any contributions from tidewater glaciers (*Barrand et al.*, 2013b; *Schannwell et al.*, 2015). Given the observed acceleration and retreat of most tidewater glaciers (*Cook et al.*, 2005; *Pritchard and Vaughan*, 2007), this may lead to a substantial underestimation of the SLR contribution from the AP. In this chapter, we present the first comprehensive modelling study of SLR projections from both tidewater and ice-shelf tributary glaciers of the AP. Building on the work of *Schannwell et al.* (2015), ice-shelf collapse timing is not determined by thermal viability limits, but is instead based on the total number of melt days - a more direct and physically-based link to the process of hydrofracture. Daily, rather than monthly near-surface temperature projections are used to provide more sensitive timing estimates of future ice-shelf collapse events. To estimate grounding-line retreat in response to ice-shelf removal, a new statistical framework is introduced that builds on previous work by *Schannwell et al.* (2015), improving their statistical parameterisation by relating expected grounding-line retreat to the degree of buttressing. Buttressing at the grounding line of each drainage basin is calculated by dividing the normal pressure in presence of an ice shelf by the ocean pressure acting when no ice shelf is present. The combined SLR contribution over the next 300 years is computed, including for the first time the largest 235 tidewater glaciers throughout the northern AP. In addition to this,

volume responses of the largest 215 ice-shelf tributary glaciers are simulated. These 450 drainage basins cover a total of 77% of the AP's area, providing a comprehensive coverage of APIS.

3.2 Data and methods

3.2.1 Climate data and preprocessing

In order to estimate the timing of future ice-shelf collapse events, daily near-surface temperature fields from 13 GCMs from CMIP5 (*Taylor et al.*, 2011) were selected using RCP4.5 (*Vuuren et al.*, 2011) and RCP8.5 emission scenarios. The selection of the GCM forcings is provided in Figure 3.1 and follows *Schannwell et al.* (2015). Temperature projection fields were bias-corrected against monthly ERA-Interim data from the European Centre for Medium Range Weather Forecasts (ECMWF; *Dee et al.*, 2011) by shifting the future temperature fields by the average bias for each month between the GCM and ERA-Interim temperatures over the period 1979-2005 (*Radic et al.*, 2014). The bias-corrected temperatures were then compared to surface station data (Table 3.1) from the AP.

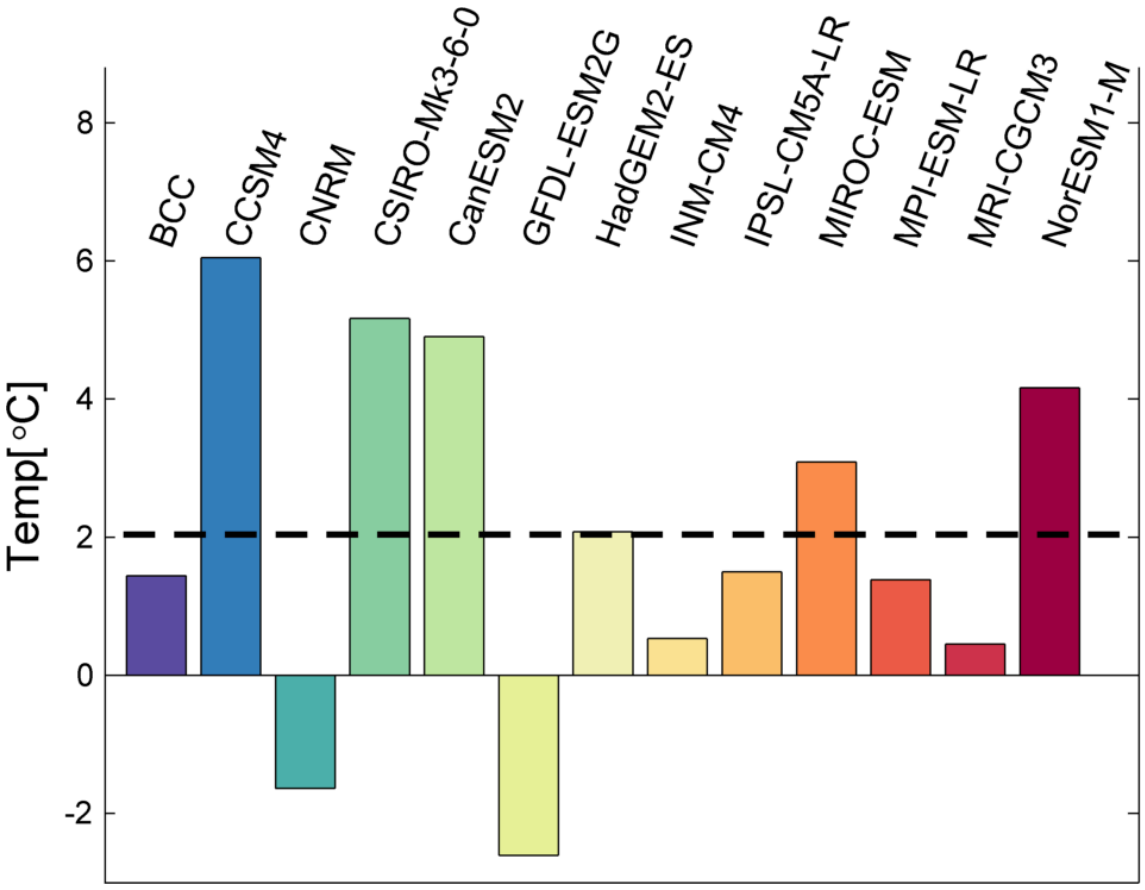

Figure 3.1: Near-surface temperature bias in comparison to ERA Interim from 1979-2005. Dashed black line indicates multi-model mean (2.0±2.6°C).

The remaining temperature difference between bias-corrected temperature fields and surface station data is attributed to an inaccurate height representation in the temperature fields caused by the relative coarse spatial resolution of the models (∼0.75°). Owing to the rugged topography of the AP, this can introduce significant temperature differences (*Jones and Lister*, 2014). To correct for this, temperature fields were shifted by a temperature-height correction factor derived for each month from every station. As most surface stations are clustered in the north of the AP, temperature data from automatic weather stations were additionally included to improve spatial coverage (Figure 3.2). Height correction factors were then bi-linearly interpolated and extrapolated to provide an ice-sheet-wide correction map for each month.

Station	ID	Type	Lat	Lon	Height	Model Height
Bellinghausen	BEL	Surface	-62.2	-58.9	16	18
Biscoe Island	BSI	AWS	-66.0	-66.1	20	244
Bonaparte Point	BPP	AWS	-64.8	-64.1	8	310
Cape Adams	CAD	AWS	-75.0	-62.5	25	125
Deception	DEC	Surface	-63.0	-60.7	8	38
Dismal Island	DSI	AWS	-68.1	-68.8	10	116
Dolleman Island	DMI	AWS	-70.6	-60.9	396	67
Fossil Bluff	FBF	AWS	-71.3	-68.3	66	536
Jubany	JBY	Surface	-62.2	-58.6	4	18
Kirkwood Island	KWI	AWS	-68.3	-69.0	30	116
Limbert	LIM	AWS	-75.9	-59.2	58	-21
Marambio	MRB	Surface	-64.8	-64.1	198	23
Marsh	MSH	Surface	-62.2	-59.0	10	18
Racer Rock	RRK	AWS	-64.1	-61.6	17	151
Sky Blue	SKB	AWS	-74.8	-71.5	1556	1451
Uranus Glacier	UGL	AWS	-71.4	-68.8	753	445

Table 3.1: List of weather stations used to compute the statistical lapse rate. Exact locations are shown in Figure 3.2. Heights are in masl. Model Height refers to the elevation of the ERA-Interim pixel closest to the respective station. AWS = Automatic Weather Station.

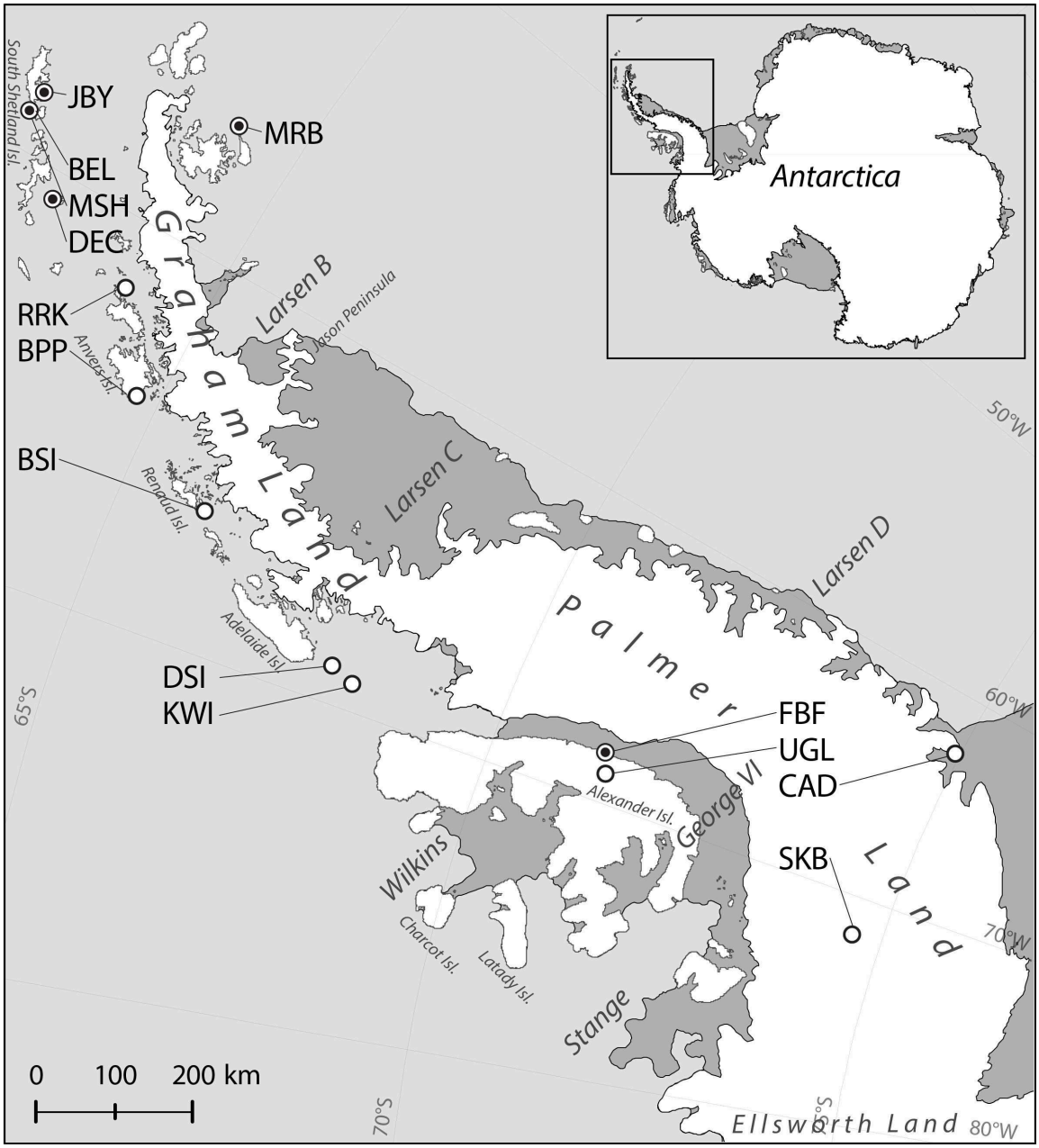

Figure 3.2: Location map of the AP and meteorological stations. Full names and details are provided in Table 3.1. Climate stations are denoted with a bullseye symbol, automatic weather stations with an unfilled circle symbol. Limbert station is off the map and not displayed (adapted from *Barrand et al.*, 2013a).

The same sample of GCMs was selected for monthly ocean surface temperature fields which were bias-corrected against the Extended Reconstructed Sea Surface Temperature (ERSST) v4 reanalysis product (*Huang et al.*, 2015) using the same methods as for the surface temperature fields. A plot of the bias for each GCM is provided (Figure 3.3).

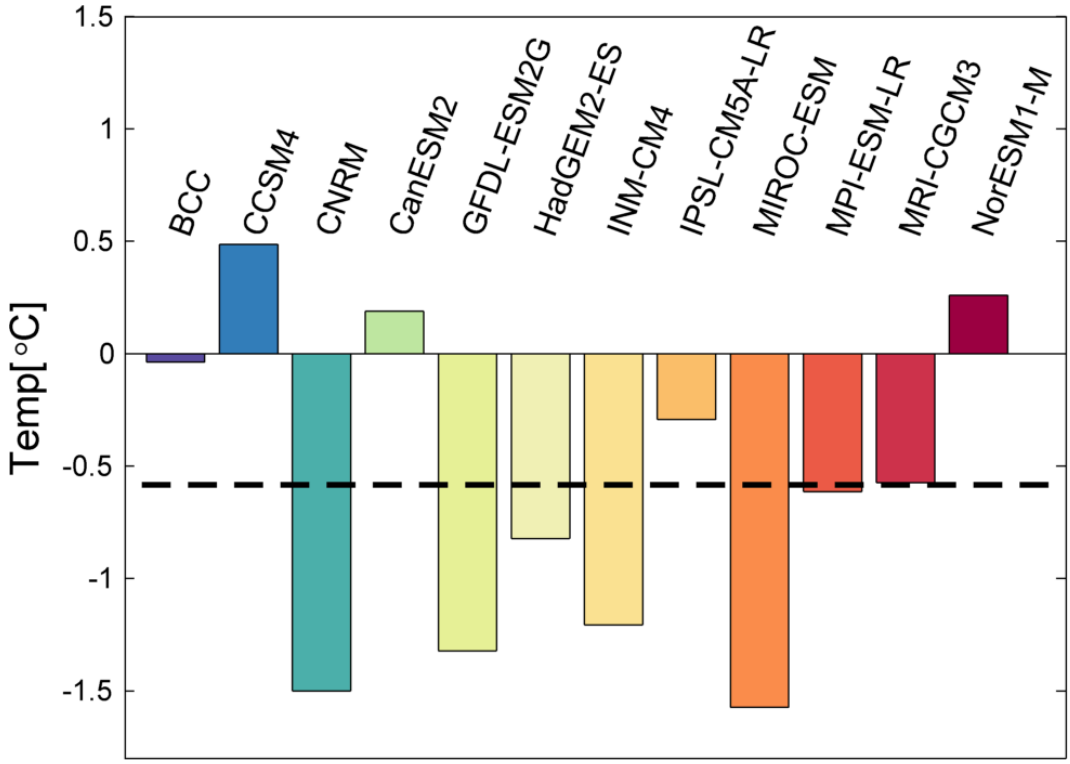

Figure 3.3: Ocean temperature bias in comparison to ERSST v4 from 1979-2005 for each GCM. Dashed black line indicates multi-model mean (-0.6±0.7°C).

3.2.2 Tidewater glaciers

A substantial portion of the mass loss of ice sheets and near-polar glaciers comes from calving (*Rignot and Kanagaratnam*, 2006; *Benn et al.*, 2007b; *Barrand et al.*, 2013c). While the importance of iceberg calving has been recognised and a number of empirical calving laws have been proposed (*Brown et al.*, 1982; *van der Veen*,

1996; *Benn et al.*, 2007a; *Alley et al.*, 2008; *Luckman et al.*, 2015), modelling iceberg calving remains a major source of uncertainty in ice-sheet models (*O'Leary and Christoffersen*, 2013). Unlike the rest of the AIS, the AP is located in a maritime climate, experiencing significant surface melt during the austral summer. These characteristics, combined with small to medium-size calving fronts, demonstrate strong similarity to tidewater glacier systems in Alaska, Svalbard, and coastal Greenland. In the absence of a universal calving law, a scenario-type approach was employed utilising three different types of calving criteria which have been used to successfully simulate calving front retreat in at least one of these regions (*Brown et al.*, 1982; *van der Veen*, 1996; *Luckman et al.*, 2015). Each calving criterion is assessed in a separate simulation.

The first criterion (henceforth water depth) relates calving rate to water depth (e.g. *Brown et al.*, 1982), using the updated formula from *Pelto and Warren* (1991)

$$V_c = 70 + 8.33 D_w, \tag{3.1}$$

where V_c is the calving rate in $m\ yr^{-1}$ and D_w is the water depth in m at the calving front.

The second criterion (henceforth flotation criterion) follows *van der Veen* (1996) who argues that the calving front position is controlled by water depth and ice thickness, following the relationship:

$$H_c = \frac{\rho_w}{\rho_i} D_w + H_0, \tag{3.2}$$

where H_c is the critical thickness, ρ_w and ρ_i are water and ice densities, respectively, and H_0 represents the minimum thickness above the flotation thickness. Based on modelling studies from Columbia Glacier, Alaska (*van der Veen*, 1996), this parameter is set to 50 m in our experiments. Equation 3.2 does not provide a calving rate, but rather states that if the calving front thickness becomes less than

a critical thickness H_c, the calving front becomes unstable and retreats by calving icebergs.

Recent studies have highlighted the importance of ocean temperatures and submarine melting to calving (e.g. *Straneo et al.*, 2010; *Luckman et al.*, 2015). *Luckman et al.* (2015) derived a linear relationship between water temperature and calving rate for 3 tidewater glaciers in Svalbard. Due to the climatic similarities between AP glaciers and Svalbard glaciers, the linear law (henceforth ocean criterion) was adopted, following the form:

$$V_c = 0.35 \times T_o, \tag{3.3}$$

where V_c is in m per month and T_o is the ocean temperature between 20-60 m in °C. Instead of ocean temperatures between 20-60 m, ocean induced calving simulations are forced by monthly ocean surface temperature projections. Ocean surface temperatures do not provide a good predictor for forecasting short term calving trends as these lead frontal ablation by 1-2 months (*Luckman et al.*, 2015). However, since long-term calving behaviour is investigated, use of ocean surface temperatures is justified. This is corroborated by a comparison over the model domain, between 1995-2004, of mean ocean surface temperatures and temperatures at 20-60 m depth, from the World Ocean Database (*Levitus et al.*, 2013). This comparison provided a mean decadal temperature difference of 0.19±0.18°C between the two data sets. A maximum distance of 100 km between calving front and ocean pixel was selected, resulting in omission of the CSIRO GCM from further analysis.

3.2.3 Ice-shelf tributary glaciers

In order to model the ice dynamic contribution from ice-shelf tributary glaciers, two important parameters need to be estimated: i) ice-shelf collapse timing and ii) the expected grounding-line retreat in response to ice-shelf removal.

Ice-shelf collapse timing is computed here according to the total number of melt days in a melt year, a direct link to the physical process of hydrofracture. Several studies noted that immediately prior to the collapse of Larsen B Ice Shelf, the number of melt days and thus the number of observed melt ponds increased dramatically (e.g. *Scambos et al.*, 2003; *van den Broeke*, 2005). A shelf collapse melt day threshold of 102 days was calculated based on observational data from QuikSCAT microwave measurements over Larsen B Ice Shelf (*Barrand et al.*, 2013a), a melt day threshold similar to a range of previously reported values (*Scambos et al.*, 2003; *van den Broeke*, 2005). Future melt days and ice-shelf collapse timing were computed from an ensemble of 13 CMIP5 GCM runs (see section 3.2.1; Climate data and preprocessing).

Ice flux across the grounding-line is restrained in the presence of an ice shelf (*Schoof*, 2007). Following *Gudmundsson* (2013) the normalised buttressing factor is computed:

$$\Theta = \frac{N}{N_0}, \tag{3.4}$$

where N is the normal pressure in presence of an ice shelf, defined by

$$N = \vec{n}_{gl}^{T} \left(R\vec{n}_{gl} \right). \tag{3.5}$$

N_0 is the ocean pressure acting normal to the grounding when no ice shelf is present

$$N_0 = \frac{1}{2}\rho g h_{gl} \tag{3.6}$$

The vector $\vec{n}_{gl}$ is the unit normal to the grounding line and,

$$R = 2\eta \begin{pmatrix} 2\frac{du}{dx} + \frac{dv}{dy} & \frac{1}{2}\left(\frac{du}{dy} + \frac{dv}{dx}\right) \\ \frac{1}{2}\left(\frac{du}{dy} + \frac{dv}{dx}\right) & 2\frac{dv}{dy} + \frac{du}{dx} \end{pmatrix}, \tag{3.7}$$

where η is the viscosity, $\rho = \rho_i\left(1 - \frac{\rho_i}{\rho_w}\right)$, and h_{gl} is the ice thickness at the grounding line.

Defined by equation 3.4, drainage basins are buttressed when $0 \leq \Theta \leq 1$; the ice shelf is actually pulling the grounded ice when $\Theta > 1$; and drainage basins are overbuttressed when $\Theta < 0$. Overbuttressed (or $\Theta < 0$) means that ice slows down as it approaches the grounding line, and mass conservation would require that ice thickens towards the grounding line ($\frac{dh}{dx} > 0$). Θ was computed for each drainage basin using velocity data from *Rignot et al.* (2011b), viscosity data from output of an ice-sheet model inversion of surface velocity data (*Arthern et al.*, 2015), and ice thickness data from *Huss and Farinotti* (2014) where available and BEDMAP2 (*Fretwell et al.*, 2013) elsewhere. 128 of the 215 ice-shelf tributary drainage basins are buttressed, 52 experience ice-shelf pulling, and 35 drainage basins are overbuttressed. Basins experiencing ice-shelf pulling are characterised by narrow ice fronts with strong shear margins. These basins are omitted from the analysis as we do not expect any ice dynamical adjustment following ice-shelf collapse. While ice dynamical changes may be expected for overbuttressed drainage basins, these glaciers were also excluded from further analysis as Schoof's flux formula (equation 1.24) is not valid for these cases.

The new parameterisation of grounding-line retreat is based on the assumption that highly buttressed drainage basins will react more to ice-shelf removal than lightly buttressed basins. Ice flux across the grounding line is computed for each drainage basin for the buttressed and the unbuttressed case ($\Theta = 1$) using Schoof's flux formula (*Schoof*, 2007). The remaining input data for Schoof's flux formula (basal drag and rheological coefficient) were obtained from output of an ice-sheet model inversion (*Arthern et al.*, 2015).

Adjustment times for drainage basins are scaled to Θ. The maximum mean adjustment time (for infinitesimal positive Θ) is set to 20 years, following observations from Larsen A Ice Shelf (*Rott et al.*, 2014) and no mean adjustment time is allowed for $\Theta = 1$. In between these bounds, the mean adjustment time is computed using Schoof's Θ exponent:

$$M_{ad} \propto \Theta^{\left(\frac{n}{m+1}\right)} \tag{3.8}$$

where M_{ad} is the mean adjustment time, n is 3, and m is 1/3.

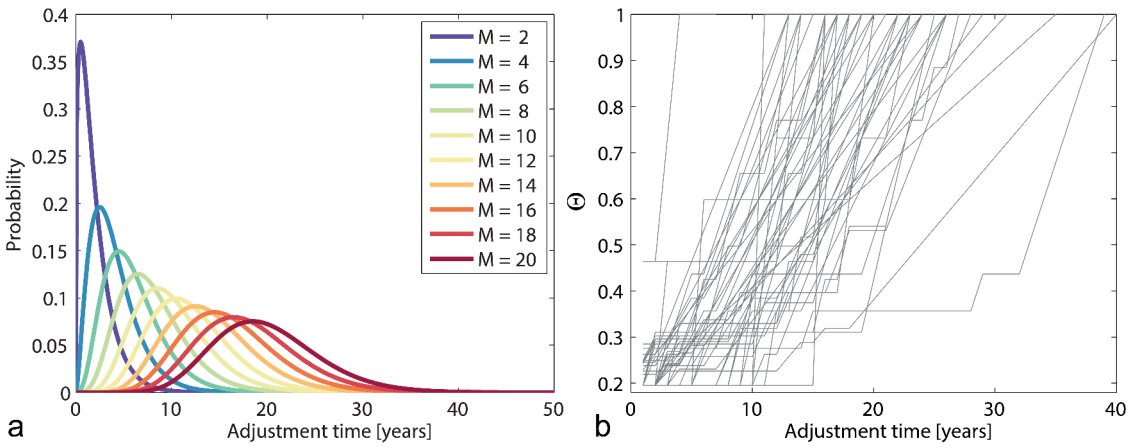

Figure 3.4: (a) Gamma distributions used in grounding-line retreat parameterisation for different mean adjustment times (M_{ad}). (b) Sample of 100 random step-response functions for corresponding $M_{ad} = 20$ curve in (a).

As mean adjustment times are based on current observations, uncertainties are associated with adjustment times derived from equation 3.8. To account for this, we allow for uncertainty in the grounding-line retreat rates within the bounds of a mean adjustment time. These realisations are set by a gamma distribution with shape parameters $k = M_{ad}/1.5$ and $\Theta_\gamma = 1.5$. The shape parameters represent greater certainty in short adjustment times and less certainty over longer adjustment timescales, allowing wider spread around the mean adjustment time in the latter case (Figure 3.4a). For each of the 10000 computed adjustment times, a corresponding step-response function for Θ is computed (Figure 3.4b). This mimics the behaviour observed in the ASS of West Antarctica where glaciers have been observed to retreat rapidly, then remain stable, before rapid retreat commences again (*Favier et al.*, 2014).

The number of steps in the function and when these steps occur for each step-response function are randomly determined (Figure 3.4b). However, the maximum number of steps has to be smaller or equal to the adjustment time. The grounding-line retreat for each realisation is then computed as follows:

$$\Delta x_{gl} = \sum_{M=1}^{M} \frac{(q_{bgl_M} - q_{gl})}{h_{gl}} \tag{3.9}$$

Here, q_{gl} is the unbuttressed grounding-line flux and q_{bgl_M} is the buttressed flux for that year using the updated Θ value from the step-response function (Figure 3.4b). The retreat distance for each ice-shelf buttressed drainage basin is determined by taking the mean of the 10000 retreat realisations (see Table 3.2).

Ice shelf	Mean retreat [m]	Θ	No. of basins
Larsen B	691	0.47	6
Larsen C North	405	0.40	17
Larsen C South	215	0.59	31
Larsen D North	656	0.60	16
Larsen D Central	250	0.57	11
Larsen D South	4140	0.66	20
George VI North	1960	0.52	4
George VI Central	7310	0.69	3
George VI South	10530	0.69	8
Stange	29540	0.54	1

Table 3.2: Ice-shelf grounding-line retreat distances, mean buttressing factor (Θ), and the number of basins for each ice shelf entity.

Grounding-line retreat of >1 km is projected for 22 drainage basins. The vast majority of the drainage basins are expected to show very little retreat. The highest retreat rates are located at drainage basins which are strongly buttressed and possess thick ice at the grounding line. The least retreat in response to ice-shelf collapse is expected for the drainage basins of Larsen B (Scar Inlet) and Larsen C ice shelves (Table 3.2). This is in agreement with independent model simulations suggesting passive shelf ice at Larsen C Ice Shelf (collapse of the shelf will not induce much grounding line retreat at upstream basins (*Fürst et al.*, 2016)).

3.2.4 Model and experimental design

Ice dynamic contribution to SLR was simulated with BAS-APISM, previously shown to be suitable for the unique topographic setting of the AP (*Barrand et al.*, 2013b; *Schannwell et al.*, 2015). Our simulations comprise two experiments: i) the SLR contribution to 2300 of 235 tidewater glacier drainage basins is computed, using a range of empirically-based calving criteria. In the first simulation, iceberg calving is allowed until 2100 and in the second simulation, calving is permitted until 2300. Differing forcing periods for calving were applied to investigate their influence on sea-level projections to the end of the simulation period. In experiment ii) the end members of the calving simulation permitting calving until 2300 are combined with SLR projections from 215 ice-shelf tributary glaciers to estimate the total ice dynamic SLR contribution for the AP. Ice-shelf collapse is permitted until 2300 for all simulations.

3.3 Results and discussion

3.3.1 Sea-level rise from tidewater glaciers

Simulated SLR projections from tidewater glaciers underline their crucial importance to the regional sea-level budget of the AP region. For the simulation allowing calving to 2100, projections are between 3.2±1.6 mm and 18.6 mm, and for the experiment permitting calving to 2300, between 8.7±2.9 and 18.6 mm. Uncertainty ranges ($\pm 1\sigma$) are available for ocean criterion simulations only. Across the two experiments, differences are present in projections from the ocean criterion, indicating a considerable change in ocean forcing between the emission scenarios (Figure 3.5).

Differences in SLR projections are most pronounced in the simulations allowing calving to 2100 (Figure 3.6a). In these simulations, projections from the ocean criterion are an order of magnitude smaller than projections from the flotation and the water depth criteria. These two calving criteria project the vast majority of their total SLR by 2300 over the next 50 years. This is mainly due to the fact that a few drainage basins (e.g. Fleming Glacier, Figure 1.3) rest on bedrock located well below sea level and thus are very vulnerable to iceberg calving in the flotation and water depth criteria (see equations 3.1 and 3.2). In contrast to the projected 18.6 and 13.7 mm by 2300 from the water depth and flotation criteria respectively, SLR projections using ocean forcing are moderate, projecting 3.2±1.6 mm for the RCP4.5 and 5.0±2.3 mm for the RCP8.5 emission scenario (Figure 3.6a).

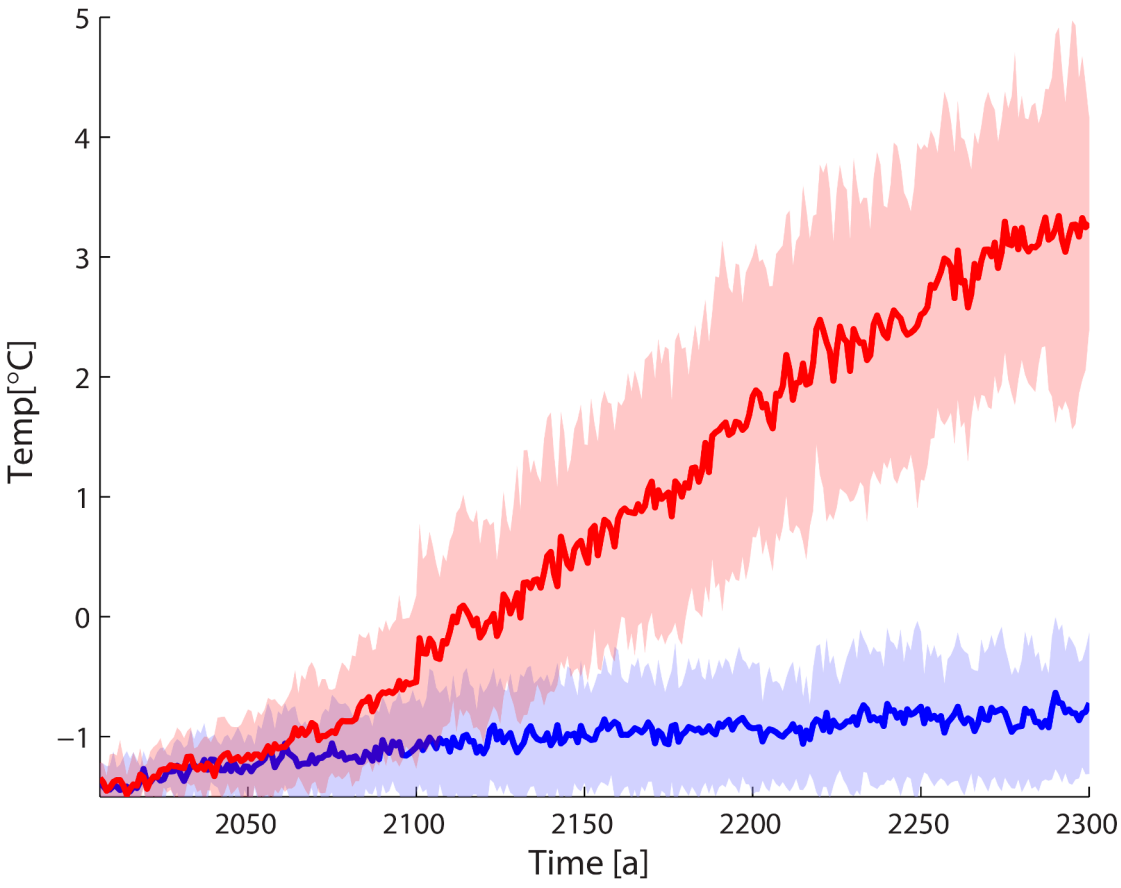

Figure 3.5: Multi-model mean ocean temperatures for the ice-sheet model domain for RCP4.5 (blue line) and RCP8.5 (red line). Shading shows (±1σ) uncertainty.

These differences in SLR projections are smaller in the simulations where iceberg calving is permitted until 2300. While SLR projections from the water depth and flotation criteria remain unchanged, projections from the ocean criterion are an order of magnitude higher and in a very similar range as the other calving criteria (Figure 3.6b). This means that for the water depth and flotation criteria, all retreat is projected to occur prior to 2100 in all simulations. In contrast SLR projections from the ocean criterion are small to 2050 (<1 mm), but increase dramatically after that. The RCP8.5 scenario projects even marginally higher SLR than the flotation criterion at 13.9±2.1 mm, while scenario RCP4.5 projects a SLR of 8.7±2.9 mm by 2300 (Figure 3.6b).

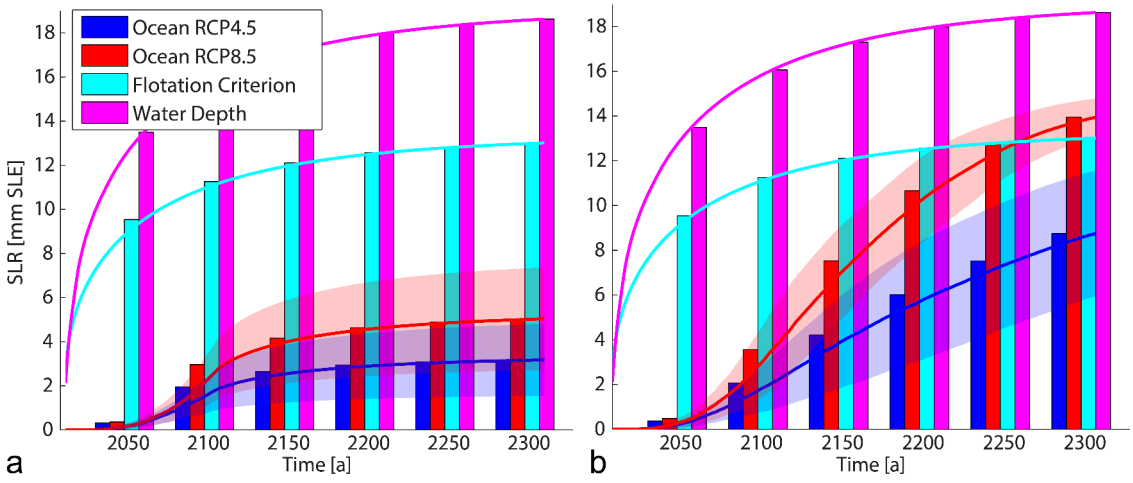

Figure 3.6: SLR projection from tidewater glaciers permitting calving front retreat to 2100 (a) and to 2300 (b). Shading shows (±1σ) uncertainty.

The larger discrepancy in SLR between the emission scenarios can be explained by the much steeper increase in ocean temperatures for the RCP8.5 scenario in the latter two centuries of the simulation period. While there is only a 1.8±0.7 mm difference in the first simulation (Figure 3.6a), this difference almost triples to 5.2±0.8 mm in the second simulation (Figure 3.6b). This is also reflected in the ocean temperature projections (Figure 3.5). In 2100, the temperature difference

between the scenarios is 0.6°C, but increases to 4°C by 2300. The total warming observed in the multi-model mean of RCP8.5 is 4.6°C (Figure 3.5). This ocean warming, however, is not spatially homogeneous. Rather, there are noticeable differences between the west and east coasts of the peninsula. To the west of the peninsula, warming is more pronounced at 0.96°C per century, compared to 0.85°C for the eastern side of the peninsula. This modelled temperature disparity between the two regions continues the pattern observed in the second half of the 20st century (*Meredith and King*, 2005).

In the absence of a universal calving law, it is important to note that none of our calving criteria are specifically tuned for the AP. BAS-APISM also cannot simulate glacier front advance. These limitations mean that the SLR numbers reported here should be understood as a first-order estimate of SLR from tidewater glaciers. While surface ocean temperatures appear to be a reasonable approximation of temperatures at depths between 20-60 m, uncertainties remain as to how well these modelled temperatures reproduce near-coastal ocean temperatures. The projected 18.6 mm from the water depth criterion should be interpreted as a maximum that can be expected from these 235 glaciers. In the simulations using this criterion, the calving front retreats at each drainage basin until the bedrock on which the glacier rests is very close to sea level.

Evaluating the suitability of calving criteria to project calving rates remains difficult. Studies investigating calving behaviour of individual glaciers in different environmental settings have noted that the processes controlling calving are multi-faceted and may vary for individual glaciers (*Nick et al.*, 2013; *James et al.*, 2014; *Luckman et al.*, 2015). Other studies have successfully reproduced calving retreat rates using simple empirical calving criteria (*Vieli et al.*, 2001; *Nick and Oerlemans*, 2006). An indication of the general agreement across the calving criteria is provided by the second simulation (Figure 3.6b), where Fleming and Prospect glacier, Wordie Bay (Figure 1.3), are the largest single contributors to

SLR regardless of the applied calving criteria, projected to contribute between 1.8-3.4 mm to SLR by 2300.

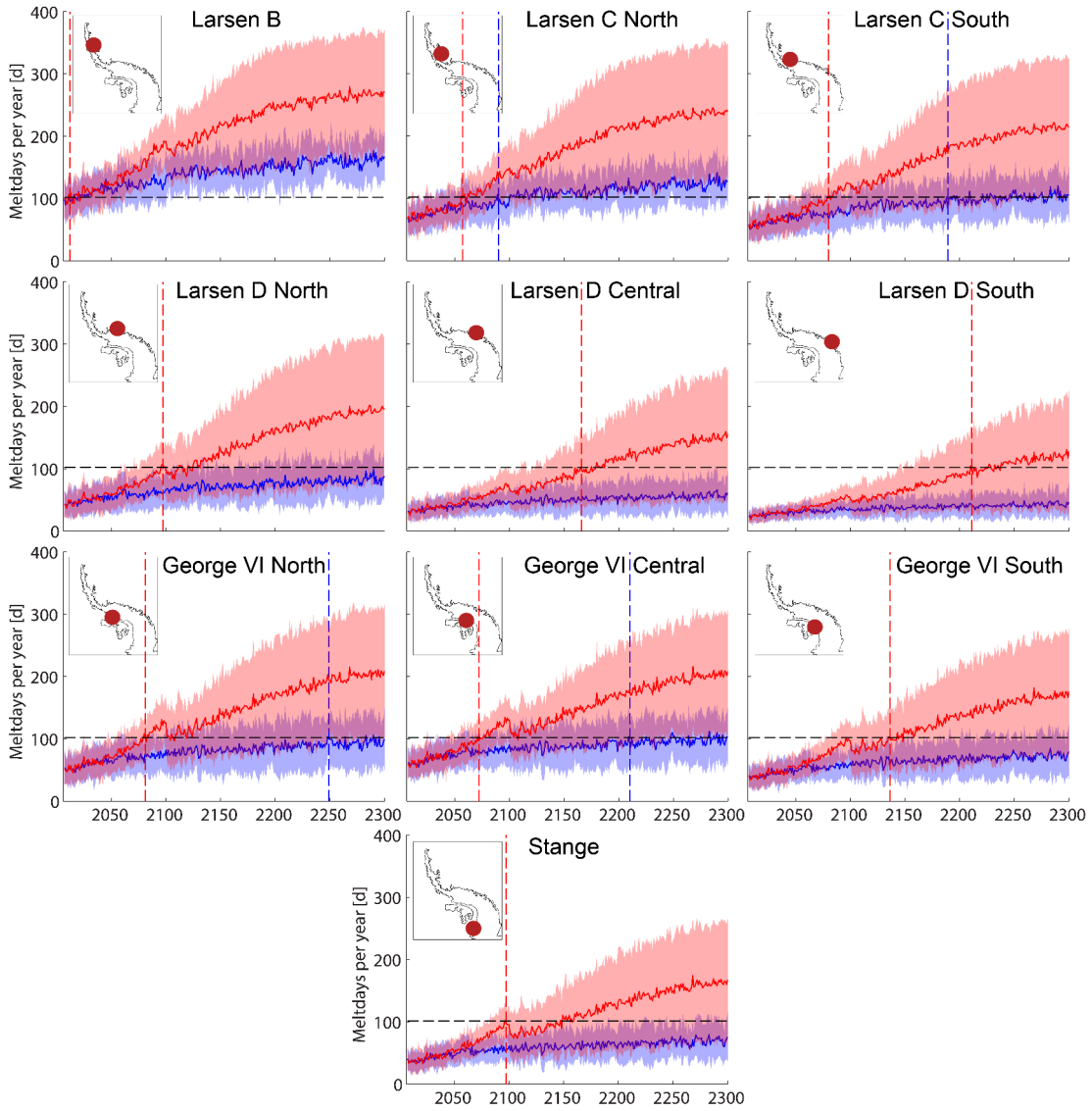

Figure 3.7: Multi-model mean melt day projections for all ice shelves for the RCP4.5 (solid blue line) and RCP8.5 (solid red line) scenarios. Shading shows ($\pm 1\sigma$) uncertainty. Dashed blue lines and dashed red lines denote ice-shelf collapse timing for the RCP4.5 and RCP8.5 scenarios, respectively. Dashed black line approximates collapse threshold. Note that for Larsen B Ice Shelf (Scar Inlet) collapse timing for both scenarios is forecasted for the same year. The dip in melt days at 2100 is due to a number of GCM projections only extending to 2100.

3.3.2 Combined ice dynamical sea-level rise

The combined SLR projections in the RCP4.5 scenario are dominated by the contributions from tidewater glaciers, accounting between 79% and 89% to the combined SLR. There is a very minor contribution from ice-shelf tributary glaciers to 2150, and their contribution to 2300 remains small at 2.4±1.5 mm. This relative unimportance is due to the absence of ice-shelf collapse (Figure 3.7). In the RCP4.5 scenario, the multi-model mean suggests disintegration of 50% of the 10 ice shelves (Figure 3.7). Only one of the ice-shelf tributary glaciers of George VI Central contributes significantly to SLR. This basin is responsible for 67% of the SLR projected from ice-shelf tributary glaciers, demonstrated by the step in the sea level curve following this shelf collapse in year 2210 (Figure 3.8).

The overall importance of ice-shelf tributary glaciers to SLR increases in the RCP8.5 scenario (Figure 3.8b). All 10 ice shelves are projected to disintegrate in this simulation (Figure 3.7). Moreover, collapse timings of ice shelves that collapsed in the RCP4.5 occur earlier in RCP8.5. The later the forecasted ice-shelf collapse in RCP4.5, the larger is the shift in timing in the RCP8.5 scenario. While there is only a 33 year shift for Larsen B North, this shift increases to 168 years for George VI North, the last ice-shelf to collapse in the RCP4.5 scenario (Figure 3.7). The collapse of more ice shelves results in much higher SLR projections from ice-shelf tributary glaciers (Figure 3.7). In contrast to the RCP4.5 scenario, ice-shelf tributary glaciers are as important as tidewater glaciers in this simulation. They contribute 51.4% and 42.4% to the 26.7±16.2 and 32.3±16.2 mm projected for the combined minimum and the combined maximum, respectively (Figure 3.8b). These projections increase by another 6±1.6 mm if overbuttressed glaciers are taken into account by setting Θ for each of these drainage basins to the minimum value (maximum buttressing) of all ice-shelf tributary glaciers. As overbuttressed drainage basins violate the Schoof flux formula, these projections should be interpreted with caution and are therefore

omitted from the total SLR projections. Since not all SLR projections from tidewater glaciers supply uncertainty ranges, uncertainty ranges for all combined SLR projections are reported as $\pm 2\sigma$ of ice-shelf tributary glacier simulations.

The relative importance of each ice shelf to overall SLR can be assessed from the step size in the SLR curve triggered by individual ice-shelf collapse responses. While some ice-shelf collapses result in no or only a very minor increase in sea level, there are two major steps present in the sea level curve (Figure 3.8b). These represent the ice shelves that were identified as the most crucial to overall SLR. By far the largest single contributor to SLR is George VI Ice Shelf South, followed by Larsen D Ice Shelf South. The former contributes 7.5±4.4 mm by 2300 or 54% of the total contribution from ice-shelf tributary glaciers, while the latter contributes 2±1.6 mm by 2300 or 14% of the total contribution. Combined, these ice shelves account for 68% of the total projected SLR from ice-shelf tributary glaciers.

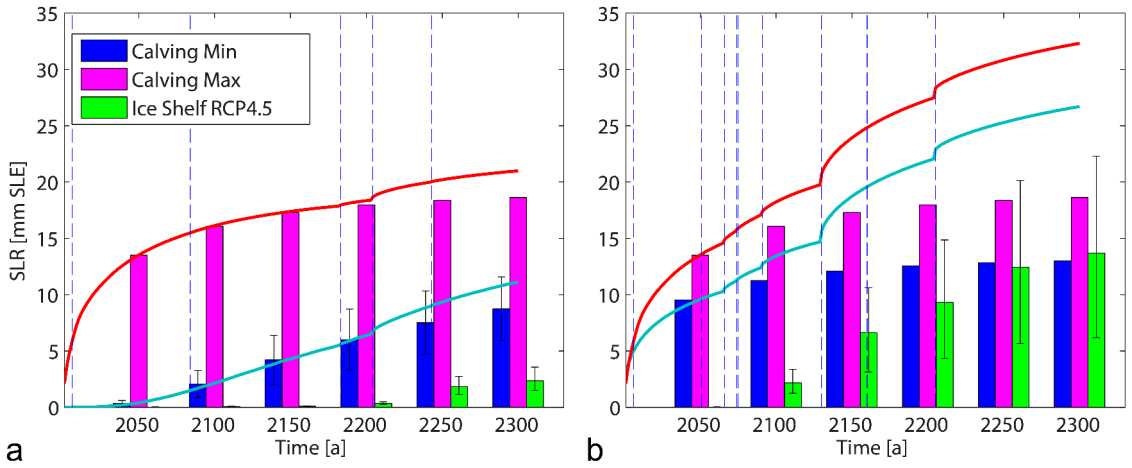

Figure 3.8: Combined SLR for RCP4.5 (a) and RCP8.5 (b) scenarios. Red and blue lines correspond to combined maximum and combined minimum projection. Dashed blue lines approximate timing of ice-shelf collapse. Error bars are displayed where available.

For ice shelves forecasted to collapse after 2100 in either the RCP4.5 or RCP8.5 scenario, there is a cold bias in the collapse timing estimates. This is due to the fact that eight GCM projections only extend to 2100, and the mean melt days after 2100 are computed from the five remaining GCM projections. For most shelves (Figure 3.7: Larsen B, George VI, and Stange), the reduction of available GCMs causes an immediate dip in melt days at 2100. This most likely leads to a delayed ice-shelf collapse forecast and thus may result in an underestimation of SLR by 2300. However, considering the little projected SLR from ice-shelf tributary glaciers in the RCP4.5 scenario, the effect is small compared to other uncertainties in this emission scenario. In the RCP8.5 scenario, the effect of delayed ice-shelf collapse on SLR projections by 2300 is higher, but still smaller than uncertainties associated with the grounding-line retreat parameterisation. A control simulation where ice-shelf collapse was imposed at 2100 for all ice shelves forecasted to collapse after 2100 in RCP8.5 led to SLR projections 2 mm larger than in the reference simulation (Figure 3.8). This provides an upper bound of this effect on SLR projections by 2300, but the uncertainty is most likely smaller than this, as some ice-shelf collapse events might not shift to be as early as 2100.

Ice-shelf collapse is based on an empirical parameterisation of the physical process hypothesised as being the principal reason for ice-shelf collapse - surface meltwater-induced hydrofracture. A melt day threshold is likely to be a function of annual accumulation as well, but here we stick to the simplest model mainly due to the lack of observations that would allow for a more complex model. Moreover, this collapse mechanism may not be the sole process driving ice-shelf disintegration (*Shepherd et al.*, 2003; *Khazendar et al.*, 2015) and thus ice-shelf collapse might be mis-forecasted. Grounding-line retreat from a gradual loss of buttressing (e.g. through ice-shelf thinning), where no collapse occurs, was also omitted. Moreover, bedrock topography is only taken into account for tidewater glacier retreat computations, omitting the potential of MISI, a self-sustained retreat

of the grounding line on retrograde sloping bedrock, in ice-shelf tributary drainage basins. While a recent study suggests that widespread MISI is unlikely in the AP (*Ritz et al.*, 2015), there is evidence that some regions may be susceptible to this mechanism (e.g. Scar Inlet and George VI Ice Shelf) (*Farinotti et al.*, 2014; *Wouters et al.*, 2015). Despite these simplifications, the implemented grounding-line retreat parameterisation predicts plausible retreat rates in agreement with theoretical considerations.

In comparison to earlier ice dynamical SLR projections from ice-shelf tributary drainage basins by *Schannwell et al.* (2015), the projections provided here are slightly higher for the RCP4.5 scenario and slightly lower for the RCP8.5 scenario. Discrepancies in SLR between *Schannwell et al.* (2015) and this study arise due to the improvement in grounding-line retreat and ice-shelf collapse parameterisations here. Unlike in the previous grounding-line retreat parameterisation, the new parameterisation permits estimation of uncertainty ranges for each simulation. Moreover, ice-shelf collapse timing is calibrated on observations, providing a more robust approximation for future collapse estimates. Despite the substantial improvements implemented in the model simulations in this chapter, the effect on the magnitude of SLR projections by 2300 is rather small compared to projections in Chapter 2 (within 3 mm of each other). Even though there is very little difference in SLR projections between the two studies, the ice-shelf collapse parameterisation is now based on a physical process and the grounding-line retreat parameterisation is based on theoretical considerations. These improvements alone justify preferring the parameterisations implemented here as they are more process based than projections presented in Chapter 2.

3.3.3 Uncertainty assessment

In order to test the robustness of the modelled SLR projections a suite of sensitivity experiments was performed. Since SLR projections from tidewater glaciers should be understood as a first-order estimate and the three calving criteria provide an envelope of future scenarios, the sensitivity experiments concentrate on ice-shelf tributary SLR contributions.

There are two main sources of uncertainty: climate (ice-shelf collapse timing) and grounding-line retreat parameterisation. The influence of climate variability on SLR projections is demonstrated by the difference between the two emission scenarios. In RCP8.5, projections are ∼6 fold higher than in RCP4.5. Nonetheless, the importance of ice-shelf collapse timing in a worst-case scenario is relatively moderate. The most extreme scenario with immediate collapse of all fringing ice shelves leads to an increase of 3.7 mm (27%) in comparison to the projection from RCP8.5.

How much the position of the grounding line changes in response to ice-shelf collapse is of crucial importance for SLR projections from ice-shelf tributary glaciers. In the parameterisation implemented here, the mean adjustment time is scaled to buttressing and is based on available observations from Larsen A Ice Shelf. Since ice dynamical changes are still ongoing in this area, maximum adjustment time may be underestimated. Grounding-line retreat rates for each basin were computed using Schoof's flux formula. To investigate the sensitivity of the results, crucial parameters such as adjustment time and all input data to the flux formula were perturbed by ±20%. Results show that by far the most important parameter is ice thickness at the grounding line. SLR projections from all other perturbed parameters vary by <46% (<4.7±1.7 mm) in comparison to the reference simulations and lie all within the reported uncertainty ranges. For perturbed ice thicknesses however, SLR projections vary by up to ∼400% (53.2±16.6 mm),

increasing SLR projections in RCP8.5 to 66.9±25 mm, more than double the SLR projected for the combined RCP8.5 reference simulation. These results highlight the key importance of accurate estimates of ice thickness at glacier grounding lines. To investigate the robustness of the results to perturbations to ice velocity, the velocity map was perturbed by adding normally distributed noise (σ = 1 SD of unperturbed velocity map) to the unperturbed velocity map. Ice velocity was used to estimate buttressing at each drainage basin. The perturbed velocity map was used to compute new Θ values for the 128 modelled drainage basins. Of the 128 normally buttressed basins in the reference simulation, 26 change to being overbuttressed and 31 to being unbuttressed. This leaves 71 drainage basins for the perturbed model simulation. Despite the smaller number of drainage basins, change in SLR for the RCP8.5 scenario is negligible (∼1%) in comparison to the reference simulation, indicating an increase in buttressing for these 70 drainage basins. Average buttressing for these basins increases from 0.59 to 0.43, negating the effect of fewer drainage basins modelled.

3.4 Conclusions

This chapter has presented the first comprehensive modelling study of SLR projections from both tidewater and ice-shelf tributary glaciers of the AP. In total, the ice dynamical response of 450 drainage basins, comprising 77% of the AP's area, was computed. Tidewater glaciers are an important contributor to the ice dynamic SLR projections from the AP. Omission of tidewater glaciers leads to an underestimation of SLR by >50%. In the RCP4.5 scenario, SLR projections are dominated by tidewater glaciers contributing >75% of the combined SLR, while tidewater and ice-shelf tributary glaciers contribute about the same to total SLR in the RCP8.5 scenario. If all ice shelves disintegrate, George VI Ice Shelf is the largest

single contributor, accounting for 9.8±5.5 mm (70%) of the total SLR projected from ice-shelf tributary glaciers. This agrees well with an earlier modelling study (*Schannwell et al.*, 2015) and is consistent with present-day observations of AP ice-sheet mass balance (*Wouters et al.*, 2015).

Sensitivity results show uncertainties in SLR projections remain due to calving, ice-shelf collapse, and grounding-line retreat parameterisation. SLR projections for ice-shelf tributary glaciers are highly sensitive to ice thickness and to a lesser extent ice velocity. To reduce uncertainties further in future simulations, accurate ice thickness and velocity maps are required for computation of buttressing and ice flux across the grounding line.

APIS is projected to contribute between 11±2 mm and 32±16 mm to global SLR by 2300, depending on emission scenario. This corresponds to an annual contribution of 0.04±0.01 mm a^{-1} and 0.11±0.05 mm a^{-1} over the next three centuries, respectively. For comparison, the SLR contribution from the entire AIS derived from satellite observations between 2003-2013 was 0.25±0.07 mm a^{-1} (*Martín-Español et al.*, 2016). These findings underline the continued importance of ice dynamic SLR from the AP, even though the AP comprises only 1% of the total AIS area.

Chapter 4

Sea-level projections from the Antarctic Peninsula Ice Sheet response to Larsen C and George VI ice shelf collapse

4.1 Introduction

APIS is contributing at an accelerating rate to SLR (e.g. *Shepherd et al.*, 2012; *Martín-Español et al.*, 2016). Most of this recent acceleration is owed to changes in ice dynamics (*Wouters et al.*, 2015; *Martín-Español et al.*, 2016) through increase of solid ice discharge from the ice sheet's interior to the margins. Outlet glaciers in the peninsula have sped-up (*Rignot et al.*, 2004; *Rott et al.*, 2014), thinned (*Scambos et al.*, 2014), and retreated (*Cook et al.*, 2005) in response to a loss of buttressing through ice-shelf retreat (*Cook and Vaughan*, 2010) and collapse (*Rott et al.*, 1996; *Scambos et al.*, 2003). Ice-shelf collapse events have been closely linked to a climatic

viability limit approximated by the -9°C mean annual isotherm (*Mercer*, 1978; *Vaughan et al.*, 2003). As this temperature limit is expected to migrate further south in the future (*Scambos et al.*, 2000, 2003; *Schannwell et al.*, 2015), more ice shelves fringing the AP may become unstable and retreat or collapse. Larsen C Ice Shelf is the largest and northern-most remaining ice shelf (Figure 4.1a) and, based on the thermal viability limit, is the ice shelf with the most immediate threat of disintegration. This threat has led to increased research interest from the glaciological community to better understand what processes control ice-shelf stability (e.g. *Jansen et al.*, 2010; *Kulessa et al.*, 2014; *McGrath et al.*, 2014; *Holland et al.*, 2015; *Jansen et al.*, 2015).

Over the last decade, Larsen C Ice Shelf has thinned by 3.8±1.1 m (*Paolo et al.*, 2015) due to a combination of changes in ice dynamics, ocean and atmospheric forcing (*Holland et al.*, 2015). In spite of these changes, the shelf was considered to be in a stable configuration (*Jansen et al.*, 2010) until an established rift started to propagate rapidly in 2014 (*Jansen et al.*, 2015). The rift is expected to lead to the largest calving event in Antarctica since the 1980s, reducing the area of the ice shelf by 9-12% and potentially threatening its stability (*Jansen et al.*, 2015). The calving event would leave the shelf in a similar state as Larsen B Ice Shelf immediately prior to its collapse in 2002 (*Jansen et al.*, 2015). However, recent ice-sheet modelling efforts (*Schannwell et al.*, 2015, 2016) indicate that in terms of SLR potential and buttressing (*Fürst et al.*, 2016) George VI Ice Shelf is more important than Larsen C Ice Shelf. Unlike most of the outlet glaciers feeding Larsen C Ice Shelf, large areas of the main outlet glaciers in the George VI embayment are located on bedrock below sea level (Figure 4.1b), potentially making the region vulnerable to the MISI mechanism - a self-sustaining retreat of the grounding line (e.g. *Schoof*, 2007). Based on the BEDMAP2 (*Fretwell et al.*, 2013) dataset, 2.1 mm and 46.6 mm SLE ice volume are contained below sea level in the Larsen C and George VI drainage basins, respectively (Figure 4.1b).

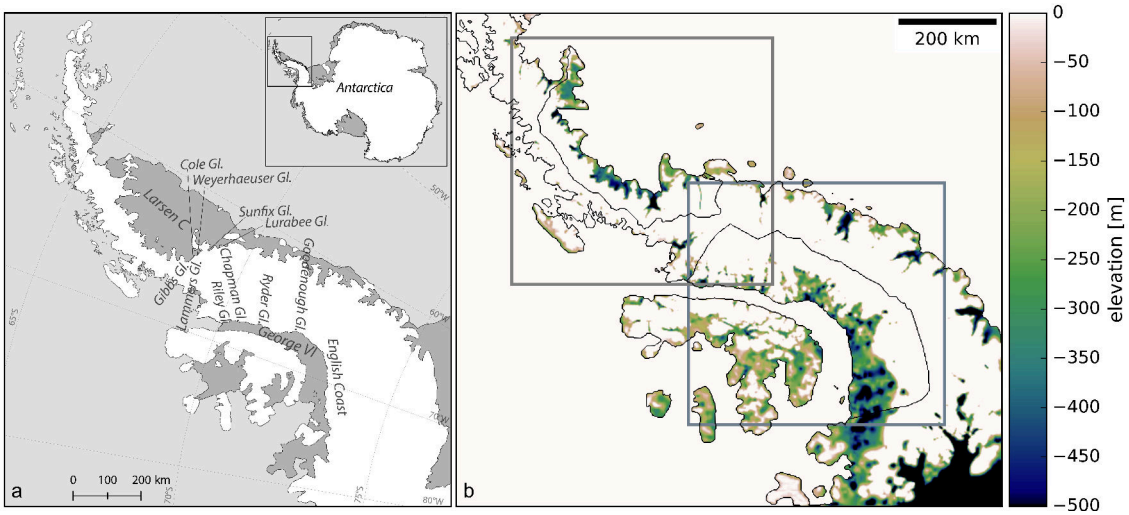

Figure 4.1: (a) Location map of the AP including locations of Larsen C and George VI ice shelves and localities mentioned (adapted from *Barrand et al.*, 2013a). (b) Bedrock elevations below sea level for the AP from BEDMAP2 (*Fretwell et al.*, 2013). Black polygons denote ice-sheet model domains. Grey boxes approximate locations of zoom-ins.

George VI Ice Shelf is the second largest ice shelf in the AP region and is fed by larger and faster flowing outlet glaciers than Larsen C Ice Shelf (e.g. *Schannwell et al.*, 2015). Satellite observations show a significant thinning of 10.9±1.1 m per decade since 1994 (*Paolo et al.*, 2015) along with an increase in flow speed of the grounded ice upstream (*Holt et al.*, 2013). The observed thinning accompanied by a loss of buttressing is believed to have caused a significant speed-up and drawdown of the major outlet glaciers, contributing 0.15±0.02 mm a^{-1} to global SLR (*Wouters et al.*, 2015).

Despite the growing evidence that ice dynamic SLR from APIS may be significant in the next centuries, SLR projections using numerical ice-sheet models are scarce (*Barrand et al.*, 2013b; *Schannwell et al.*, 2015, 2016). Hitherto, projections from the peninsula are provided by ice-sheet models solving the simplest force balance approximation, the SIA. While computationally efficient and valid for an ice mass

where the thickness scale is much smaller than the length scale (e.g. *Pattyn et al.*, 2013), the SIA is not valid in some key areas of the ice sheet, such as ice divides, ice streams/ice shelves, and grounding lines (*Hutter*, 1983; *Baral et al.*, 2001). To successfully simulate the coupled ice sheet-ice shelf system, membrane stress transfer across the grounding line needs to be accounted for in numerical ice-sheet models (e.g. *Pattyn et al.*, 2012, 2013). Recent advances have led to the emergence of such models incorporating the necessary physics to simulate the coupled sheet-shelf system on a continental scale (e.g. *Winkelmann et al.*, 2011; *Pollard and DeConto*, 2012a; *Cornford et al.*, 2013; *Pattyn*, 2017).

In this chapter, we use two state-of-the-art ice sheet-ice shelf models (PSU3D (*Pollard and DeConto*, 2012a) and BISICLES (*Cornford et al.*, 2013)) to compute SLR projections for the Larsen C and George VI embayments. These projections are compared to those simulated with a simple SIA ice-sheet model (BAS-APISM), where grounding-line retreat is parameterised based on a statistical model (see section 3.2.3). We evaluate the importance of each of these ice shelves with regard to their ice dynamic SLR potential to 2300 by removing them completely in our model intercomparison experiment. The sheet-shelf models are run at different horizontal resolutions to investigate the grid size dependence of the respective SLR projections. In addition to the model intercomparison experiment, the sheet-shelf models are also driven in a second experiment with a more realistic forcing of ice-shelf retreat or collapse. Subsequent tidewater glacier retreat is simulated using a simple calving criterion (*Benn et al.*, 2007a, see section 4.2.1).

4.2 Methods

The ice-sheet models BAS-APISM (*Barrand et al.*, 2013b), BISICLES (*Cornford et al.*, 2013), and PSU3D (*Pollard and DeConto*, 2012a) have been described in detail elsewhere. Here, we briefly list a few key points of each of these models

relevant to this chapter and note any important model set-up changes to their previous configurations.

4.2.1 Model description

BAS-APISM simulates ice flow by solving a linearised SIA equation. Owing to the linearisation, ice thickness appears only once as a divisor in the perturbation equation (equation (16) in *Barrand et al.*, 2013b), making BAS-APISM less sensitive to ice thickness errors than traditional SIA-based-models. The linear nature of the ice sheet equation permits superposable solutions. This means that SLR contributions from individual drainage basins can simply be summed to provide an ice-sheet-wide contribution. As the SIA prohibits the explicit modelling of the grounding line, grounding-line retreat has previously been parameterised through scenario-based and statistical model approaches. This model scales the expected retreat of the grounding line in response to ice-shelf collapse to the amount of buttressing at the ice front of each drainage basin (*Schannwell et al.*, 2016).

BISICLES models ice flow by solving a vertically integrated stress balance to determine the horizontal velocity (*Schoof and Hindmarsh*, 2010). This type of stress balance is very similar to the SSA, but includes vertical shearing in the effective viscosity calculation, resulting in softer ice at the grounding line in comparison to traditional SSA models and resembles more the behaviour of FS models (e.g. *Pattyn and Durand*, 2013). The equations are solved on an adaptive 2-D grid, allowing for higher resolution in areas of interest e.g. grounding lines and shear margins, and coarser resolution away from these regions to save computation time. We employ a subgrid interpolation scheme for basal drag near the grounding line to improve the accuracy of the grounding-line position at each time step. This scheme subdivides a partly grounded and partly floating cell into 64 equal parts and counts the grounded subdivisions to provide a more accurate calculation of basal drag in

this cell (*Cornford et al.*, 2016).

PSU3D simulates ice flow by using a hybrid combination of the scaled SIA and SSA equations. The model employs an internal flux boundary condition at the grounding line (*Schoof*, 2007). This boundary condition makes the model less sensitive to grid resolution at the grounding line, avoiding the need to resolve the boundary layer at very fine resolution (<1 km). While the model set-up is similar to *Pollard et al.* (2015), cliff failure and bedrock deformation are not included.

Basal traction in PSU3D and BISICLES is determined by a viscous law

$$\tau^b = \begin{cases} -C|\vec{u}|^{m-1}\vec{u} & \text{if } \frac{\rho_i}{\rho_w}h > -b, \\ 0 & \text{otherwise,} \end{cases} \tag{4.1}$$

where m=0.5, τ^b is the basal traction, $\vec{u}$ is the horizontal velocity, ρ_i and ρ_w are ice and ocean density, b is the bedrock elevation, and C is the basal friction parameter inferred by solving an inverse problem (see section 4.2.3).

In simulations where the calving front is not fixed e.g. where ice-shelf retreat is explicitly simulated, calving is parameterised by calculating the depths of surface (d_s) and basal crevasses (d_b) as follows (*Benn et al.*, 2007b; *Nick et al.*, 2010)

$$d_s = \frac{2}{\rho_i g}\left(\frac{\dot{\epsilon}}{\bar{A}}\right)^{\frac{1}{n}} + \frac{\rho_w}{\rho_i}d_w, \tag{4.2}$$

$$d_b = \left(\frac{\rho_i}{\rho_0 - \rho_i}\right)\frac{2}{\rho_i g}\left(\frac{\dot{\epsilon}}{\bar{A}}\right)^{\frac{1}{n}}, \tag{4.3}$$

where g is the gravitational acceleration, $\bar{A}$ is the depth averaged rheological exponent, n=3 is the rheological exponent, d_w is the water height in the surface crevasse and ρ_0 is the density of surface liquid. The parameter $\dot{\epsilon}$ is the longitudinal strain rate approximated in PSU3D through the isotropic ice divergence

$$\dot{\epsilon} = \left(\frac{\partial u}{\partial x} + \frac{\partial v}{\partial y}\right). \tag{4.4}$$

Instead of ice flux divergence, BISICLES uses stresses to approximate the tensile force such that equations 4.2-4.3 become (*Sun et al.*, 2017)

$$d_s = \frac{\mathrm{tr}(\tau)}{\rho_i g} h + \frac{\rho_w}{\rho_i} d_w, \tag{4.5}$$

$$d_b = \frac{\rho_i}{\rho_0 - \rho_i} \left(\frac{tr(\tau)}{\rho_i g} h - h_{ab} \right), \tag{4.6}$$

where τ is the deviatoric stress tensor and h_{ab} is the thickness above flotation. In PSU3D ice is calved off when the combined thickness of the surface and bottom crevasses propagate at least 75% of the column ice thickness, whereas in BISICLES icebergs calve when the sum of the surface and bottom crevasses reaches sea level.

4.2.2 Experimental design

Two experiments including all outlet glaciers of the Larsen C and George VI model domains were performed. Both experiments simulate the ice dynamic SLR only. This means that any mass loss from a negative SMB is ignored in all our simulations. The first experiment aims to compare the ice-sheet models of different complexity. In this experiment, immediate ice-shelf collapse is imposed. Following ice-shelf removal the calving front is fixed and ice sheet adjustment to the new boundary conditions is simulated to 2300. For PSU3D and BISICLES, simulations are performed at 4 km, 2 km, 1 km, and 0.5 km (BISICLES only) horizontal resolution to investigate the grid size dependence on SLR projections for each of these models. A grid resolution of 1 km in PSU3D translates to this resolution everywhere in the model domain, whereas in BISICLES this translates to a 1 km resolution in the regions of interest e.g. grounding lines, and coarser grid resolution elsewhere (max 4 km). The difference between using a 1 km static grid to the 1 km adaptive grid in BISCICLES has been shown to be minimal (*Cornford et al.*,

2013). BAS-APISM is only run at a horizontal resolution of 0.9 km.

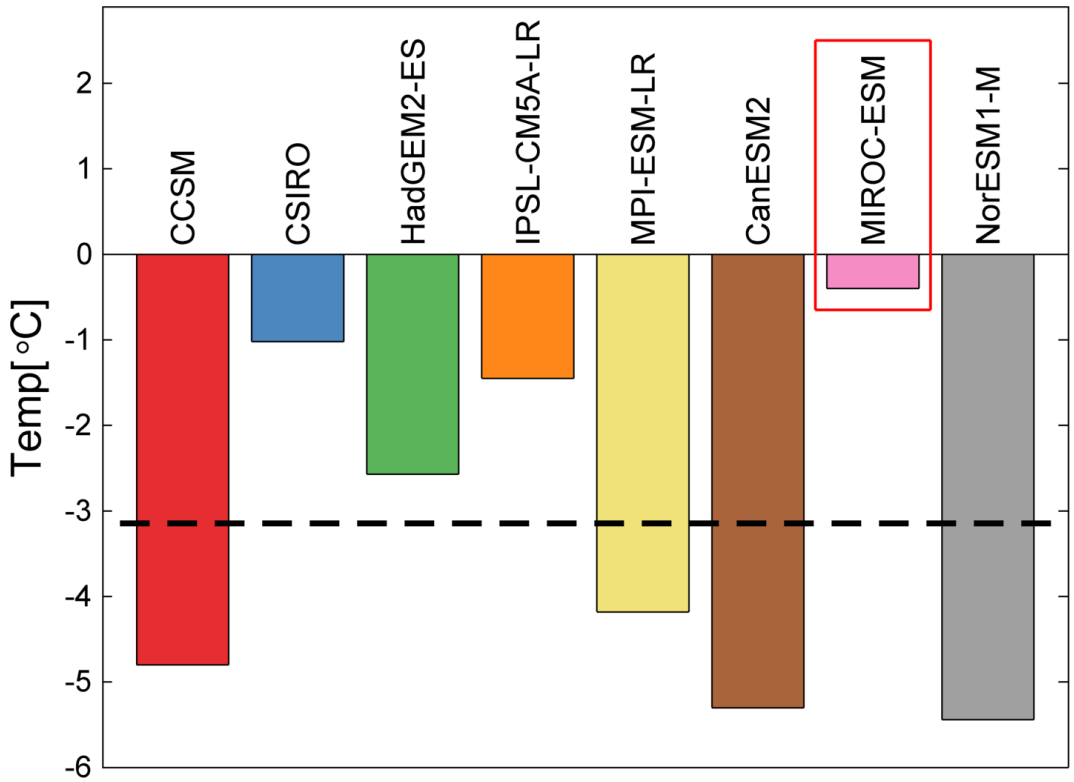

Figure 4.2: Near-surface temperature bias for the baseline period 1980-2005 in GCMs for RCP4.5 projections. Dashed black line indicates multi-model mean (-3.1±2.0°C). The selected forcing is highlighted by the red box.

In the second experiment, both sheet-shelf models are forced with Benn's calving criterion (*Benn et al.*, 2007b) at the calving front (equations 4.2-4.6) to simulate ice-shelf retreat or collapse and tidewater glacier retreat. Water height (d_w in equation 4.2) is computed from biased-corrected CMIP5 model projections to 2300 from the same model selection as presented in *Schannwell et al.* (2015). The bias-correction and melt computation approach follows *Trusel et al.* (2015) exactly. In brief, December-January-February (DJF) near-surface temperatures from the CMIP5 Historical simulations were compared to high resolution (5.5 km)

RACMO2.3 simulations (*van Wessem et al.*, 2016) such that

$$\overline{Bias_{GCM}} = \overline{T_{2m_{GCM}}} - \overline{T_{2m_{RACMO2.3}}}, \tag{4.7}$$

where $\overline{T_{2m_{GCM}}}$ and $\overline{T_{2m_{RACMO2.3}}}$ are the mean DJF near-surface temperatures over the baseline period 1980-2005 from each GCM and RACMO2.3, respectively. As we are interested in the Larsen C and George VI embayments only, the bias calculation (equation 4.7) is restricted to the ice-shelf areas in these two model domains. The best performing GCM (lowest bias) for the RCP4.5 (Figure 4.2, MIROC-ESM) and RCP8.5 (Figure 4.3, CSIRO) scenario was then selected as future forcing.

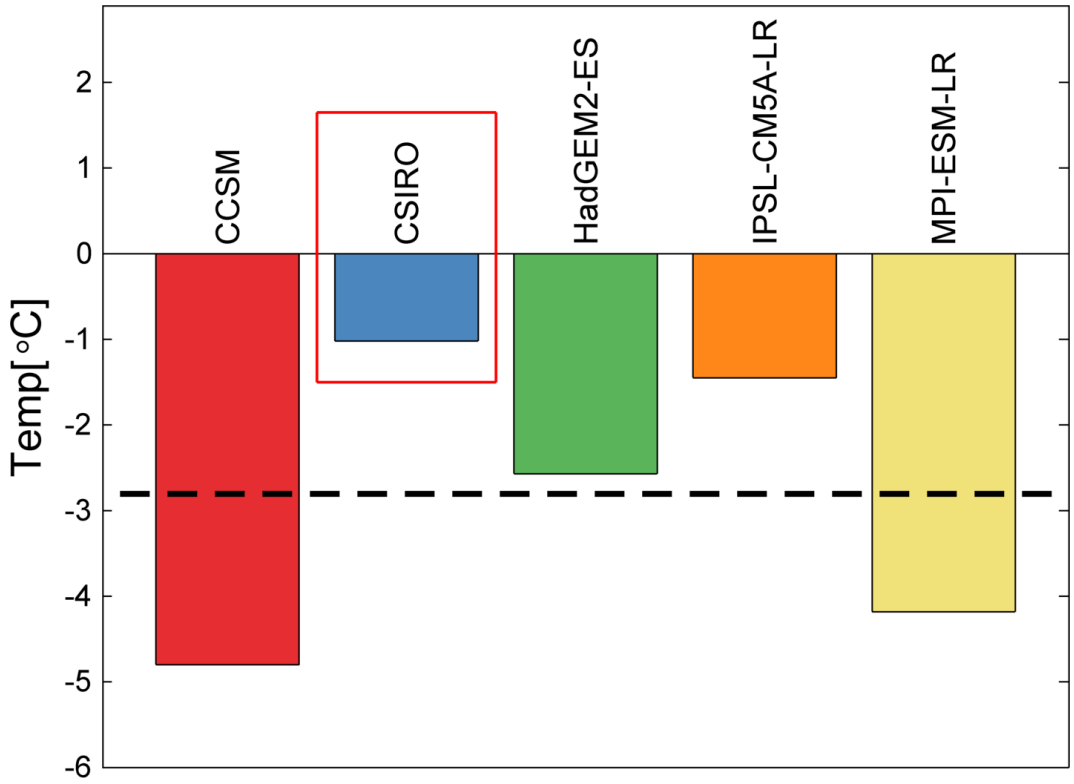

Figure 4.3: Near-surface temperature bias for the baseline period 1980-2005 in GCMs for the RCP8.5 projections. Dashed black line indicates multi-model mean (-2.8±1.7°C). The selected forcing is highlighted by the red box.

To convert from near-surface temperature to melt, the empirical formula derived by *Trusel et al.* (2015) was used. This approximates the surface melt available to fill surface crevasses (R). To compute water height in surface crevasses, d_w is simply set to (*Pollard et al.*, 2015)

$$d_w = 100R^2. \tag{4.8}$$

This results in two simulations to 2300 for PSU3D and BISICLES - one for the RCP4.5 and one for the RCP8.5 scenario. All simulations are carried out at 1 km horizontal resolution.

4.2.3 Initialisation and spin up

BAS-APISM is initialised using a combination of altimetric and velocity initialisation, permitting a steady state starting condition after initialisation under the assumption that the current ice sheet configuration is close to steady state (*Barrand et al.*, 2013b). As BAS-APISM is based on a linearised form of the SIA, it is not necessary to specify whether or not basal sliding is occurring. This means that there is no need to infer basal traction coefficients (*Barrand et al.*, 2013b). BISICLES is initialised by solving an optimisation problem to infer the basal traction coefficient C and the stiffening factor ϕ (also enhancement factor), by matching modelled velocities with observed velocities (*Rignot et al.*, 2011b). For this, a nonlinear conjugate gradient method was employed to seek a minimum of the objective function

$$J = J_m + J_p \tag{4.9}$$

where J_m is the misfit between observed and modelled velocities and J_p is a Tikhonov penalty function described by

$$J_p = \lambda_C J_C^{reg} + \lambda_\phi J_\phi^{reg} \tag{4.10}$$

where λ_C and λ_ϕ are the Tikhonov parameters and J_C^{reg} and J_ϕ^{reg} represent the spatial gradients of C and ϕ integrated over the domain (*Cornford et al.*, 2015). An L-curve analysis was performed to calibrate the Tikhonov parameters and avoid overfitting or overregularisation (*Fürst et al.*, 2015). The selected values are $\lambda_C = 10^{-1}$ and $\lambda_\phi = 10^9$ (Figure 4.4).

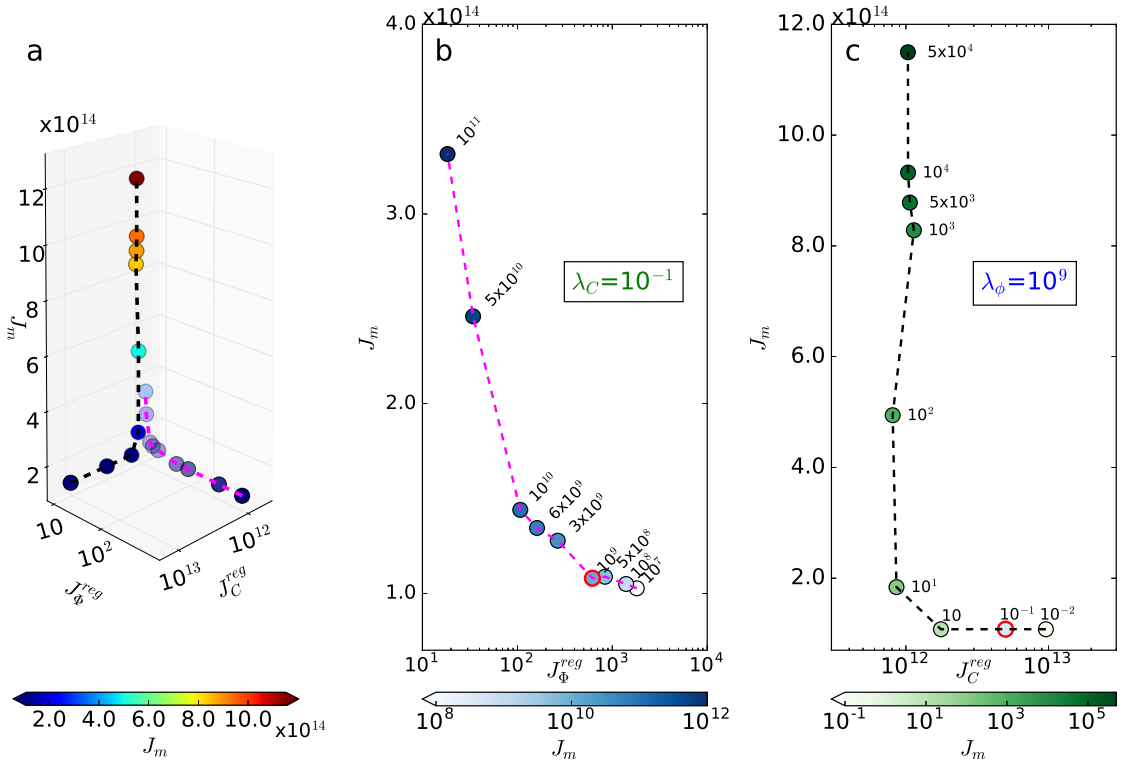

Figure 4.4: L-curve analysis to select Tikhonov parameters λ_ϕ and λ_C: (a) 3-D scatter plot of the model-data misfit J_m as a function of the regularisation terms J_C^{reg} and J_ϕ^{reg}. (b) 2-D cross section for variable λ_ϕ and λ_C fixed at 10^{-1} Pa^{-2} m^6 a^{-4}. (c) Reverse case with constant λ_ϕ at 10^9 m^4 a^{-2} and λ_C varying. The units of J_m and J_C^{reg} are m^4 a^{-2} and Pa^2 m^{-2} a^2, respectively. J_ϕ^{reg} is unitless. Selected values are highlighted by red circles in (b) and (c).

For the inversion a static horizontal resolution of 1 km was employed and a linear sliding law was used ($m = 1$ in equation 4.1). This type of inversion is well established and widely used in ice-sheet modelling (e.g. *MacAyeal*, 1992; *Morlighem et al.*, 2014a; *Cornford et al.*, 2015). To solve the inverse problem, maps of surface elevation and bedrock topography were taken from the BEDMAP2 (*Fretwell et al.*, 2013) dataset, and a steady state 3-D temperature field was used from a higher order model (*Pattyn*, 2010). In all BISICLES simulations ice temperature is held constant. PSU3D utilises a different algorithm to infer the basal traction coefficient. Instead of matching velocities, the algorithm implemented in PSU3D seeks to minimise the misfit between local surface elevation observations and modelled local surface elevations (*Pollard and DeConto*, 2012b). To achieve this, the ice-sheet model is run forward in time, and basal traction coefficients are periodically compared and adjusted according to the local surface elevation error. This iterative process is continued until modelled surface elevation converges to the best fit with observed surface elevation (*Pollard and DeConto*, 2012b). It is noteworthy that this simpler algorithm does not infer a stiffening factor ϕ for ice shelves. Input maps needed for the inversion algorithm are from ALBMAP (*Le Brocq et al.*, 2010): e.g., ice thickness, bedrock topography, and surface mass balance. Unlike in BISICLES, PSU3D solves the 3-D temperature equation, but surface air temperature forcing is held constant at year 2000 (*Le Brocq et al.*, 2010) throughout the simulations. ALBMAP instead of the more recent BEDMAP2 dataset is used because all initial and boundary conditions are present in ALBMAP. A feature that is absent in BEDMAP2. Differences between the data products may cause differences across the models in the inferred basal traction fields. However, given that *in situ* data for the AP was still sparse when BEDMAP2 was published, these differences should not be a major concern. Especially, when it is taken into account that PSU3D and BISICLES use a different algorithm to infer basal traction that most likely introduces more severe differences than the slightly different boundary condition

datasets. For all PSU3D simulations, basal traction fields are interpolated onto the respective model grid from a 5 km Antarctica inversion simulation. The basal traction, C, and stiffening, ϕ, fields are held constant throughout our simulations, even though these fields should be time varying. However, numerical ice-sheet models of the current generation lack the necessary skill at present to incorporate this (*Cornford et al.*, 2015).

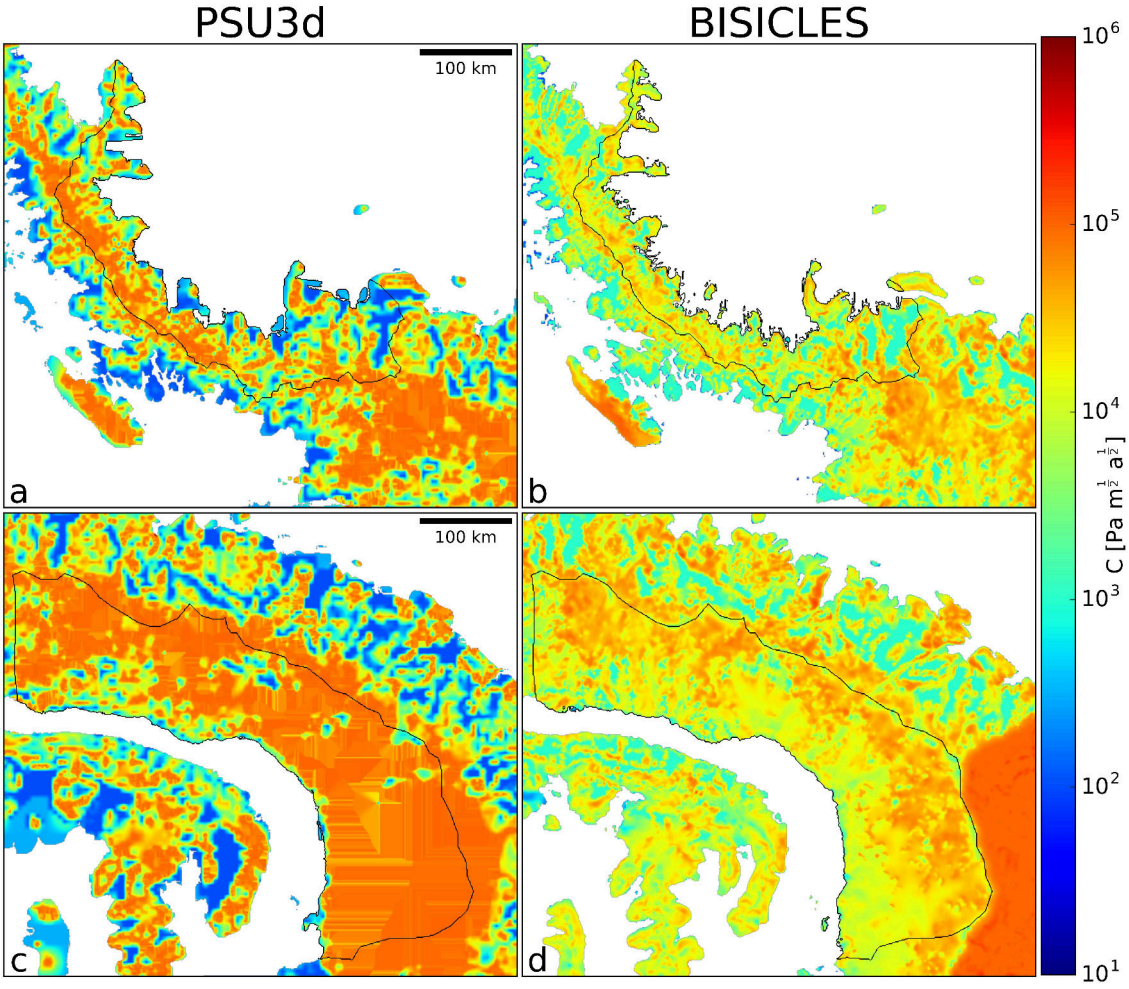

Figure 4.5: Inferred basal traction fields C for the Larsen C (a,b) and George VI model domains (c,d). The black polygons show the respective drainage basin. Location of maps is approximated by grey boxes in Figure 4.1.

Under the assumption that the ice-sheet is close to equilibrium, both inversion methods - velocity and surface elevation matching - should result in similar basal traction coefficient patterns. Figure 4.5 compares the basal traction fields for Larsen C and George VI model domains. Overall, both inversions show a similar qualitative pattern with lower basal drag towards the grounding line. For Larsen C Ice Shelf (Figure 4.5a,b), the agreement is better than for George VI. However, in areas of slippery bedrock conditions (blue color), basal drag is constantly lower in PSU3D than for BISICLES. The opposite is the case for sticky bedrock conditions (orange to red color). Here PSU3D inverts for basal drag that is at least an order of magnitude higher than for the corresponding regions in BISICLES. Most notably are these differences for the George VI model domain (Figure 4.5c,d). In general, basal drag is higher than for Larsen C and there is less spatial variability in basal drag. PSU3D infers high basal drag throughout the model domain corresponding to very sticky bedrock conditions. The high basal drag in BISICLES just outside of the model domain is not a result of the basal drag inversion (Figure 4.5d), but was set to a very high value to represent a no-flux condition at the domain boundaries. This is not the case in PSU3D where a nested domain is used, forced at the lateral boundaries with a continental 20 km Antarctica model simulation.

In theory, PSU3D and BISICLES should be close to equilibrium after initialisation, providing $\frac{\partial h}{\partial t} = 0$. However, this condition is often not fulfilled (*Cornford et al.*, 2015; *Nias et al.*, 2016), requiring a spin-up or relaxation simulation to reach a steady state for each model to guarantee a stable starting position. To facilitate comparison across all three ice-sheet models, the employed spin-up approach aims to keep the ice sheet geometry as close as possible to the initial geometry. This is necessary because BAS-APISM provides a stable starting condition after initialisation. To ensure a minimal change in ice-sheet geometry, we compute a synthetic mass balance (MB) which is simply (*Price et al.*, 2017)

$$MB = FC, \tag{4.11}$$

where FC is the negative of the modelled thickness field change when the model is run forward a single time step. All simulations are then run forward in time for 50 years with only this forcing applied. To reach steady state, the volume above flotation change with time should be near zero ($\frac{\partial V}{\partial t} \sim 0$) at the end of the spin-up. All of our simulations fulfil this criterion (Figure 4.6), even though PSU3D simulations are not as close to steady state as BISICLES simulations at the end of the spin-up period. It is likely that a longer spin-up of PSU3D would lead to an initial starting position closer to steady state. However, considering the computation cost of longer spin-up simulations and the expected marginal gain, the 50 year spin-up simulation was deemed sufficient. This is in line with other ice-sheet modelling studies (*Cornford et al.*, 2015).

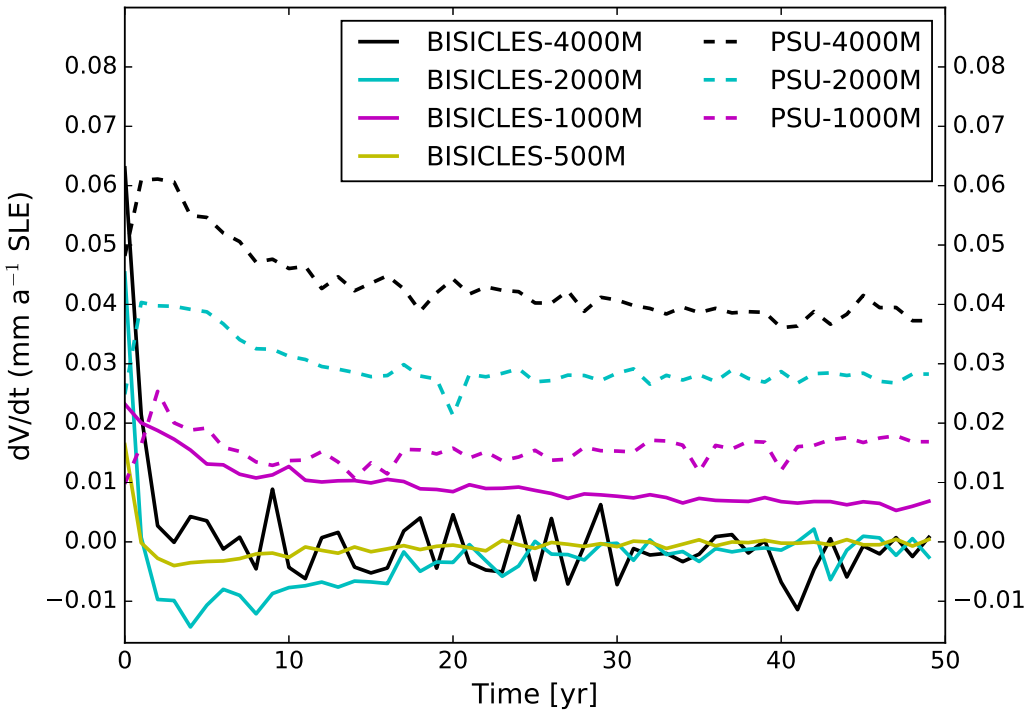

Figure 4.6: $\frac{\partial V}{\partial t}$ spin-up plot for BISICLES (solid lines) and PSU3D (dashed lines) at different horizontal resolutions.

4.3 Results and discussion

4.3.1 Experiment 1: Immediate ice-shelf collapse

Even in the event of immediate ice-shelf collapse all ice-sheet models project very little SLR from the Larsen C embayment, ranging from 0.6-1.6 mm after 300 years (Figure 4.7a). BAS-APISM shows the lowest SLR projection at 0.5 mm, while the sheet-shelf models project slightly higher SLR, but show excellent agreement in projected SLR. In response to Larsen C collapse, SLR contributions rise considerably, but only for ∼25 years before the system adjusts to the new boundary conditions for another 25 years until reaching steady state.

From 2050 onwards there is almost no notable contribution to SLR remaining as a result of the collapse event (Figure 4.7c). The situation is different for the George VI embayment. SLR projections are higher, ranging from 1.5-11 mm across the ice-sheet models and different model resolutions (Figure 4.7b). For this model domain, BAS-APISM projects higher SLR but agrees with the sheet-shelf models within its uncertainty. While there is a notable grid dependence in BISICLES (1.5-5.6 mm), this is not the case for PSU3D where model simulations at all horizontal resolutions result in very similar SLR projections (8.1-8.8 mm). BISICLES projections are generally lower than PSU3D projections at the same horizontal resolution. The initial response of the grounded ice sheet to ice-shelf removal across all models is more dramatic - an order of magnitude higher than for Larsen C glaciers (Figure 4.7c,d). However, the overall response reveals a similar pattern as for Larsen C glaciers, with a strong initial response to ice-shelf collapse, followed by a rapid decay in SLR contributions before a new steady state is reached at ∼2100. PSU3D continues to contribute more to SLR beyond 2100 and is further away from steady state at the end of the simulation period (Figure 4.7d). We attribute this to the fact that the model is not as close to steady state as BISICLES

after initialisation. The combined SLR projections range from 2.7-11.5 mm across all simulations, with the bulk of the SLR projections coming from George VI outlet glaciers (>60%).

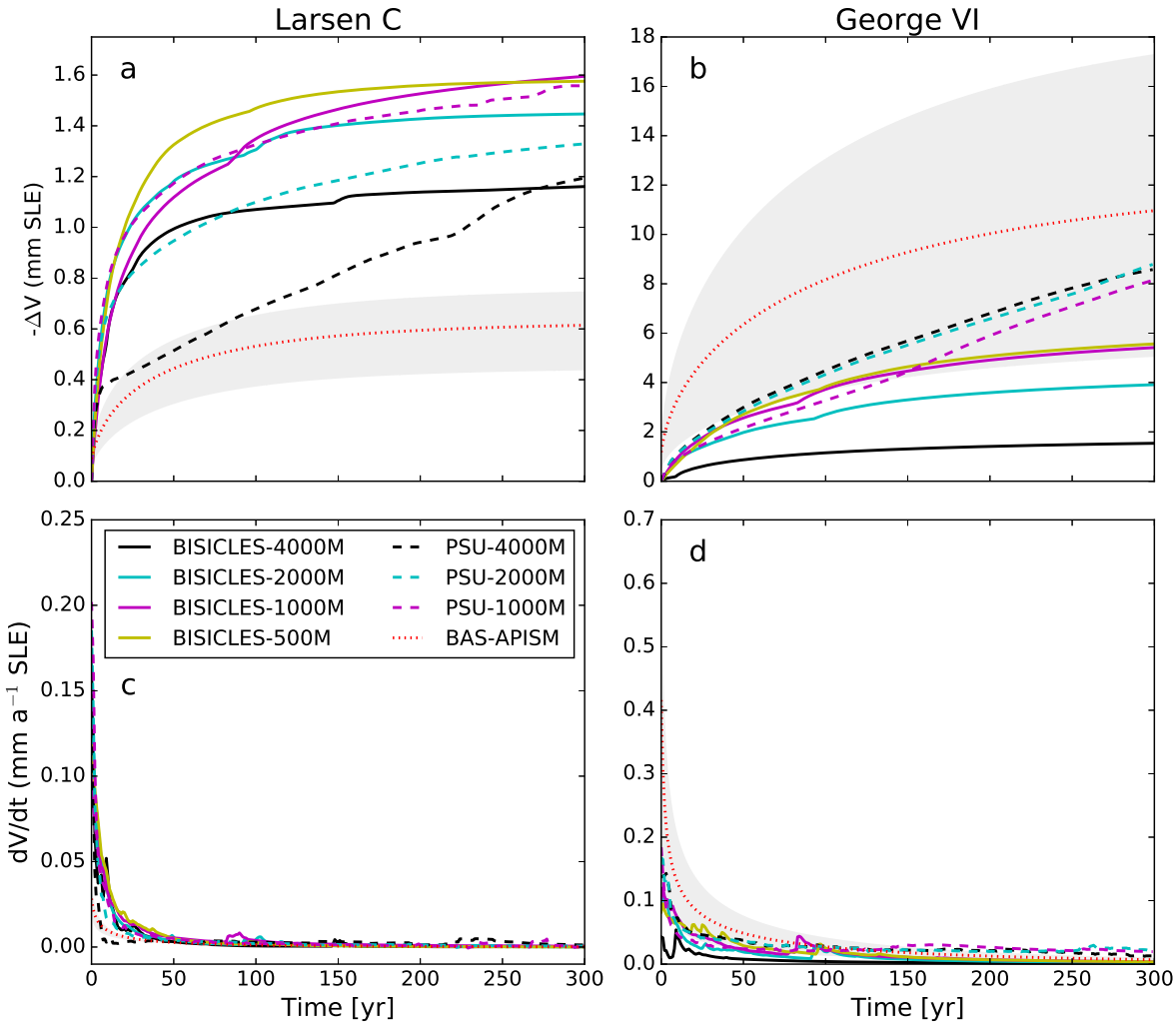

Figure 4.7: Upper panel (a,b) shows SLR projections for BISICLES (solid lines), PSU3D (dashed lines), and BAS-APISM (dotted line). Lower panel (c,d) shows the derivative (rate of change) of the corresponding SLR projections in the upper panel (a,b). Grey shading displays uncertainty associated with SLR projections from BAS-APISM. Note different y-axis scales.

Simulations for the sheet-shelf models were carried out at different horizontal resolutions to investigate the grid dependence of the SLR projections and to select the best model resolution for the more realistic forcing experiment. This selection was based on the best compromise between computational demand and appropriate grid resolution. For BISICLES, the appropriate grid resolution was evaluated following *Cornford et al.* (2016) by ensuring the following conditions are met: i) the difference in SLR projections decreases as the grid resolution increases (e.g. 2 km to 1 km) at first order. This means that the difference between BISICLES simulations at 1 km and 0.5 km should be half of the difference between 2 km and 1 km. ii) Moreover, the difference between the SLR projections should be sufficiently small. Both conditions are met for simulations at 1 km and 0.5 km resolution. As computation time increased by a factor of roughly eight from 1 km to 0.5 km, 1 km resolution was selected for the second experiment. In addition to saving considerable computation and queuing time, this resolution also facilitates comparison between BISICLES and PSU3D, since PSU3D highest stable horizontal grid resolution is 1 km. Due to the implementation of an internal flux boundary condition at the grounding line, PSU3D should not exhibit such grid dependence. This is corroborated by our simulations (Figure 4.7a,b), showing very little change in SLR projections as the grid is refined. To facilitate comparison between the two sheet-shelf models in the second experiment, however, a 1 km grid resolution was also selected for PSU3D.

Despite the simplicity in the force balance approximation, BAS-APISM provides SLR projections that are of the same order of magnitude as the sheet-shelf models. However, the spatial pattern of dynamic thinning does not match as well as the SLR projections imply, suggesting equifinality in simulation outcomes. Thinning in the south of the Larsen C embayment domain (Figure 4.8) agrees best with the sheet-shelf model projections, but the central - where most of the SLR originates from in BAS-APISM - and the northern sectors show minimal thinning in PSU3D and

BISICLES (<0.6 m a^{-1}, Figure 4.8b,c), whereas thinning is forecasted for these regions in BAS-APISM (>0.6 m a^{-1}, Figure 4.8a). Overall, the model performs better for the George VI domain where thinning is most pronounced in the central and southern part of the domain (>0.7 m a^{-1}), with a couple of thinning hotspots in the north (Riley and Chapman glaciers, Figure 4.9).

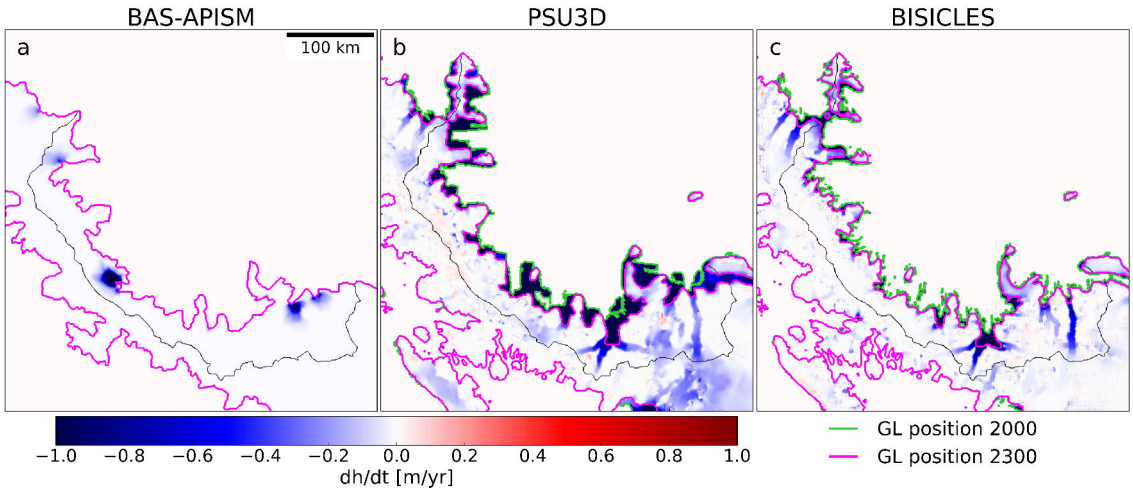

Figure 4.8: Dynamic thinning pattern averaged over the simulation period for the Larsen C embayment in (a) BAS-APISM, (b) PSU3D, and (c) BISICLES.

When comparing the modelled thinning pattern across the sheet-shelf models only, excellent agreement in the overall pattern, as well as local thinning hotspots, is found (Figure 4.8, 4.9). For Larsen C, most of the extensive thinning is restricted to the southern end of the domain, where six of the main outlet glaciers (Gibbs, Lammers, Cole, Weyerhauser, Sunfix, and Lurabee glaciers) show notable grounding-line retreat (>1 km) and dynamic thinning propagates far inland (∼75 km). Grounding-line positions at the end of the simulation for both models are almost identical. However, the initial grounding-line position (Figure 4.8b,c; purple line) differs. This discrepancy is introduced in the model spin-up phase. Since PSU3D is not as close to steady state, the grounding line slightly advances in the first years of the spin-up, resulting in slightly different

initial grounding-line locations at the start of the prognostic simulations. The more advanced grounding-line position also has consequences for SLR projections as more ice is grounded initially in the PSU3D simulations and these grounded areas contribute to SLR when they become afloat in the experiments. However the effect is small (0.28 mm). No such discrepancy in initial grounding-line position is present for the George VI embayment basins. Here, thinning and grounding-line retreat are most pronounced in the central part of the domain, where the largest outlet glaciers such as Ryder and Goodenough feed George VI Ice Shelf. Thinning propagates far inland in these regions (>80 km), but the rate at which the ice sheet thins decays rapidly within a few kilometers upstream from the grounding line. The only difference in grounding-line retreat and thinning pattern between the two models is in the north of the domain, where BISICLES unlike PSU3D projects some significant (>1 km) retreat of the grounding line (Figure 4.9).

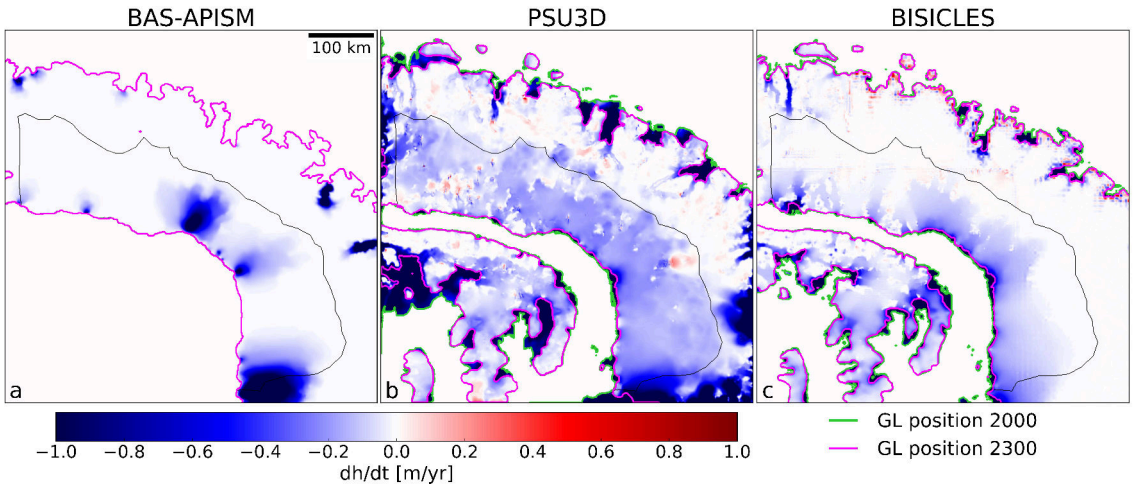

Figure 4.9: Dynamic thinning pattern averaged over the simulation period for the George VI embayment in (a) BAS-APISM, (b) PSU3D, and (c) BISICLES.

While BAS-APISM projects similar total SLR over the next 300 years to sheet-shelf models, the spatial thinning pattern (especially for the Larsen C embayment) shows a rather poor match between BAS-APISM and the sheet-shelf models. This suggests that the statistical model used to estimate the imposed grounding-line retreat in BAS-APISM does not perform satisfactorily in some areas. To confirm this observation, seven sample drainage (Figure 1.3) basins were selected to compare the grounding-line retreat rates simulated by the statistical parameterisation with the grounding-line retreat rates simulated by the sheet-shelf models. The selected basins were amongst the areas with the highest modelled thinning rates in the sheet-shelf simulations (Figures 4.8 and 4.9). For these sample basins, PSU3D simulates the highest retreat rates, while BAS-APISM's statistical grounding-line retreat parametersiation simulates the fewest grounding-line retreat. The difference between the sheet-shelf models in mean grounding-line retreat is mostly due to the advance of the grounding line in PSU3D in the spin-up phase in the Larsen C embayment. This leads to significantly higher grounding-line retreat rates in this area compared to BISICLES (Table 4.1). Comparing the mean grounding-line retreat rates seems to indicate that BAS-APISM predicts similar retreat rates to the sheet-shelf models. However, when grounding-line retreat rates are compared on a basin to basin scale, it becomes clear that the statistical parameterisation is in most cases unable to reproduce the grounding-line retreat rates simulated by the other models (Table 4.1). This again points towards equifinality in the simulation outcomes, where BAS-APISM predicts similar retreat rates and hence SLR projections when averaged over the entire model domain, but fails to reproduce the simulated grounding-line retreat on a finer spatial scale. This result also indicates that the differences in the ice dynamic thinning pattern between BAS-APISM and the sheet-shelf models are more likely to be a result of the shortcomings in the statistical grounding-line retreat parameterisation than differences in ice flow approximations. A reason for this discrepancy in simulated grounding-line retreat

could be the approach of how buttressing is calculated in the statistical model. It is assumed that ice flux is approximately normal to the grounding line. This type of buttressing - sometimes referred to as flow buttressing (*Fürst et al.*, 2016) - only takes into account buttressing in one direction - in this case the direction of flow. However, buttressing in confined outlet glaciers may be provided through lateral friction or confluent flow (e.g. *Fürst et al.*, 2016). A better measure to account for these processes would be to compute maximum buttressing which provides the maximum buttressing in any direction (*Fürst et al.*, 2016). Another simplification in the statistical grounding-line retreat parameterisation is that bedrock topography is omitted, potentially resulting in large grounding-line retreat rates for highly buttressed drainage basins that are located on prograde sloping bedrock and little grounding-line retreat for lightly buttressed drainage basins located on retrograde sloping bedrock. Moreover, the input data used to calculate buttressing in the statistical model are from a model inversion on a 5 km horizontal grid (*Arthern et al.*, 2015). While this resolution is sufficient for the largest outlet glaciers in the AP region, smaller outlet glaciers may not be well resolved at this horizontal resolution.

Ice shelf	Glacier name	BAS-APISM	PSU3D	BISICLES
Larsen C	GLCW	0.0 km	35.0 km	21.6 km
Larsen C	Sunfix	6.4±2.2 km	28.0 km	3.3 km
Larsen C	Lurabee	1.0±0.5 km	7.4 km	7.3 km
George VI	Riley North	0.0 km	6.4 km	18.3 km
George VI	Chapman	2.5±0.9 km	4.5 km	4.5 km
George VI	Ryder	0.3±0.2 km	8.7 km	7.2 km
George VI	Goodenough	21.0±8.0 km	7.2 km	4.7 km
Mean		4.5±1.7 km	13.9 km	9.6 km

Table 4.1: Comparison of simulated grounding-line retreat at seven sample glaciers. Locations of glaciers are shown in Figure 1.3. GLCW = Gibbs-Lammers-Cole-Weyerhause glacier complex.

Ice-shelf removal does not result in widespread grounding line retreat in either model domains. This is unsurprising for the Larsen C embayment, owing to a combination of prograde sloping bedrock topography (*Fretwell et al.*, 2013, Figure 4.1b) and the fact that the buttressing force provided by Larsen C Ice Shelf is rather small (*Fürst et al.*, 2016). These characteristics do not apply to the George VI embayment. The shelf provides strong buttressing (*Fürst et al.*, 2016) and large portions of the bedrock immediately upstream from the current grounding line are marine-based. Despite these favourable conditions for MISI, grounding-line retreat is limited to a few locations and <10 km in length. This suggests that the stabilising forces (e.g. basal drag, lateral shear) provide enough resistance to keep the ice-sheet in a stable configuration after an initial adjustment to the perturbed boundary conditions.

4.3.2 Experiment 2: Calving criterion

SLR contributions span a much larger range in this experiment where the calving front is permitted to evolve freely according to Benn's calving criterion (see section 4.2.1). Whereas in some RCP4.5 ('business as usual') scenario simulations negligible SLR is projected, projections increase to as much as ∼23 mm in the RCP8.5 ('high emission') scenario (Figure 4.10a,b). Most of this contribution is from George VI embayment basins, while contributions from Larsen C embayment basins remain similar to the immediate collapse experiment (<1.5 mm, Figure 4.10a). There is a notable difference between projections from the different models (Figure 4.10b). Projections from PSU3D remain almost unchanged in comparison to the immediate collapse experiment (Figure 4.10a,b). This is in stark contrast to simulations from the BISICLES model. Here, almost no SLR is projected for the RCP4.5 scenario, but SLR projections rise to ∼23 mm for RCP8.5 (Figure 4.10a,b). George VI contributes over 90% of this total, while SLR projections from Larsen C with BISICLES are lower (<1 mm) than for the immediate collapse experiment.

For Larsen C Ice Shelf, at least 40% of the shelf has to be lost before a slight increase in SLR along with retreat of the grounding-line is simulated by BISICLES (Figure 4.10c). The behaviour is different for PSU3D where an immediate SLR contribution alongside a loss of grounded ice (area integral of grounding-line retreat) is modelled (Figure 4.10c). This is due to the more advanced initial grounding-line position and cannot be attributed to a reduction in buttressing of the ice shelf. For George VI Ice Shelf the area that needs to be removed before any grounding-line retreat is initiated varies across the models (Figure 4.10d). For BISICLES ∼30% of the ice shelf has to be removed before any signal is seen in the SLR projections, whereas this number appears to be lower (∼15%) for PSU3D (Figure 4.10d). That less of the shelf needs to be removed to trigger a contribution to SLR suggests the

shelf provides more buttressing to the grounded ice upstream than Larsen C Ice Shelf and supports earlier findings with a different ice-sheet model (*Fürst et al.*, 2016).

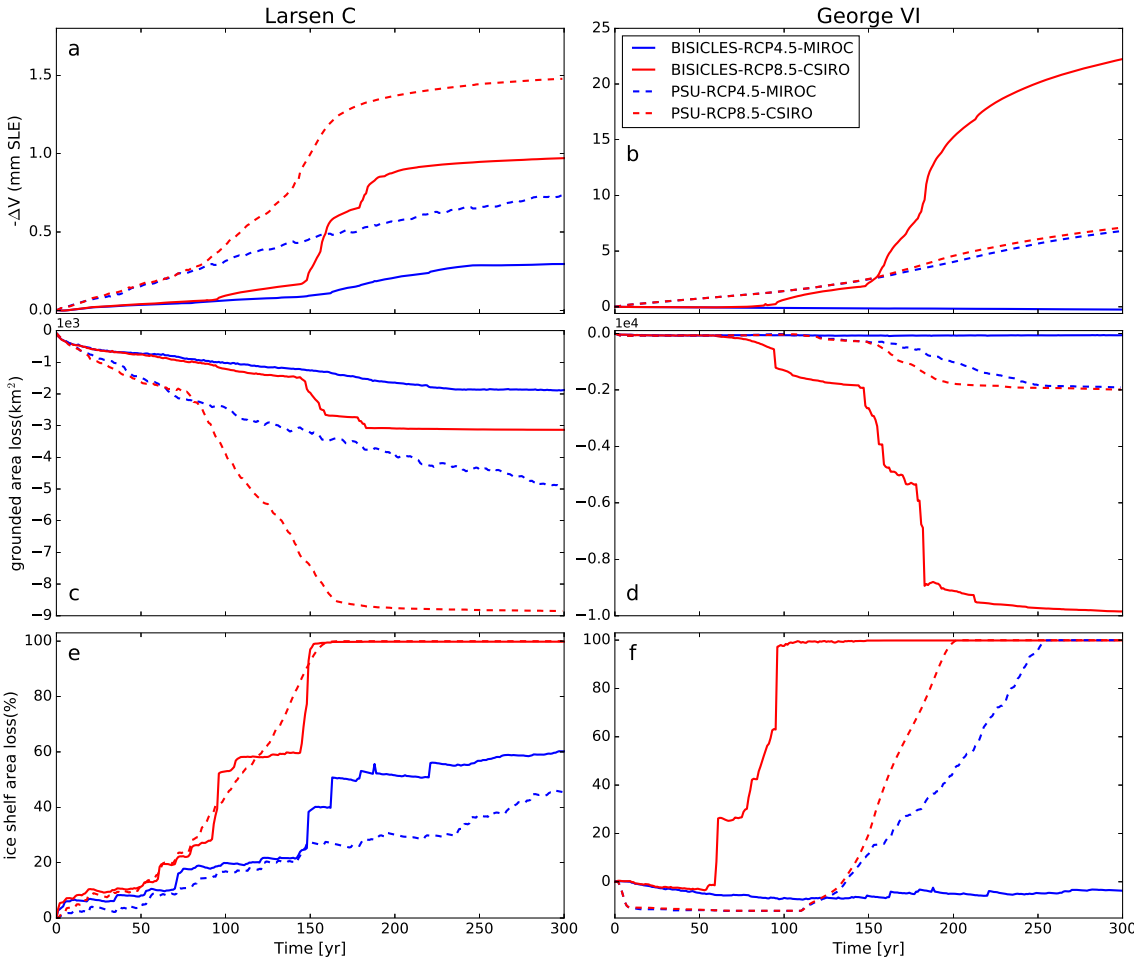

Figure 4.10: SLR projections for Larsen C (a) and George VI ice shelves (b) with corresponding area loss of grounded ice (c,d) and ice shelf area loss (e,f).

Grounding-line retreat at Larsen C basins and most simulations for George VI basins are limited to a few hotspots (e.g. Gibbs, Lammers, Cole, Weyherhauser, Sunfix, and Lurabee glaciers for Larsen C basins and Riley, Chapman, Ryder, and Goodenough glaciers for George VI basins) of grounding-line retreat in the same areas where retreat was modelled in the immediate collapse experiment

(Figure 4.11, 4.12). The larger grounding-line retreat rates for PSU3D in the Larsen C embayment are due to the more advanced initial grounding-line position. It takes ∼50 years to unground this more advanced grounded area. From this point onwards, grounding-line retreat of the Larsen C domain is very similar for both ice-sheet models (Figure 4.10c). This is not the case for George VI Ice Shelf, where the BISICLES simulations envelope the PSU3D simulations (Figure 4.10d).

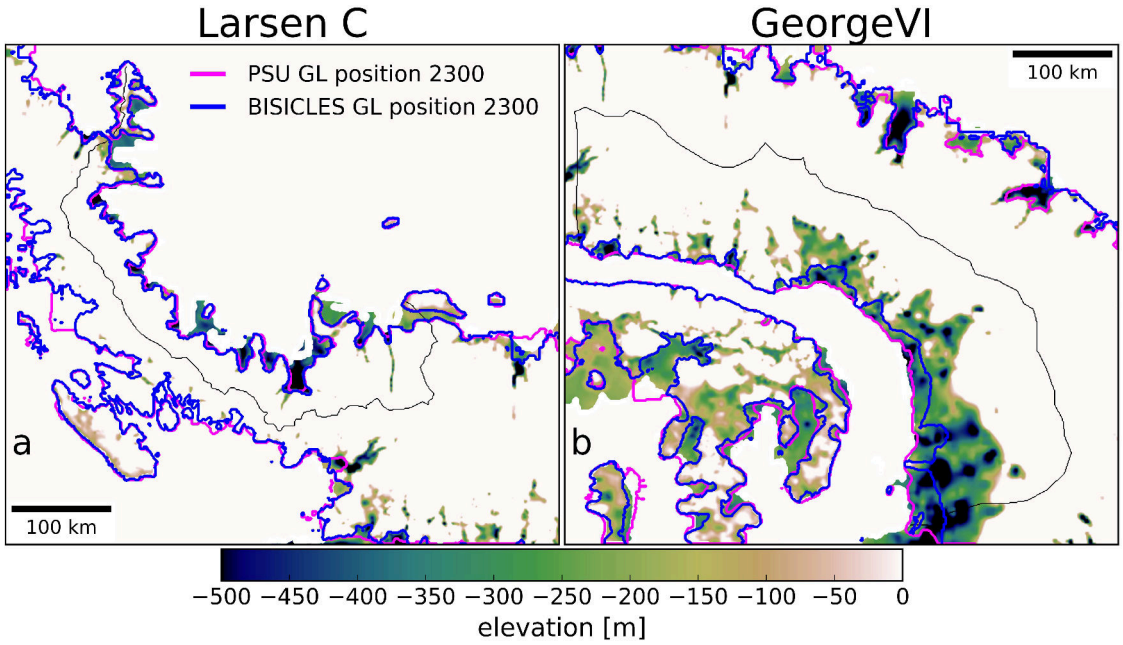

Figure 4.11: Comparison of modelled grounding-line positions for RCP8.5 scenario for Larsen C (a) and George VI embayments (b). Black outlines show drainage basins.

For PSU3D the modelled grounding-line retreat is almost identical to the immediate collapse experiment. There is no grounding-line retreat for the RCP4.5 scenario in BISICLES, but widespread grounding-line retreat for the RCP8.5 scenario (Figure 4.11b). In the RCP8.5 scenario, the shelf retreats rapidly and is removed over ∼40 years, disappearing completely around 2100. But unlike in the immediate collapse experiment, the dynamic calving front is forced further back into areas with retrograde sloping bedrock, leading to even more grounding-line retreat and widespread thinning throughout the model domain. Dynamic thinning propagates

as far upstream as ∼100 km from the grounding line (Figure 4.12b).

This large grounding-line retreat is not simulated by PSU3D. The most likely reason for this is the basal drag coefficient. The basal drag coefficient for George VI Ice Shelf in PSU3D is an order of magnitude higher than in BISICLES except for a few areas in the immediate vicinity of the grounding line. As the calving law is only applied to floating ice, this higher basal drag has the following effect. In BISICLES the removal of the ice shelf leads to a speed-up of the major outlet glaciers induced by the reduction of buttressing. This speed-up is accompanied by dynamic thinning leading to the tidewater glacier tongue to reach flotation and is thus forced further back by the calving law. Due to the high basal drag inferred by PSU3D, this process never takes place in simulations with this model. As there is too much basal resistance, the outlet glaciers do not speed up enough to cause dynamic thinning so that the glacier tongue reaches flotation. This in turn means that the calving law cannot be applied at the tidewater glacier fronts.

In order to test this hypothesis, additional simulations were carried out with PSU3D. In the first simulation, in addition to the normal forcing applied in the experiment, a constant basal melt anomaly was applied over the full length of the simulation period, equivalent to the current thinning signal of George VI Ice Shelf (*Paolo et al.*, 2015). In a second melt experiment, the same basal melt rate as the thinning signal was applied initially and then increased linearly to 3x the current thinning signal by 2100 and held constant for the remainder of the simulation until 2300. This type of ocean forcing crudely approximates the course of global near-surface temperature increase in the RCP8.5 scenario. The SLR projections from these stronger forcings are within a few tenth of millimeters of the simulations without any ocean forcing.

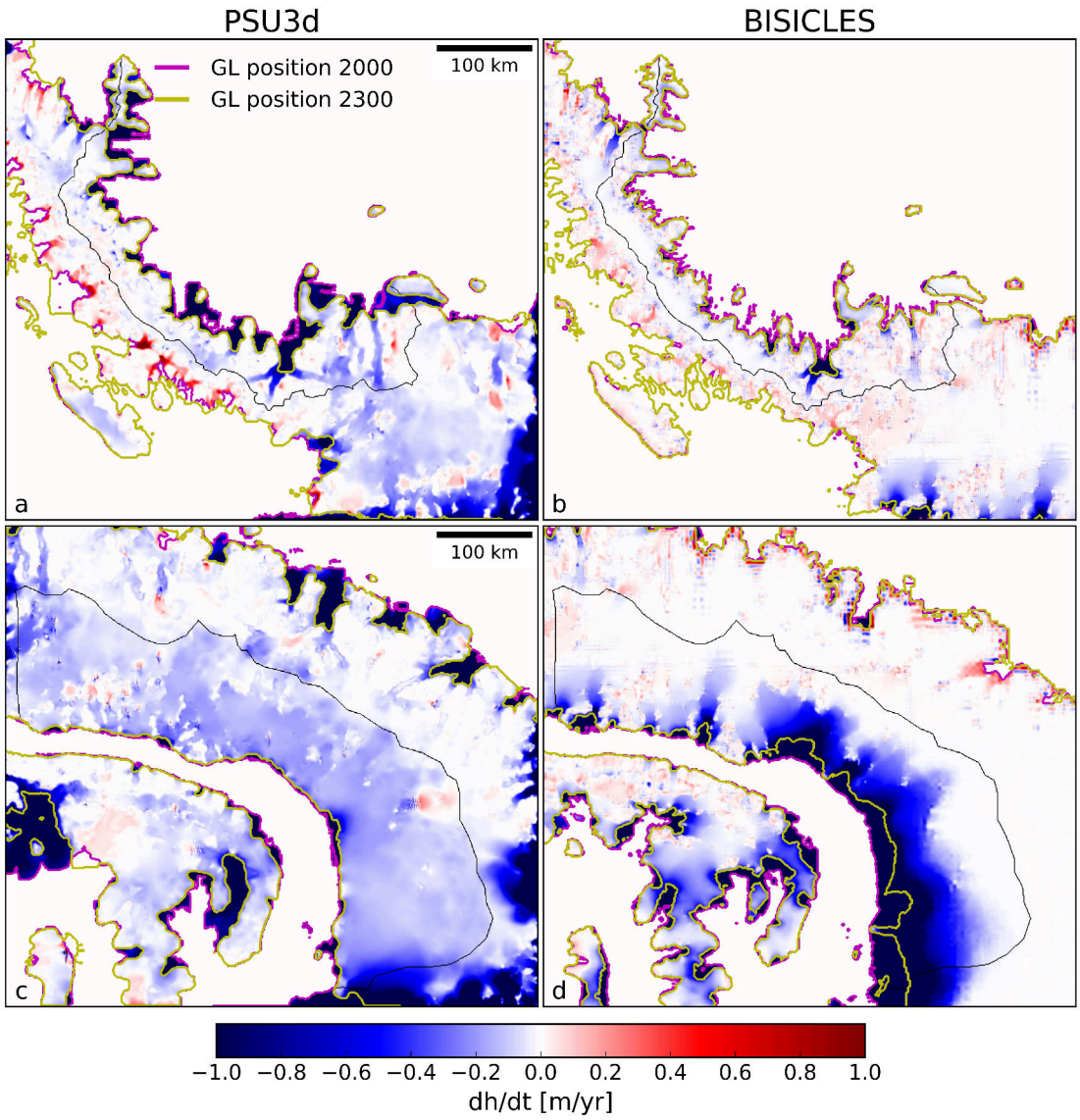

Figure 4.12: Dynamic thinning pattern averaged over the simulation period in the RCP8.5 scenario for Larsen C (a,c) and George VI embayments (b,d). Black outlines show drainage basins.

There is excellent agreement between the models for Larsen C Ice Shelf retreat timing and duration (Figure 4.10e). Despite the difference in implementation of the calving law, both models project complete ice-shelf removal by 2150 in RCP8.5 and ∼60% of area loss by 2300 in the RCP4.5 scenario (Figure 4.10e). Most of the shelf area is lost within a century in RCP8.5 (Figure 4.10e). The calving behaviour across the models is different with PSU3D exhibiting a more linear retreat pattern,

whereas BISICLES shows a step-like retreat pattern (Figure 4.10e,f). To force Larsen C Ice Shelf into a sustained retreat, a waterdepth of >1 m a^{-1} is necessary (w_d in equation 4.2). This is in line with earlier studies (*Pollard et al.*, 2015). For the George VI embayment, more meltwater is necessary in BISICLES to trigger retreat, leading to no shelf retreat in the RCP4.5 scenario, but very rapid retreat in the RCP8.5 scenario (Figure 4.10f). Here, George VI has completely disintegrated by 2100 and the shelf is removed within ∼40 years. In comparison, the meltwater threshold stays stable for PSU3D (1-3 m a^{-1}), leading to a similar ice-shelf retreat pattern as for Larsen C Ice Shelf (Figure 4.10f).

To test the robustness of our model projections, a range of sensitivity experiments were carried out. With PSU3D, simulations for Larsen C Ice Shelf were performed where in addition to the calving forcing described above, a basal melt anomaly was also applied. In the first simulation, the basal melt anomaly was set to the equivalent of the current thinning signal derived from remote sensing methods (*Paolo et al.*, 2015) for the entire simulation period. In the second simulation, the same basal melt anomaly was applied initially, but this melt rate was then increased linearly to 3x the current thinning signal by 2100 and remained at this magnitude for the rest of the simulation. Both simulations show SLR projections of ∼1.5 mm by 2300 for the Larsen C embayment, showing that the results are relatively insensitive to increased ocean forcing.

Observations from GPS stations in the northern peninsula show that the isostatic uplift rates have increased up to 8.8 mm a^{-1} since the collapse of Larsen B Ice Shelf (*Thomas et al.*, 2011). As in all previous simulations isostatic rebound was omitted, the immediate collapse experiment was rerun with the same set-up as before but include bedrock deformation as described in *Pollard and DeConto* (2012a). This simulates bedrock deformation as a two-layer isostasy model where the viscous asthenosphere is overlaid by a rigid elastic lithosphere (*Pollard and DeConto*, 2012a). Changes in SLR projections due to the inclusion of isostatic

rebound are negligible for Larsen C (<0.7%) and remain moderate for the George VI embayment (<10%), revealing that at least on the timescales considered here, isostatic rebound does not play an important role.

As a recent study demonstrated the importance of the basal boundary condition by showing that SLR projection may vary by a factor of ∼3 depending on the applied basal sliding law (*Pattyn*, 2017), the immediate collapse experiment was repeated with a range of basal sliding laws in the BISICLES model. In addition to the sliding law described by equation 4.1 with m=0.5 (quadratic law), simulations were performed with m=1/3 (cubic law), m=1 (linear law), and with a pressure-limited law according to Tsai (*Tsai et al.*, 2015). This law combines the power law (equation 4.1) with the Coulomb friction law by ensuring that basal traction cannot exceed the Coulomb friction that is proportional to the effective pressure N_e:

$$\tau_b = \min\left(a * N_e, -C|\vec{u}|^{m-1}\vec{u}\right), \tag{4.12}$$

here the first term in the parentheses is the Coulomb friction law with a=0.5, m=0.5 and the effective pressure N_e is

$$N_e = \rho_i g(h - h_f), \tag{4.13}$$

where h is the ice thickness and h_f is the flotation thickness. Since the Coulomb law implies that basal drag approaches zero towards the grounding line, this type of basal sliding law ensures a smooth transition from grounded to floating ice, unlike the traditional power law (equation 4.1) which implies that basal drag is highest near the grounding line (e.g. *Tsai et al.*, 2015; *Pattyn*, 2017).

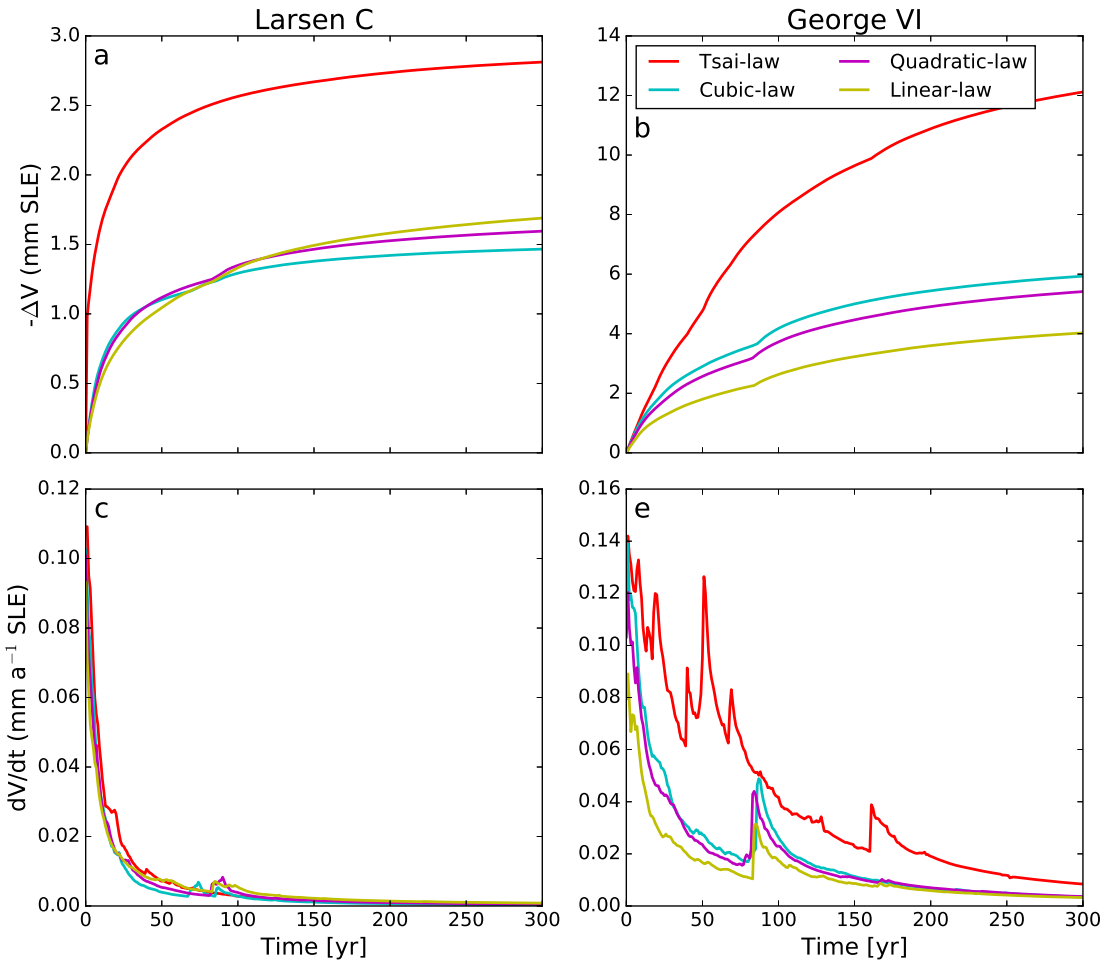

Figure 4.13: SLR projections using different basal sliding laws (a,b). Lower panel (c,d) shows the derivative (rate of change) of the corresponding SLR projections in the upper panel (a,b). Note different y-axis scales.

All power law implementations project similar SLR, with the linear law projecting the least and the cubic law projecting the most (Figure 4.13a,b). However, all three power laws project SLR within ∼2 mm of each other, ranging from 1.4-1.6 mm for Larsen C Ice Shelf (Figure 4.13a) and 4-6 mm for George VI Ice Shelf (Figure 4.13b). Simulations with the Tsai law, however, project SLR twice as high as for the cubic power law, resulting in ∼3 mm for Larsen C Ice Shelf and ∼12 mm for George VI Ice Shelf (Figure 4.13). While grounding-line positions are only slightly different for the Larsen C embayment across the different sliding relations, the Tsai law

simulation for the George VI embayment loses a much larger area of grounded ice in comparison to the power law simulations (Figure 4.14). As for the BISICLES RCP8.5 simulation of the calving experiment, largest retreat rates are simulated in areas with very deep bedrock topography (Figure 4.11b, 4.14b, English Coast drainage basins). Grounding-line retreat is halted at local bedrock highs, further reinforcing the importance of accurate bedrock topography maps for reliable SLR projections (e.g. *Sun et al.*, 2014).

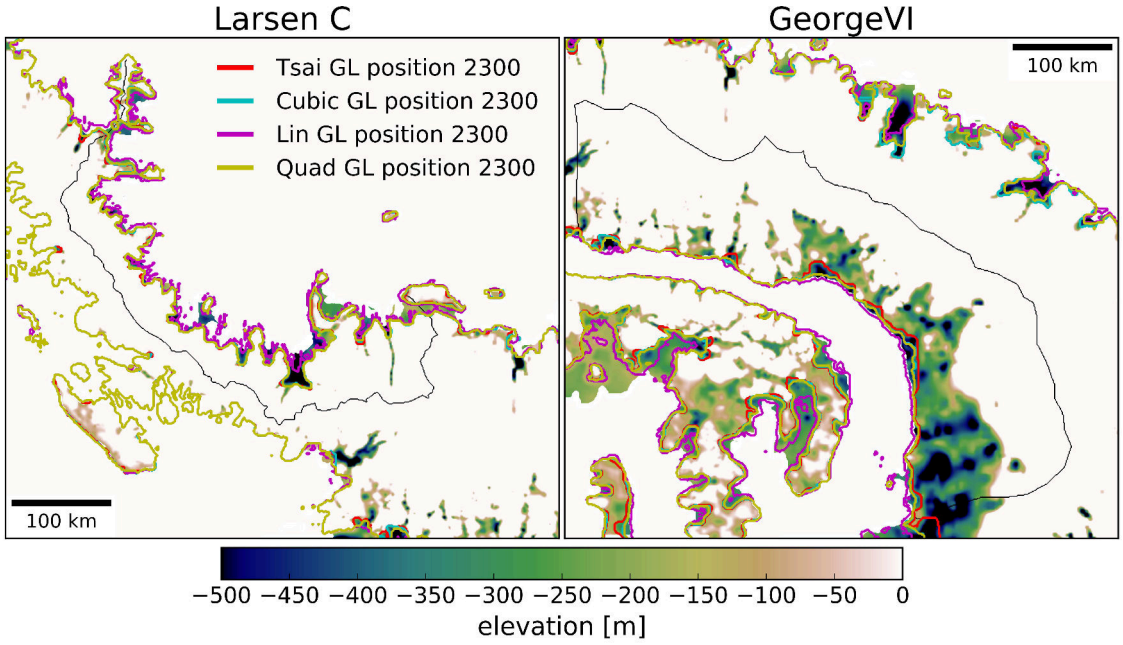

Figure 4.14: Comparison of modelled grounding-line positions with different basal sliding laws for Larsen C (a) and George VI embayments (b). Black outlines show drainage basins.

4.4 Conclusions

In light of Larsen C Ice Shelf potentially becoming unstable following an imminent major calving event (*Jansen et al.*, 2015), our simulations under different forcing scenarios show that SLR projections in response to Larsen C Ice Shelf removal are

limited to <3.0 mm to 2300. This small contribution is due to the fact that the outlet glaciers feeding Larsen C Ice Shelf are relatively small and that most of the grounded ice is located on bedrock well above sea level (Figure 4.1b). Our findings contradict claims that the collapse of Larsen C Ice Shelf should lead to a major drawdown of the region (*Jansen et al.*, 2015).

The main contributor to SLR in our simulations is George VI Ice Shelf, with SLR projections up to 22 mm to 2300, resulting in widespread grounding-line retreat into the marine-based sectors (>20 km). This supports results from earlier modelling studies (Chapters 2 and 3). Considering that this projection is only ∼55% of the grounded ice located below sea level in this area, there may be even more ice at risk to the MISI mechanism.

Of crucial importance for the magnitude of our SLR projections is the basal boundary condition, causing SLR projections to diverge across the sheet-shelf models for the George VI embayment in the calving experiment. SLR projections are even more sensitive to the choice of the basal sliding law (Figure 4.13). While all power laws project a similar range of SLR, SLR projections increase by a factor of two with the use of a pressure-limited sliding law.

The simple ice-sheet model in conjunction with the grounding-line retreat parameterisation is able to project SLR of similar magnitude for both modelling domains, but the spatial match of the modelled dynamic thinning is not very well captured in comparison with the sheet-shelf models, indicating equifinality in the simulation outcomes. The combined SLR projections range from 0.3-23 mm to 2300 for the two modelling domains from ice dynamics alone. This translates to an annual contribution of 0.0-0.1 mm a^{-1} over the next 300 years, which is about 1/3 of the annual SLR contribution from the entire AIS between 2003 and 2013 (*Martín-Español et al.*, 2016). These rates underline the potential importance of APIS to global SLR over the coming centuries.

Chapter 5

Conclusions

5.1 Summary of the main findings

The overarching goal of the research presented in this doctoral thesis was to quantify the ice dynamic SLR from APIS to 2300. To accomplish this, numerical ice-sheet models were used. To provide realistic SLR projections, two main processes have to be simulated: i) the timing of ice-shelf collapse and ii) the migration of the grounding line in response to the collapse event. This problem can be approached by either simulating the entire sheet-shelf system with the appropriate boundary conditions, or alternatively a simpler ice-sheet model can be employed together with parameterisations for ice-shelf collapse and subsequent grounding-line retreat (e.g. *Barrand et al.*, 2013b).

The latter approach was selected to model ice dynamic SLR from ice-shelf tributary glaciers (Chapter 2). A simple linearised SIA ice-sheet model (BAS-APISM), specifically designed for the demands of APIS, was employed. Ice-shelf collapse timing was approximated through a thermal viability limit, tracked in an ensemble of 14 CMIP5 GCM projections for RCP4.5 and RCP8.5 scenarios. Grounding-line retreat in response to ice-shelf removal was parameterised by a multivariate linear

regression model, taking into account a range of different glacier characteristics (e.g. ice speed, size of drainage basin) for each drainage basin. This simpler model set-up is computationally cheap, allowing scenario-based SLR projections under different future climate scenarios. The simulated mulit-model mean upper bound SLR projection from these ice-shelf tributary glaciers ranged from 0-19 mm to 2300, depending on the emission scenario. George VI Ice Shelf was identified as the most important contributor, providing >75% of the total simulated SLR (Chapter 2, Figures 2.11 and 2.12). In these areas, thinning induced through a retreat of the grounding line propagates far upstream (∼135 km), whereas in most other regions of the peninsula thinning is restricted to the areas in the immediate vicinity of the grounding line.

Some of the recent contribution to SLR from the AP has not come from the acceleration of outlet glaciers in response to ice-shelf collapse, but from the acceleration and retreat of tidewater glaciers (e.g. *Cook et al.*, 2005; *Pritchard and Vaughan*, 2007; *Cook et al.*, 2016). To be able to quantify their SLR potential to 2300, tidewater glacier retreat was simulated using three different empirical calving laws (Chapter 3). Tidewater glaciers are expected to contribute between 3.2-18.6 mm to SLR over the next 300 years. While the latter estimate is most likely an upper bound, the exclusion of tidewater glaciers in SLR projections may lead to an underestimation of ice dynamic SLR by >50%. In addition to the inclusion of tidewater glaciers to provide ice-sheet-wide SLR projections, major improvements were made to the statistical grounding-line retreat model and ice-shelf collapse parameterisation. The more physically-realistic grounding-line retreat model is based on Schoof's flux formula (equation 1.24) and scales the expected retreat to the amount of buttressing at the ice front. The set-up of the statistical model also allows the estimation of the uncertainty associated with the parameterisation. While the thermal viability limit seems to be a good approximation for ice-shelf collapse timing, it is not directly related to any processes commonly linked with

ice-shelf collapse. The improved ice-shelf collapse approximation is instead based on the total number of meltdays, and as such is directly linked to the process of hydrofracture. The process that has been linked with the collapse of Larsen B Ice Shelf (*Scambos et al.*, 2003; *van den Broeke*, 2005).

With the improved parameterisations, SLR projections from ice-shelf tributary glaciers are 2.4±1.5 mm and 13.7±8.1 mm for RCP4.5 and RCP8.5. When combined with SLR projections from tidewater glaciers, this leads to an overall SLR of 11.1±3.4 mm to 21.0±3.0 mm for RCP4.5 and 26.7±16.2 mm to 32.3±16.2 mm for RCP8.5 by 2300. Despite slightly lower SLR projections for ice-shelf tributary glaciers in comparison to the scenario-based approach (Chapter 2), the main contributor to SLR remains George VI Ice Shelf. Drainage basins feeding this ice shelf are responsible for 54% of the total simulated SLR, followed by drainage basins feeding Larsen D Ice Shelf South with 14%. Little SLR is projected from Larsen C Ice Shelf, the northern-most of the remaining ice shelves in the AP. The inclusion of tidewater glacier SLR projections however increase the upper bound SLR potential from 19 mm to 26.7±16.2 mm.

To assess the reliability of the SLR projections with the simple ice-sheet model, these projections were compared to more sophisticated and computationally expensive sheet-shelf model simulations (Chapter 4). These types of ice-sheet models provide a more complete mathematical description of ice flow and do not necessitate a parameterisation of grounding-line retreat. For the model intercomparison exercise, George VI Ice Shelf and Larsen C Ice Shelf embayment glaciers were selected as model domains. SLR projections across the three ice-sheet models, at similar horizontal resolution, agree well with each other, ranging from 0.6-1.6 mm for Larsen C Ice Shelf and 5.7-11.0 mm for George VI Ice Shelf. All ice-sheet models agree that very little SLR can be expected from the Larsen C embayment, even in the event of immediate collapse. In terms of SLR potential, George VI Ice Shelf is most important for the AP. Despite SLR projections of similar magnitude in comparison

with the sheet-shelf models, BAS-APISM does not capture well the spatial thinning pattern exhibited by the sheet-shelf models. This discrepancy may well be due to the assumptions made in the statistical model or due to the coarse resolution (5 km) of the input data for the statistical model. Overall, this means that when the computational resources are available, sheet-shelf models (hybrid, HOM, or FS models) should be preferred to the simple but efficient SIA-based ice-sheet models. If computing resources are limited, SIA-based ice-sheet models remain a valuable alternative to gain insights into a complex ice-sheet modelling problem.

Since a significant portion of the George VI embayment is marine-based, the sheet-shelf models were used in conjunction with a physically based calving law (*Benn et al.*, 2007a) to investigate the likelihood of MISI - a self-sustained retreat of the grounding line. Ice-shelf and subsequent tidewater retreat was forced with climate data from a GCM for the RCP4.5 and RCP8.5 scenarios, respectively. While PSU3D did not engage in MISI, BISICLES simulations resulted in grounding-line retreat into the marine-based sectors in the RCP8.5 scenario, resulting in SLR projections for the George VI embayment of up to 22 mm by 2300. The diverging SLR projections across the sheet-shelf models for George VI Ice Shelf are most likely due to different basal traction coefficients inferred by each of the models, leading to very sticky bedrock conditions in PSU3D that inhibits the onset of the retreat modelled with BISICLES. The importance of the basal boundary condition is further highlighted by simulations that use different basal sliding laws. SLR projections using traditional power laws are similar (within 2 mm), but increase by a factor of $\sim$2 for both model domains when a pressure limited sliding law is used. Unlike for the George VI embayment, marine-based grounded ice is limited for Larsen C outlet glaciers. This means that even in the high emission scenario, projections are small at $\sim$1.5 mm. Even under stronger ocean forcing the SLR projections for Larsen C Ice Shelf do not change. Only when the pressure limited sliding law is used do SLR projections increase to 2.8 mm (Figure 4.13a). These

findings contradict earlier claims that a collapse of Larsen C Ice Shelf may lead to a substantial drawdown of the grounded ice upstream. Rather, SLR projections in response to the collapse of the entire Larsen C Ice Shelf are likely to be limited to a maximum of <3 mm.

All three ice-sheet models agree that the AP will continue to be an important contributor to SLR over the next three centuries. While SLR projections are not as high as in West Antarctica (e.g. *DeConto and Pollard*, 2016), RCP8.5 SLR projections go up to 32±16.2 mm with the simple ice-sheet model. However, this number does not take into account the reverse sloping bedrock topography in the George VI embayment. If this is accounted for, the upper bound SLR projection modelled to 2300 for the AP is 43 mm. Considering that these projections are from ice dynamics only and that there is at least 23 mm more of grounded ice stored below sea level in the George VI embayment, more research is needed to better constrain these projections.

5.2 Limitations and scope for further research

It is important to note that the studies presented here are only a first step towards realistic SLR projections from APIS. Some of the limitations of the work undertaken in this thesis have already been identified, but are revisited in the discussion of this section. Along with the presentation of the major limitations, potential for improvements in future work is suggested. At the end of the section, a suggestion is given as to what the most beneficial improvement to the presented results in this thesis would be. The limitations ought to be kept in mind when interpreting the results. Limitations in the presented model projections can be grouped into two major categories; i) limitations due to the employed model set-up; and ii) limitations due to the quality of the input and forcing data.

The most fundamental limitation of all ice-sheet models used in this thesis is the

simplification to the mathematical description of ice flow by dropping terms in the momentum balance equation. This applies primarily to the ice-sheet model employed in Chapter 2 and Chapter 3, as this is the most basic description necessary to describe ice-sheet flow. While widely used, it is important to note that any differences in the approximation of the force balance inevitably lead to varying responses in the respective ice-sheet model, even under equal forcing. This does not necessarily mean that simple ice-sheet models are outdated or that they are inadequate. This depends heavily on the problem under consideration. Simple numerical ice-sheet models are computationally cheap and easy to use. In very simple cases e.g. simplified geometries, they may even allow model verification through comparison with an analytical solution. Such a simplified model led to the derivation of the internal flux boundary condition implemented in PSU3D. In many cases in computational glaciology, the choice of ice-sheet model is not only dictated by the availability of computational resources or the problem under consideration, but also the input data quality. If the input and/or forcing data quality is insufficient, there is no need to use a very sophisticated ice-sheet model. Quite the contrary, using a sophisticated model in these circumstances can lead to interpreting artefacts in model output that are simply a result of the lack of data quality. However, the simple model used in this thesis is valid in areas that are relatively slow moving and additionally is not able to simulate the coupled sheet-shelf system. In such a situation where the coupled sheet-shelf system needs to be simulated, it is certainly recommendable that more sophisticated models are employed. This is even of greater importance when only ice-dynamic SLR is considered as reliable projections hinge on an adequate description of the ice dynamics. In the coupled sheet-shelf system, this includes the stress transfer from ice shelf to ice sheet and *vice versa*, which is ignored in the simple model. Even though the differences in projected SLR are moderate across the three ice-sheet models, SLR projections from the sheet-shelf models are more reliable than from

the simple model as the intercomparison exercise in Chapter 4 showed.

All experiments were designed to focus on the ice dynamic SLR contribution of APIS, omitting some important components of the ice sheet's mass balance such as SMB, basal melting, and isostatic rebound. Hence, this approach provides an incomplete description of total ice-sheet mass loss. For more realistic SLR projections a description of surface mass loss and the effect it may have on ice dynamics is required. Moreover, geometrical changes to ice shelves induced through ocean melting were only incorporated in a very limited number of sensitivity simulations. Even in these simulations, the basal melt rate was set to a spatially invariant value. This presents a very crude approximation of the melt distribution underneath ice shelves and thus is not able to simulate ice-ocean interactions realistically.

A more complete model set-up would certainly improve on the SLR projections presented here. Incorporating SMB projections would be a first step to a more complete system. At the broad scale the consideration of the SMB can have two opposing effects. If the SMB is negative overall than this mass balance term will even lead to higher SLR projections. The opposite is the case if the SMB is positive overall, in which case more ice is stored in the ice sheet and SLR projections would be reduced. However, when interactions between ice dynamics and SMB are included, the problem is more complex than this. The spatial distribution of positive and negative SMB regions might also play a crucial role. If a single glacier has a very negative SMB in the lower reaches, but a very positive SMB in the upper reaches, this can lead to a steepening of the surface slope which in turn increases the driving stress in ice and hence increases ice flux across the grounding line. So even though this glacier has an area-averaged SMB that is near zero, the SLR projections may be higher than for a case where the SMB is near zero everywhere on the glacier. As shown in *Barrand et al.* (2013b), a similar mechanism may come into play if the SMB is positive overall. Over decadal and longer timescales, this leads

to thicker ice throughout the drainage basin. Since ice flow across the grounding line is to first order a function of ice thickness, this positive SMB and hence sea-level drop could be at least partially counterbalanced by a higher ice discharge across the grounding line. Therefore, the effect of SMB on SLR projection depends on the complex interplay between ice dynamics and SMB. By incorporating SMB projections it could be examined whether this increases or dampens overall SLR from APIS. Coupling of the ice-sheet model with a regional ocean circulation model would ensure a realistic representation of ice-ocean interactions. If this coupling is too computationally expensive, the ocean model could be run separately and provide time and spatially varying forcing fields for the ice-sheet model. Even if this approach was shown to potentially lead to different results than a direct coupling (*De Rydt and Gudmundsson*, 2016), it would still mark a significant improvement on the model set-up presented here.

Apart from a more complete description of the sheet-shelf system, there remain large uncertainties in certain parameter choices such as the basal drag coefficient, type of basal sliding law, ocean melt coefficient and bedrock relaxation time. Basic exploration of these parameter spaces were carried out in the sensitivity simulations for this thesis. Owing to the increase in computational power, together with the emergence of a new generation of ice-sheet models, the ice-sheet modelling community has started to use ensemble projections (*Ritz et al.*, 2015; *Pollard et al.*, 2016; *Nias et al.*, 2016), similar to the ensembles used in the climate modelling community e.g. for CMIP5 (*Taylor et al.*, 2011). To provide more robust SLR projections, a large ensemble can be generated that samples the entire plausible parameter space of the uncertain parameters (e.g. *Nias et al.*, 2016). Each ensemble member's SLR projection could then be weighed based on the skill of this parameter combination to simulate the current state of the ice sheet. This can be done at various levels of complexity, ranging from a simple averaging method to advanced statistical techniques involving emulators and likelihood functions (*Pollard et al.*,

2016). As computational resources remain finite, the number of the uncertain parameters is limited and preference should be given to parameters that matter most on the timescales considered. In addition, to provide better constrained SLR projections, these advanced statistical techniques provide smooth probability density functions in parameter space.

For a sheet-shelf model to accurately and reliably model grounding-line migration, high-resolution bedrock topography maps are required. Even though the bedrock topography from BEDMAP2 (*Fretwell et al.*, 2013) is provided on a 1 km horizontal grid resolution, the density of actual measurements is much coarser, especially in parts of the AP region. To provide a complete map of bedrock topography interpolation techniques are used. The interpolation however is not mass conserving, leading to physically untenable high flux divergence (hundreds of metres per year) in high-resolution ice-sheet models after initialisation. This is because ice velocity and geostatistically interpolated bedrock topography do not match (*Morlighem et al.*, 2014b). As demonstrated by the simulations in Chapter 4, small bedrock highs can halt grounding-line retreat, resulting in lower SLR projections. A more consistent and mass-conserving bedrock map could be generated by using the mass conservation equation, along with high resolution ice velocity and surface mass balance fields (e.g. *Morlighem et al.*, 2014a, 2011, 2014b). This method has been used to generate a new bedrock topography map for the Greenland ice sheet (*Morlighem et al.*, 2014b). The new map displays a more plausible and consistent distribution of bedrock features, including bedrock channels extending all the way to the grounding line. Using the same algorithm for the AP, where high resolution velocity and surface mass balance fields are available, would likely improve the reliability of SLR projections.

The implementation of Benn's calving law (*Benn et al.*, 2007a) allows for the explicit modelling of ice-shelf retreat. At each time step, crevasse depth is computed. If crevasses have propagated far enough through the ice column, iceberg calving

takes place. At the following time step, this procedure is repeated without taking into account the crevasse depth and distribution of the previous time step. This unphysical behaviour could be improved by advecting the crevasse field of the previous time step using the velocities from the solution of the momentum balance equation (*Sun et al.*, 2017). This would ensure that the ice-sheet model retains a memory of heavily crevassed regions. As a consequence of this, these mechanically weakened regions would then need less tensile force to trigger calving, resulting in a more physically realistic behaviour of calving front motion.

Taking into account the main conclusions of this thesis and the principal limitations associated with it, improvements to the SLR projections could be achieved with relatively little effort by generating ensemble projections of SLR for APIS. This would immediately constrain projections better and shed more light onto the magnitude of uncertainties associated with the basal boundary condition.

Bibliography

Alley, R. B., H. J. Horgan, I. Joughin, K. M. Cuffey, T. K. Dupont, B. R. Parizek, S. Anandakrishnan, and J. Bassis (2008), A simple law for ice-shelf calving, *Science*, *322*(5906), 1344–1344, doi:10.1126/science.1162543.

Alley, R. B., S. Anandakrishnan, K. Christianson, H. J. Horgan, A. Muto, B. R. Parizek, D. Pollard, and R. T. Walker (2015), Oceanic forcing of ice-sheet retreat: West Antarctica and more, *Annual Review of Earth and Planetary Sciences*, *43*, 207-231.

Arthern, R. J., D. P. Winebrenner, and D. G. Vaughan (2006), Antarctic snow accumulation mapped using polarization of 4.3-cm wavelength microwave emission, *Journal of Geophysical Research: Atmospheres*, *111*(D6), 2156-2202, doi:10.1029/2004JD005667.

Arthern, R. J., R. C. A. Hindmarsh, and C. R. Williams (2015), Flow speed within the Antarctic ice sheet and its controls inferred from satellite observations, *Journal of Geophysical Research: Earth Surface*, *120*(7), 1171-1188, doi:10.1002/2014JF003239.

Baral, D. R., K. Hutter, and R. Greve (2001), Asymptotic theories of large-scale motion, temperature, and moisture distribution in land-based polythermal ice sheets: A critical review and new developments, *Applied Mechanics Reviews*, *54*(3), 215-256, doi:10.1115/1.3097296, 10.1115/1.3097296.

Barletta, V. R., L. S. Sörensen, and R. Forsberg (2013), Scatter of mass changes estimates at basin scale for Greenland and Antarctica, *The Cryosphere*, *7*(5), 1411-1432, doi:10.5194/tc-7-1411-2013.

Barrand, N. E., D. G. Vaughan, N. Steiner, M. Tedesco, P. Kuipers Munneke, M. R. van den Broeke, and J. S. Hosking (2013a), Trends in Antarctic Peninsula surface melting conditions from observations and regional climate modeling, *Journal of Geophysical Research: Earth Surface*, *118*(1), 315-330, doi:10.1029/2012JF002559.

Barrand, N. E., R. C. A. Hindmarsh, R. J. Arthern, C. R. Williams, J. Mouginot, B. Scheuchl, E. Rignot, S. R. M. Ligtenberg, M. R. Van Den Broeke, T. L. Edwards, A. J. Cook, and S. B. Simonsen (2013b), Computing the volume response of the

Antarctic Peninsula ice sheet to warming scenarios to 2200, *Journal of Glaciology*, *59*(215), 397-409, doi:10.3189/2013JoG12J139.

Barrand, N. E., H. Machguth, and J. O. Hagen (2013c), Observing changes in near-polar glaciers in the northern and southern hemispheres, *Eos, Transactions American Geophysical Union*, *94*(23), 208-208, doi:10.1002/2013EO230007.

Benn, D. I., N. R. J. Hulton, and R. H. Mottram (2007a), 'Calving laws', 'sliding laws' and the stability of tidewater glaciers, *Annals of Glaciology*, *46*(1), 123-130, doi:10.3189/172756407782871161.

Benn, D. I., C. R. Warren, and R. H. Mottram (2007b), Calving processes and the dynamics of calving glaciers, *Earth-Science Reviews*, *82*(3-4), 143-179, doi:10.1016/j.earscirev.2007.02.002.

Bernales, J., I. Rogozhina, R. Greve, and M. Thomas (2017), Comparison of hybrid schemes for the combination of shallow approximations in numerical simulations of the Antarctic ice sheet, *The Cryosphere*, *11*(1), 247-265, doi:10.5194/tc-11-247-2017.

Blatter, H. (1995), Velocity and stress fields in grounded glaciers: A simple algorithm for including deviatoric stress gradients, *Journal of Glaciology*, *41*(138), 333-344, doi:10.3198/1995JoG41-138-333-344.

Borstad, C., A. Khazendar, B. Scheuchl, M. Morlighem, E. Larour, and E. Rignot (2016), A constitutive framework for predicting weakening and reduced buttressing of ice shelves based on observations of the progressive deterioration of the remnant Larsen B Ice Shelf, *Geophysical Research Letters*, *43*(5), 2027-2035, doi:10.1002/2015GL067365.

Borstad, C. P., E. Rignot, J. Mouginot, and M. P. Schodlok (2013), Creep deformation and buttressing capacity of damaged ice shelves: Theory and application to Larsen C Ice Shelf, *The Cryosphere*, *7*(6), 1931-1947, doi:10.5194/tc-7-1931-2013.

Box, J. E., X. Fettweis, J. C. Stroeve, M. Tedesco, D. K. Hall, and K. Steffen (2012), Greenland ice sheet albedo feedback: Thermodynamics and atmospheric drivers, *The Cryosphere*, *6*(4), 821–839, doi:10.5194/tc-6-821-2012.

Bromwich, D. H., Z. Guo, L. Bai, and Q.-s. Chen (2004), Modeled Antarctic precipitation. Part I: Spatial and temporal variability, *Journal of Climate*, *17*(3), 427-447, doi:10.1175/1520-0442(2004)017⟨0427:mappis⟩2.0.co;2.

Brown, C. S., M. F. Meier, and A. Post (1982), Calving speed of Alaska tidewater glaciers, with application to Columbia Glacier, *USGS Professional Paper*, *1258-C*, C1-C13.

Brunt, K. M., H. A. Fricker, L. Padman, T. A. Scambos, and S. O'Neel (2010), Mapping the grounding zone of the Ross Ice Shelf, Antarctica, using ICESat laser altimetry, *Annals of Glaciology*, *51*(55), 71-79, doi:10.3189/172756410791392790.

Cook, A., D. Vaughan, A. Luckman, and T. Murray (2014), A new Antarctic Peninsula glacier basin inventory and observed area changes since the 1940s, *Antarctic Science*, *26*(Special Issue 06), 614-624, doi:10.1017/S0954102014000200.

Cook, A. J., and D. G. Vaughan (2010), Overview of areal changes of the ice shelves on the Antarctic Peninsula over the past 50 years, *The Cryosphere*, *4*(1), 77-98, doi: 10.5194/tc-4-77-2010.

Cook, A. J., A. J. Fox, D. G. Vaughan, and J. G. Ferrigno (2005), Retreating glacier fronts on the Antarctic Peninsula over the past half-century, *Science*, *308*(5721), 541-544, doi:10.1126/science.1104235.

Cook, A. J., P. R. Holland, M. P. Meredith, T. Murray, A. Luckman, and D. G. Vaughan (2016), Ocean forcing of glacier retreat in the western Antarctic Peninsula, *Science*, *353*(6296), 283–286, doi:10.1126/science.aae0017.

Cornford, S. L., D. F. Martin, D. T. Graves, D. F. Ranken, A. M. Le Brocq, R. M. Gladstone, A. J. Payne, E. G. Ng, and W. H. Lipscomb (2013), Adaptive mesh, finite volume modeling of marine ice sheets, *Journal of Computational Physics*, *232*(1), 529-549, doi:10.1016/j.jcp.2012.08.037.

Cornford, S. L., D. F. Martin, A. J. Payne, E. G. Ng, A. M. Le Brocq, R. M. Gladstone, T. L. Edwards, S. R. Shannon, C. Agosta, M. R. van den Broeke, H. H. Hellmer, G. Krinner, S. R. M. Ligtenberg, R. Timmermann, and D. G. Vaughan (2015), Century-scale simulations of the response of the West Antarctic Ice Sheet to a warming climate, *The Cryosphere*, *9*(4), 1579-1600, doi:10.5194/tc-9-1579-2015.

Cornford, S. L., D. F. Martin, V. Lee, A. J. Payne, and E. G. Ng (2016), Adaptive mesh refinement versus subgrid friction interpolation in simulations of Antarctic ice dynamics, *Annals of Glaciology*, *57*(73), 1-9, doi:10.1017/aog.2016.13.

Corr, H. F. J., C. S. M. Doake, A. Jenkins, and D. G. Vaughan (2001), Investigations of an "ice plain" in the mouth of Pine Island Glacier, Antarctica, *Journal of Glaciology*, *47*(156), 51-57, doi:10.3189/172756501781832395.

Cuffey, K. M., and W. S. B. Paterson (2010), *The physics of glaciers*, Academic Press.

De Angelis, H., and P. Skvarca (2003), Glacier surge after ice shelf collapse, *Science*, *299*(5612), 1560-1562, doi:10.1126/science.1077987.

De Rydt, J., and G. H. Gudmundsson (2016), Coupled ice shelf-ocean modeling and complex grounding line retreat from a seabed ridge, *Journal of Geophysical Research: Earth Surface*, *121*(5), 865-880, doi:10.1002/2015JF003791.

De Rydt, J., G. H. Gudmundsson, H. Rott, and J. L. Bamber (2015), Modeling

the instantaneous response of glaciers after the collapse of the Larsen B Ice Shelf, *Geophysical Research Letters*, *42*(13), 5355-5363, doi:10.1002/2015GL064355.

DeConto, R. M., and D. Pollard (2016), Contribution of Antarctica to past and future sea-level rise, *Nature*, *531*(7596), 591-597, doi:10.1038/nature17145.

Dee, D. P., S. M. Uppala, A. J. Simmons, P. Berrisford, P. Poli, S. Kobayashi, U. Andrae, M. A. Balmaseda, G. Balsamo, P. Bauer, P. Bechtold, A. C. M. Beljaars, L. van de Berg, J. Bidlot, N. Bormann, C. Delsol, R. Dragani, M. Fuentes, A. J. Geer, L. Haimberger, S. B. Healy, H. Hersbach, E. V. Hólm, L. Isaksen, P. Kållberg, M. Köhler, M. Matricardi, A. P. McNally, B. M. Monge-Sanz, J. J. Morcrette, B. K. Park, C. Peubey, P. de Rosnay, C. Tavolato, J. N. Thépaut, and F. Vitart (2011), The ERA-Interim reanalysis: Configuration and performance of the data assimilation system, *Quarterly Journal of the Royal Meteorological Society*, *137*(656), 553-597, doi: 10.1002/qj.828.

Depoorter, M. A., J. L. Bamber, J. A. Griggs, J. T. M. Lenaerts, S. R. M. Ligtenberg, M. R. van den Broeke, and G. Moholdt (2013), Calving fluxes and basal melt rates of Antarctic ice shelves, *Nature*, *502*(7469), 89-92, doi:10.1038/nature12567.

Durand, G., O. Gagliardini, T. Zwinger, E. Le Meur, and R. C. A. Hindmarsh (2009), Full stokes modeling of marine ice sheets: Influence of the grid size, *Annals of Glaciology*, *50*(52), 109-114, doi:10.3189/172756409789624283.

Edwards, T. L., X. Fettweis, O. Gagliardini, F. Gillet-Chaulet, H. Goelzer, J. M. Gregory, M. Hoffman, P. Huybrechts, A. J. Payne, M. Perego, S. Price, A. Quiquet, and C. Ritz (2014), Probabilistic parameterisation of the surface mass balance-elevation feedback in regional climate model simulations of the Greenland ice sheet, *The Cryosphere*, *8*(1), 181–194, doi:10.5194/tc-8-181-2014.

Enderlin, E. M., I. M. Howat, S. Jeong, M.-J. Noh, J. H. van Angelen, and M. R. van den Broeke (2014), An improved mass budget for the Greenland ice sheet, *Geophysical Research Letters*, *41*(3), 866-872, doi:10.1002/2013GL059010.

Farinotti, D., E. C. King, A. Albrecht, M. Huss, and G. H. Gudmundsson (2014), The bedrock topography of Starbuck Glacier, Antarctic Peninsula, as determined by radio-echo soundings and flow modeling, *Annals of Glaciology*, *55*(67), 22-28, doi:10.3189/2014AoG67A025.

Favier, L., G. Durand, S. L. Cornford, G. H. Gudmundsson, O. Gagliardini, F. Gillet-Chaulet, T. Zwinger, A. J. Payne, and A. M. Le Brocq (2014), Retreat of Pine Island Glacier controlled by marine ice-sheet instability, *Nature Clim. Change*, *4*(2), 117-121, doi:10.1038/nclimate2094.

Fretwell, P., H. D. Pritchard, D. G. Vaughan, J. L. Bamber, N. E. Barrand, R. Bell,

C. Bianchi, R. G. Bingham, D. D. Blankenship, G. Casassa, G. Catania, D. Callens, H. Conway, A. J. Cook, H. F. J. Corr, D. Damaske, V. Damm, F. Ferraccioli, R. Forsberg, S. Fujita, Y. Gim, P. Gogineni, J. A. Griggs, R. C. A. Hindmarsh, P. Holmlund, J. W. Holt, R. W. Jacobel, A. Jenkins, W. Jokat, T. Jordan, E. C. King, J. Kohler, W. Krabill, M. Riger-Kusk, K. A. Langley, G. Leitchenkov, C. Leuschen, B. P. Luyendyk, K. Matsuoka, J. Mouginot, F. O. Nitsche, Y. Nogi, O. A. Nost, S. V. Popov, E. Rignot, D. M. Rippin, A. Rivera, J. Roberts, N. Ross, M. J. Siegert, A. M. Smith, D. Steinhage, M. Studinger, B. Sun, B. K. Tinto, B. C. Welch, D. Wilson, D. A. Young, C. Xiangbin, and A. Zirizzotti (2013), Bedmap2: Improved ice bed, surface and thickness datasets for Antarctica, *The Cryosphere*, *7*(1), 375-393, doi: 10.5194/tc-7-375-2013.

Fricker, H. A., and L. Padman (2012), Thirty years of elevation change on Antarctic Peninsula ice shelves from multimission satellite radar altimetry, *Journal of Geophysical Research: Oceans*, *117*(C2), 2156-2202, doi:10.1029/2011JC007126.

Fricker, H. A., R. Coleman, L. Padman, T. A. Scambos, J. Bohlander, and K. M. Brunt (), Mapping the grounding zone of the Amery Ice Shelf, East Antarctica using InSAR, MODIS and ICESat, *Antarctic Science*, *21*.

Fürst, J. J., G. Durand, F. Gillet-Chaulet, N. Merino, L. Tavard, J. Mouginot, N. Gourmelen, and O. Gagliardini (2015), Assimilation of Antarctic velocity observations provides evidence for uncharted pinning points, *The Cryosphere*, *9*(4), 1427–1443, doi:10.5194/tc-9-1427-2015.

Fürst, J. J., G. Durand, F. Gillet-Chaulet, L. Tavard, M. Rankl, M. Braun, and O. Gagliardini (2016), The safety band of Antarctic ice shelves, *Nature Clim. Change*, *6*, 479-482, doi:10.1038/nclimate2912.

Fyke, J. G., L. Carter, A. Mackintosh, A. J. Weaver, and K. J. Meissner (2010), Surface melting over ice shelves and ice sheets as assessed from modeled surface air temperatures, *Journal of Climate*, *23*(7), 1929-1936, doi:10.1175/2009JCLI3122.1.

Gagliardini, O., T. Zwinger, F. Gillet-Chaulet, G. Durand, L. Favier, B. de Fleurian, R. Greve, M. Malinen, C. Martín, P. Råback, J. Ruokolainen, M. Sacchettini, M. Schäfer, H. Seddik, and J. Thies (2013), Capabilities and performance of Elmer/Ice, a new-generation ice sheet model, *Geosci. Model Dev.*, *6*(4), 1299-1318, doi:10.5194/gmd-6-1299-2013.

Giovinetto, M. (1985), Surface balance in ice drainage systems of Antarctica, *Antarctic Journal of the United States*, *20*(4), 6–13.

Giovinetto, M. B., and H. J. Zwally (2000), Spatial distribution of net surface accumulation on the Antarctic ice sheet, *Annals of Glaciology*, *31*(1), 171-178, doi: 10.3189/172756400781820200.

Giovinetto, M. B., C. R. Bentley, and C. Bull (1989), *Choosing between some incompatible regional surface-mass-balance data sets in Antarctica*, National Science Foundation.

Gladstone, R. M., A. J. Payne, and S. L. Cornford (2010), Parameterising the grounding line in flow-line ice sheet models, *The Cryosphere*, *4*(4), 605-619, doi: 10.5194/tc-4-605-2010.

Goldberg, D., D. M. Holland, and C. Schoof (2009), Grounding line movement and ice shelf buttressing in marine ice sheets, *Journal of Geophysical Research: Earth Surface*, *114*(F4), F04026, doi:10.1029/2008JF001227.

Greve, R., and H. Blatter (2009), *Dynamics of ice sheets and glaciers*, Springer Science and Business Media.

Gudmundsson, G. H. (2013), Ice-shelf buttressing and the stability of marine ice sheets, *The Cryosphere*, *7*(2), 647-655, doi:10.5194/tc-7-647-2013.

Gudmundsson, G. H., J. Krug, G. Durand, L. Favier, and O. Gagliardini (2012), The stability of grounding lines on retrograde slopes, *The Cryosphere*, *6*(6), 1497-1505, doi:10.5194/tc-6-1497-2012.

Hagen, J., and N. Reeh (2004), *In situ measurement techniques: Land ice*, pp. 11–41, Cambridge University Press.

Hair, J. F., B. Black, R. Anderson, and R. Tatham (1995), *Multivariate Data Analysis with Readings*, 4th ed., Prentice-Hall, Inc, New Jersey.

Hanna, E., F. J. Navarro, F. Pattyn, C. M. Domingues, X. Fettweis, E. R. Ivins, R. J. Nicholls, C. Ritz, B. Smith, S. Tulaczyk, P. L. Whitehouse, and H. J. Zwally (2013), Ice-sheet mass balance and climate change, *Nature*, *498*(7452), 51-59, doi:10.1038/nature12238.

Harig, C., and F. J. Simons (2015), Accelerated West Antarctic ice mass loss continues to outpace East Antarctic gains, *Earth and Planetary Science Letters*, *415*, 134-141, doi:10.1016/j.epsl.2015.01.029.

Held, I. M., and B. J. Soden (2006), Robust responses of the hydrological cycle to global warming, *Journal of Climate*, *19*(21), 5686-5699, doi:10.1175/jcli3990.1.

Helm, V., A. Humbert, and H. Miller (2014), Elevation and elevation change of Greenland and Antarctica derived from CryoSat-2, *The Cryosphere*, *8*(4), 1539-1559, doi:10.5194/tc-8-1539-2014.

Hindmarsh, R. C. A. (2004), A numerical comparison of approximations to the Stokes equations used in ice sheet and glacier modeling, *Journal of Geophysical Research: Earth Surface*, *109*(F1), F01012, doi:10.1029/2003JF000065.

Hindmarsh, R. C. A. (2009), Consistent generation of ice-streams via thermo-viscous instabilities modulated by membrane stresses, *Geophysical Research Letters*, *36*(6), L06502, doi:10.1029/2008GL036877.

Hock, R., M. de Woul, V. Radic, and M. Dyurgerov (2009), Mountain glaciers and ice caps around Antarctica make a large sea-level rise contribution, *Geophysical Research Letters*, *36*(7), L07501, doi:10.1029/2008GL037020.

Holland, P. R., A. Jenkins, and D. M. Holland (2008), The response of ice shelf basal melting to variations in ocean temperature, *Journal of Climate*, *21*(11), 2558-2572, doi:10.1175/2007JCLI1909.1.

Holland, P. R., H. F. J. Corr, H. D. Pritchard, D. G. Vaughan, R. J. Arthern, A. Jenkins, and M. Tedesco (2011), The air content of Larsen Ice Shelf, *Geophysical Research Letters*, *38*(10), L10503, doi:10.1029/2011GL047245.

Holland, P. R., A. Brisbourne, H. F. J. Corr, D. McGrath, K. Purdon, J. Paden, H. A. Fricker, F. S. Paolo, and A. H. Fleming (2015), Oceanic and atmospheric forcing of Larsen C Ice-Shelf thinning, *The Cryosphere*, *9*(3), 1005-1024, doi:10.5194/tc-9-1005-2015.

Holt, T. O., N. F. Glasser, D. J. Quincey, and M. R. Siegfried (2013), Speedup and fracturing of George VI Ice Shelf, Antarctic Peninsula, *The Cryosphere*, *7*(3), 797-816, doi:10.5194/tc-7-797-2013.

Horgan, H. J., and S. Anandakrishnan (2006), Static grounding lines and dynamic ice streams: Evidence from the Siple Coast, West Antarctica, *Geophysical Research Letters*, *33*(18), L18502, doi:10.1029/2006GL027091.

Hu, A., G. A. Meehl, W. Han, and J. Yin (2009), Transient response of the MOC and climate to potential melting of the Greenland Ice Sheet in the 21st century, *Geophysical Research Letters*, *36*(10), L10707, doi:10.1029/2009GL037998.

Huang, B., V. F. Banzon, E. Freeman, J. Lawrimore, W. Liu, T. C. Peterson, T. M. Smith, P. W. Thorne, S. D. Woodruff, and H.-M. Zhang (2015), Extended Reconstructed Sea Surface Temperature Version 4 (ERSST.v4). Part I: Upgrades and intercomparisons, *Journal of Climate*, *28*(3), 911-930, doi:10.1175/JCLI-D-14-00006.1.

Huss, M., and D. Farinotti (2014), A high-resolution bedrock map for the Antarctic Peninsula, *The Cryosphere*, *8*(4), 1261-1273, doi:10.5194/tc-8-1261-2014.

Hutter, K. (1983), *Theoretical glaciology: Material science of ice and the mechanics of glaciers and ice sheets*, vol. 1, Springer.

Huybrechts, P. (2009), Global change: West-side story of Antarctic ice, *Nature*, *458*(7236), 295-296, doi:10.1038/458295a.

Ivins, E. R., T. S. James, J. Wahr, E. J. O. Schrama, F. W. Landerer, and K. M. Simon (2013), Antarctic contribution to sea level rise observed by GRACE with improved GIA correction, *Journal of Geophysical Research: Solid Earth*, *118*(6), 3126-3141, doi: 10.1002/jgrb.50208.

Jacob, T., J. Wahr, W. T. Pfeffer, and S. Swenson (2012), Recent contributions of glaciers and ice caps to sea level rise, *Nature*, *482*(7386), 514-518, doi:10.1038/nature10847.

Jacobs, S. S., H. H. Helmer, C. S. M. Doake, A. Jenkins, and R. M. Frolich (1992), Melting of ice shelves and the mass balance of Antarctica, *Journal of Glaciology*, *38*(130), 375-387, doi:10.3198/1992JoG38-130-375-387.

James, T. D., T. Murray, N. Selmes, K. Scharrer, and M. O'Leary (2014), Buoyant flexure and basal crevassing in dynamic mass loss at Helheim Glacier, *Nature Geosci*, *7*(8), 593-596, doi:10.1038/ngeo2204.

Jansen, D., B. Kulessa, P. R. Sammonds, A. Luckman, E. C. King, and N. F. Glasser (2010), Present stability of the Larsen C Ice Shelf, Antarctic Peninsula, *Journal of Glaciology*, *56*(198), 593-600, doi:10.3189/002214310793146223.

Jansen, D., A. J. Luckman, A. Cook, S. Bevan, B. Kulessa, B. Hubbard, and P. R. Holland (2015), Brief communication: Newly developing rift in Larsen C Ice Shelf presents significant risk to stability, *The Cryosphere*, *9*(3), 1223-1227, doi:10.5194/tc-9-1223-2015.

Jenkins, A., and S. Jacobs (2008), Circulation and melting beneath George VI Ice Shelf, Antarctica, *Journal of Geophysical Research: Oceans*, *113*(C4), C04013, doi:10.1029/2007JC004449.

Jones, P. D., and D. H. Lister (2014), Antarctic near-surface air temperatures compared with ERA-Interim values since 1979, *International Journal of Climatology*, *35*(7), 1354-1366, doi:10.1002/joc.4061.

Joughin, I., and R. B. Alley (2011), Stability of the West Antarctic ice sheet in a warming world, *Nature Geosci*, *4*(8), 506-513, 10.1038/ngeo1194.

Joughin, I., B. E. Smith, and D. M. Holland (2010), Sensitivity of 21st century sea level to ocean-induced thinning of Pine Island Glacier, Antarctica, *Geophysical Research Letters*, *37*(20), L20502, doi:10.1029/2010GL044819.

Joughin, I., B. E. Smith, and B. Medley (2014), Marine ice sheet collapse potentially under way for the Thwaites Glacier basin, West Antarctica, *Science*, *344*(6185), 735-738, doi:10.1126/science.1249055.

Joughin, I., D. E. Shean, B. E. Smith, and P. Dutrieux (2016), Grounding line variability

and subglacial lake drainage on Pine Island Glacier, Antarctica, *Geophysical Research Letters*, *43*(17), 9093-9102, doi:10.1002/2016GL070259.

Khazendar, A., C. P. Borstad, B. Scheuchl, E. Rignot, and H. Seroussi (2015), The evolving instability of the remnant Larsen B Ice Shelf and its tributary glaciers, *Earth and Planetary Science Letters*, *419*, 199-210, doi:10.1016/j.epsl.2015.03.014.

King, M. A., R. J. Bingham, P. Moore, P. L. Whitehouse, M. J. Bentley, and G. A. Milne (2012), Lower satellite-gravimetry estimates of Antarctic sea-level contribution, *Nature*, *491*(7425), 586-589, doi:10.1038/nature11621.

Kirchner, N., K. Hutter, M. Jakobsson, and R. Gyllencreutz (2011), Capabilities and limitations of numerical ice sheet models: A discussion for earth-scientists and modelers, *Quaternary Science Reviews*, *30*(25–26), 3691-3704, doi:10.1016/j.quascirev.2011.09.012.

Kulessa, B., D. Jansen, A. J. Luckman, E. C. King, and P. R. Sammonds (2014), Marine ice regulates the future stability of a large Antarctic ice shelf, *Nat Commun*, *5*, 3707, doi:10.1038/ncomms4707.

Larour, E., H. Seroussi, M. Morlighem, and E. Rignot (2012), Continental scale, high order, high spatial resolution, ice sheet modeling using the Ice Sheet System Model (ISSM), *Journal of Geophysical Research: Earth Surface*, *117*(F1), F01022, doi:10.1029/2011JF002140.

Le Brocq, A. M., A. J. Payne, and A. Vieli (2010), An improved Antarctic dataset for high resolution numerical ice sheet models (ALBMAP v1), *Earth System Science Data*, *2*(2), 247–260, doi:10.5194/essd-2-247-2010.

Lenaerts, J. T. M., M. R. van den Broeke, W. J. van de Berg, E. van Meijgaard, and P. Kuipers Munneke (2012), A new, high-resolution surface mass balance map of Antarctica (1979-2010) based on regional atmospheric climate modeling, *Geophysical Research Letters*, *39*(4), L04501, doi:10.1029/2011GL050713.

Levitus, S., J. Antonov, O. K. Baranova, T. Boyer, C. Coleman, H. Garcia, A. Grodsky, D. Johnson, R. Locarnini, A. V. Mishonov, C. O'Brien, J. Reagan, D. Seidov, I. Smolyar, and M. Zweng (2013), The world ocean database, *Data Science Journal*, *12*(0), WDS229–WDS234.

Ligtenberg, S. R. M., W. J. van de Berg, M. R. van den Broeke, J. G. L. Rae, and E. van Meijgaard (2013), Future surface mass balance of the Antarctic ice sheet and its influence on sea level change, simulated by a regional atmospheric climate model, *Climate Dynamics*, *41*(3), 867-884, doi:10.1007/s00382-013-1749-1.

Luckman, A., A. Elvidge, D. Jansen, B. Kulessa, P. Kuipers Munneke, J. King, and N. E. Barrand (2014), Surface melt and ponding on Larsen C Ice Shelf and

the impact of foehn winds, *Antarctic Science*, *26*(Special Issue 06), 625-635, doi: 10.1017/S0954102014000339.

Luckman, A., D. I. Benn, F. Cottier, S. Bevan, F. Nilsen, and M. Inall (2015), Calving rates at tidewater glaciers vary strongly with ocean temperature, *Nat Commun*, *6*, 8566, doi:10.1038/ncomms9566.

MacAyeal, D. R. (1989), Large-scale ice flow over a viscous basal sediment: Theory and application to Ice Stream B, Antarctica, *Journal of Geophysical Research: Solid Earth*, *94*(B4), 4071-4087, doi:10.1029/JB094iB04p04071.

MacAyeal, D. R. (1992), The basal stress distribution of Ice Stream E, Antarctica, inferred by control methods, *Journal of Geophysical Research: Solid Earth*, *97*(B1), 595–603, doi:10.1029/91JB02454.

Martín-Español, A., A. Zammit-Mangion, P. J. Clarke, T. Flament, V. Helm, M. A. King, S. B. Luthcke, E. Petrie, F. Rémy, N. Schön, B. Wouters, and J. L. Bamber (2016), Spatial and temporal Antarctic ice sheet mass trends, glacio-isostatic adjustment, and surface processes from a joint inversion of satellite altimeter, gravity, and GPS data, *Journal of Geophysical Research: Earth Surface*, *121*(2), 182-200, doi:10.1002/2015JF003550.

McGrath, D., K. Steffen, P. R. Holland, T. Scambos, H. Rajaram, W. Abdalati, and E. Rignot (2014), The structure and effect of suture zones in the Larsen C Ice Shelf, Antarctica, *Journal of Geophysical Research: Earth Surface*, *119*(3), 588-602, doi:10.1002/2013JF002935.

McMillan, M., A. Shepherd, A. Sundal, K. Briggs, A. Muir, A. Ridout, A. Hogg, and D. Wingham (2014), Increased ice losses from Antarctica detected by CryoSat-2, *Geophysical Research Letters*, *41*(11), 3899-3905, doi:10.1002/2014GL060111.

Mercer, J. H. (1978), West Antarctic ice sheet and CO2 greenhouse effect: A threat of disaster, *Nature*, *271*(5643), 321-325, doi:10.1038/271321a0.

Meredith, M. P., and J. C. King (2005), Rapid climate change in the ocean west of the Antarctic Peninsula during the second half of the 20th century, *Geophysical Research Letters*, *32*(19), L19604, doi:10.1029/2005GL024042.

Morland, L. W., and R. Zainuddin (1987), *Plane and Radial Ice-Shelf Flow with Prescribed Temperature Profile*, pp. 117–140, Springer Netherlands, Dordrecht, doi: 10.1007/978-94-009-3745-1_7.

Morlighem, M., E. Rignot, H. Seroussi, E. Larour, H. Ben Dhia, and D. Aubry (2011), A mass conservation approach for mapping glacier ice thickness, *Geophysical Research Letters*, *38*(19), L19503, doi:10.1029/2011GL048659.

Morlighem, M., E. Rignot, J. Mouginot, H. Seroussi, and E. Larour (2014a), High-resolution ice-thickness mapping in south Greenland, *Annals of Glaciology*, *55*(67), 64-70, doi:doi:10.3189/2014AoG67A088.

Morlighem, M., E. Rignot, J. Mouginot, H. Seroussi, and E. Larour (2014b), Deeply incised submarine glacial valleys beneath the Greenland ice sheet, *Nature Geosci*, *7*(6), 418-422, doi:10.1038/ngeo2167.

Morris, E. M., and D. G. Vaughan (2003), *Spatial and temporal variation of surface temperature on the Antarctic Peninsula and the limit of viability of ice shelves*, pp. 61–68, American Geophysical Union, doi:10.1029/AR079p0061.

Mouginot, J., E. Rignot, and B. Scheuchl (2014), Sustained increase in ice discharge from the Amundsen Sea Embayment, West Antarctica, from 1973 to 2013, *Geophysical Research Letters*, *41*(5), 1576-1584, doi:10.1002/2013GL059069.

Munneke, P. K., S. R. M. Ligtenberg, M. R. Van Den Broeke, and D. G. Vaughan (2014), Firn air depletion as a precursor of Antarctic ice-shelf collapse, *Journal of Glaciology*, *60*(220), 205-214, doi:10.3189/2014JoG13J183.

Nias, I. J., S. L. Cornford, and A. J. Payne (2016), Contrasting the modelled sensitivity of the Amundsen Sea Embayment ice streams, *Journal of Glaciology*, *62*(233), 552-562, doi:10.1017/jog.2016.40.

Nicholls, K. W., C. J. Pudsey, and P. Morris (2004), Summertime water masses off the northern Larsen C Ice Shelf, Antarctica, *Geophysical Research Letters*, *31*(9), L09309, doi:10.1029/2004GL019924.

Nicholls, K. W., K. Makinson, and E. J. Venables (2012), Ocean circulation beneath Larsen C Ice Shelf, Antarctica from in situ observations, *Geophysical Research Letters*, *39*(19), L19608, doi:10.1029/2012GL053187.

Nick, F. M., and J. Oerlemans (2006), Dynamics of tidewater glaciers: Comparison of three models, *Journal of Glaciology*, *52*(177), 183-190, doi:10.3189/172756506781828755.

Nick, F. M., C. J. van der Veen, A. Vieli, and D. I. Benn (2010), A physically based calving model applied to marine outlet glaciers and implications for the glacier dynamics, *Journal of Glaciology*, *56*(199), 781-794, doi:10.3189/002214310794457344.

Nick, F. M., A. Vieli, M. L. Andersen, I. Joughin, A. Payne, T. L. Edwards, F. Pattyn, and R. S. W. van de Wal (2013), Future sea-level rise from Greenland's main outlet glaciers in a warming climate, *Nature*, *497*(7448), 235-238, doi:10.1038/nature12068.

Nowicki, S. M. J., A. Payne, E. Larour, H. Seroussi, H. Goelzer, W. Lipscomb, J. Gregory, A. Abe-Ouchi, and A. Shepherd (2016), Ice Sheet Model Intercomparison Project

(ISMIP6) contribution to CMIP6, *Geoscientific Model Development*, *9*(12), 4521–4545, doi:10.5194/gmd-9-4521-2016.

O'Leary, M., and P. Christoffersen (2013), Calving on tidewater glaciers amplified by submarine frontal melting, *The Cryosphere*, *7*(1), 119-128, doi:10.5194/tc-7-119-2013.

Paolo, F. S., H. A. Fricker, and L. Padman (2015), Volume loss from Antarctic ice shelves is accelerating, *Science*, *348*(6232), 327-331, doi:10.1126/science.aaa0940.

Pattyn, F. (2003), A new three-dimensional higher-order thermomechanical ice sheet model: Basic sensitivity, ice stream development, and ice flow across subglacial lakes, *Journal of Geophysical Research: Solid Earth*, *108*(B8), 2382, doi:10.1029/2002JB002329.

Pattyn, F. (2010), Antarctic subglacial conditions inferred from a hybrid ice sheet/ice stream model, *Earth and Planetary Science Letters*, *295*(3-4), 451-461, doi:10.1016/j.epsl.2010.04.025.

Pattyn, F. (2017), Sea-level response to melting of Antarctic ice shelves on multi-centennial time scales with the fast Elementary Thermomechanical Ice Sheet model (f.ETISh v1.0), *The Cryosphere Discuss.*, *2017*, 1-52, doi:10.5194/tc-2017-8.

Pattyn, F., and G. Durand (2013), Why marine ice sheet model predictions may diverge in estimating future sea level rise, *Geophysical Research Letters*, *40*(16), 4316-4320, doi:10.1002/grl.50824.

Pattyn, F., C. Schoof, L. Perichon, R. C. A. Hindmarsh, E. Bueler, B. de Fleurian, G. Durand, O. Gagliardini, R. Gladstone, D. Goldberg, G. H. Gudmundsson, P. Huybrechts, V. Lee, F. M. Nick, A. J. Payne, D. Pollard, O. Rybak, F. Saito, and A. Vieli (2012), Results of the Marine Ice Sheet Model Intercomparison Project, MISMIP, *The Cryosphere*, *6*(3), 573-588, doi:10.5194/tc-6-573-2012.

Pattyn, F., L. Perichon, G. Durand, L. Favier, O. Gagliardini, R. C. A. Hindmarsh, T. Zwinger, T. Albrecht, S. Cornford, D. Docquier, J. J. Fürst, D. Goldberg, G. H. Gudmundsson, A. Humbert, M. Hütten, P. Huybrechts, G. Jouvet, T. Kleiner, E. Larour, D. Martin, M. Morlighem, A. J. Payne, D. Pollard, M. Rückamp, O. Rybak, H. Seroussi, M. Thoma, and N. Wilkens (2013), Grounding-line migration in plan-view marine ice-sheet models: Results of the ice2sea MISMIP3d intercomparison, *Journal of Glaciology*, *59*(215), 410-422, doi:10.3189/2013JoG12J129.

Payne, A. J., P. R. Holland, A. P. Shepherd, I. C. Rutt, A. Jenkins, and I. Joughin (2007), Numerical modeling of ocean-ice interactions under Pine Island Bay's ice shelf, *Journal of Geophysical Research: Oceans*, *112*(C10), C10019, doi:10.1029/2006JC003733.

Pelto, M. S., and C. R. Warren (1991), Relationship between tidewater glacier calving

velocity and water depth at the calving front, *Annals of Glaciology*, *15*, 115-118, doi: 10.1017/S0260305500009617.

Pollard, D., and R. M. DeConto (2009), *A coupled ice-sheet/ice-shelf/sediment model applied to a marine-margin flowline: Forced and unforced variations*, pp. 37–52, Blackwell Publishing Ltd., doi:10.1002/9781444304435.ch4.

Pollard, D., and R. M. DeConto (2012a), Description of a hybrid ice sheet-shelf model, and application to Antarctica, *Geosci. Model Dev.*, *5*(5), 1273-1295, doi: 10.5194/gmd-5-1273-2012.

Pollard, D., and R. M. DeConto (2012b), A simple inverse method for the distribution of basal sliding coefficients under ice sheets, applied to Antarctica, *The Cryosphere*, *6*(5), 953–971, doi:10.5194/tc-6-953-2012.

Pollard, D., R. M. DeConto, and R. B. Alley (2015), Potential Antarctic Ice Sheet retreat driven by hydrofracturing and ice cliff failure, *Earth and Planetary Science Letters*, *412*, 112-121, doi:10.1016/j.epsl.2014.12.035.

Pollard, D., W. Chang, M. Haran, P. Applegate, and R. DeConto (2016), Large ensemble modeling of the last deglacial retreat of the West Antarctic Ice Sheet: Comparison of simple and advanced statistical techniques, *Geoscientific Model Development*, *9*(5), 1697–1723, doi:10.5194/gmd-9-1697-2016.

Price, S. F., M. J. Hoffman, J. A. Bonin, I. M. Howat, T. Neumann, J. Saba, I. Tezaur, J. Guerber, D. P. Chambers, K. J. Evans, J. H. Kennedy, J. Lenaerts, W. H. Lipscomb, M. Perego, A. G. Salinger, R. S. Tuminaro, M. R. van den Broeke, and S. M. J. Nowicki (2017), An ice sheet model validation framework for the Greenland ice sheet, *Geoscientific Model Development*, *10*(1), 255–270, doi:10.5194/gmd-10-255-2017.

Pritchard, H. D., and D. G. Vaughan (2007), Widespread acceleration of tidewater glaciers on the Antarctic Peninsula, *Journal of Geophysical Research: Earth Surface*, *112*(F3), F03S29, doi:10.1029/2006JF000597.

Pritchard, H. D., R. J. Arthern, D. G. Vaughan, and L. A. Edwards (2009), Extensive dynamic thinning on the margins of the Greenland and Antarctic ice sheets, *Nature*, *461*(7266), 971-975, doi:10.1038/nature08471.

Pritchard, H. D., S. R. M. Ligtenberg, H. A. Fricker, D. G. Vaughan, M. R. van den Broeke, and L. Padman (2012), Antarctic ice-sheet loss driven by basal melting of ice shelves, *Nature*, *484*(7395), 502-505, doi:10.1038/nature10968.

Radic, V., and R. Hock (2011), Regionally differentiated contribution of mountain glaciers and ice caps to future sea-level rise, *Nature Geosci*, *4*(2), 91-94, doi:10.1038/ngeo1052.

Radic, V., A. Bliss, A. C. Beedlow, R. Hock, E. Miles, and J. G. Cogley (2014), Regional

and global projections of twenty-first century glacier mass changes in response to climate scenarios from global climate models, *Climate Dynamics*, *42*(1-2), 37-58, doi: 10.1007/s00382-013-1719-7.

Ridley, J. K., P. Huybrechts, J. M. Gregory, and J. A. Lowe (2005), Elimination of the Greenland Ice Sheet in a High CO2 Climate, *Journal of Climate*, *18*(17), 3409-3427, doi:10.1175/JCLI3482.1.

Riedl, C., H. Rott, and W. Rack (2004), Recent variations of Larsen Ice Shelf, Antarctic Peninsula, observed by Envisat, *Proc. of the Envisat & ERS Symposium, Salzburg, Austria, 6-10 September 2004 (ESA SP-572, April 2005).*

Rignot, E., and S. S. Jacobs (2002), Rapid bottom melting widespread near Antarctic ice sheet grounding lines, *Science*, *296*(5575), 2020-2023, doi:10.1126/science.1070942.

Rignot, E., and P. Kanagaratnam (2006), Changes in the velocity structure of the Greenland ice sheet, *Science*, *311*(5763), 986-990, doi:10.1126/science.1121381.

Rignot, E., G. Casassa, P. Gogineni, W. Krabill, A. Rivera, and R. Thomas (2004), Accelerated ice discharge from the Antarctic Peninsula following the collapse of Larsen B Ice Shelf, *Geophysical Research Letters*, *31*(18), L18401, doi:10.1029/2004GL020697.

Rignot, E., G. Casassa, S. Gogineni, P. Kanagaratnam, W. Krabill, H. Pritchard, A. Rivera, R. Thomas, J. Turner, and D. Vaughan (2005), Recent ice loss from the Fleming and other glaciers, Wordie Bay, West Antarctic Peninsula, *Geophysical Research Letters*, *32*(7), L07502, doi:10.1029/2004GL021947.

Rignot, E., J. L. Bamber, M. R. van den Broeke, C. Davis, Y. Li, W. J. van de Berg, and E. van Meijgaard (2008), Recent Antarctic ice mass loss from radar interferometry and regional climate modelling, *Nature Geosci*, *1*(2), 106-110, doi:10.1038/ngeo102.

Rignot, E., J. Mouginot, and B. Scheuchl (2011a), Antarctic grounding line mapping from differential satellite radar interferometry, *Geophysical Research Letters*, *38*(10), L10504, doi:10.1029/2011GL047109.

Rignot, E., J. Mouginot, and B. Scheuchl (2011b), Ice flow of the Antarctic ice sheet, *Science*, *333*(6048), 1427-1430, doi:10.1126/science.1208336.

Rignot, E., S. Jacobs, J. Mouginot, and B. Scheuchl (2013), Ice-shelf melting around Antarctica, *Science*, *341*(6143), 266-270, doi:10.1126/science.1235798.

Rignot, E., J. Mouginot, M. Morlighem, H. Seroussi, and B. Scheuchl (2014), Widespread, rapid grounding line retreat of Pine Island, Thwaites, Smith, and Kohler glaciers, West Antarctica, from 1992 to 2011, *Geophysical Research Letters*, *41*(10), 3502-3509, doi: 10.1002/2014GL060140.

Ritz, C., T. L. Edwards, G. Durand, A. J. Payne, V. Peyaud, and R. C. A. Hindmarsh

(2015), Potential sea-level rise from Antarctic ice-sheet instability constrained by observations, *Nature*, *528*(7580), 115-118, doi:10.1038/nature16147.

Rott, H., P. Skvarca, and T. Nagler (1996), Rapid collapse of northern Larsen Ice Shelf, Antarctica, *Science*, *271*(5250), 788-792, doi:10.1126/science.271.5250.788.

Rott, H., W. Rack, P. Skvarca, and H. De Angelis (2002), Northern Larsen Ice Shelf, Antarctica: Further retreat after collapse, *Annals of Glaciology*, *34*(1), 277-282, doi:10.3189/172756402781817716.

Rott, H., W. Rack, and T. Nagler (2007), Increased export of grounded ice after the collapse of northern Larsen Ice Shelf, Antarctic Peninsula, observed by Envisat ASAR, *Geoscience and Remote Sensing Symposium, 2007. IGARSS 2007. IEEE International*, pp. 1174–1176, doi:10.1109/IGARSS.2007.4423013.

Rott, H., F. Müller, T. Nagler, and D. Floricioiu (2011), The imbalance of glaciers after disintegration of Larsen-B Ice Shelf, Antarctic Peninsula, *The Cryosphere*, *5*(1), 125-134, doi:10.5194/tc-5-125-2011.

Rott, H., D. Floricioiu, J. Wuite, S. Scheiblauer, T. Nagler, and M. Kern (2014), Mass changes of outlet glaciers along the Nordensjköld Coast, northern Antarctic Peninsula, based on TanDEM-X satellite measurements, *Geophysical Research Letters*, *41*(21), 8123-8129, doi:10.1002/2014GL061613.

Sasgen, I., H. Konrad, E. R. Ivins, M. R. Van den Broeke, J. L. Bamber, Z. Martinec, and V. Klemann (2013), Antarctic ice-mass balance 2003 to 2012: Regional reanalysis of GRACE satellite gravimetry measurements with improved estimate of glacial-isostatic adjustment based on GPS uplift rates, *The Cryosphere*, *7*(5), 1499-1512, doi:10.5194/tc-7-1499-2013.

Scambos, T., C. Hulbe, and M. Fahnestock (2003), *Climate-induced ice shelf disintegration in the Antarctic Peninsula*, pp. 79–92, American Geophysical Union, doi:10.1029/AR079p0079.

Scambos, T. A., C. Hulbe, M. Fahnestock, and J. Bohlander (2000), The link between climate warming and break-up of ice shelves in the Antarctic Peninsula, *Journal of Glaciology*, *46*(154), 516-530, doi:10.3189/172756500781833043.

Scambos, T. A., J. A. Bohlander, C. A. Shuman, and P. Skvarca (2004), Glacier acceleration and thinning after ice shelf collapse in the Larsen B embayment, Antarctica, *Geophysical Research Letters*, *31*(18), L18402, doi:10.1029/2004GL020670.

Scambos, T. A., T. M. Haran, M. A. Fahnestock, T. H. Painter, and J. Bohlander (2007), Modis-based Mosaic of Antarctica (MOA) data sets: Continent-wide surface morphology and snow grain size, *Remote Sensing of Environment*, *111*(2–3), 242-257, doi:10.1016/j.rse.2006.12.020.

Scambos, T. A., E. Berthier, T. Haran, C. A. Shuman, A. J. Cook, S. R. M. Ligtenberg, and J. Bohlander (2014), Detailed ice loss pattern in the northern Antarctic Peninsula: Widespread decline driven by ice front retreats, *The Cryosphere*, *8*(6), 2135-2145, doi: 10.5194/tc-8-2135-2014.

Schannwell, C., N. E. Barrand, and V. Radić (2015), Modeling ice dynamic contributions to sea level rise from the Antarctic Peninsula, *Journal of Geophysical Research: Earth Surface*, *120*(11), 2374-2392, doi:10.1002/2015JF003667.

Schannwell, C., N. E. Barrand, and V. Radić (2016), Future sea-level rise from tidewater and ice-shelf tributary glaciers of the Antarctic Peninsula, *Earth and Planetary Science Letters*, *453*, 161-170, doi:10.1016/j.epsl.2016.07.054.

Schoof, C. (2007), Ice sheet grounding line dynamics: Steady states, stability, and hysteresis, *Journal of Geophysical Research*, *112*(F3), F03S28, doi:10.1029/ 2006JF000664.

Schoof, C., and R. C. A. Hindmarsh (2010), Thin-film flows with wall slip: An asymptotic analysis of higher order glacier flow models, *The Quarterly Journal of Mechanics and Applied Mathematics*, *63*(1), 73-114, doi:10.1093/qjmam/hbp025.

Schrama, E. J. O., B. Wouters, and R. Rietbroek (2014), A mascon approach to assess ice sheet and glacier mass balances and their uncertainties from GRACE data, *Journal of Geophysical Research: Solid Earth*, *119*(7), 6048-6066, doi:10.1002/2013JB010923.

Shepherd, A., D. Wingham, T. Payne, and P. Skvarca (2003), Larsen Ice Shelf has progressively thinned, *Science*, *302*(5646), 856-859, doi:10.1126/science.1089768.

Shepherd, A., D. Wingham, D. Wallis, K. Giles, S. Laxon, and A. V. Sundal (2010), Recent loss of floating ice and the consequent sea level contribution, *Geophysical Research Letters*, *37*(13), L13503, doi:10.1029/2010GL042496.

Shepherd, A., E. R. Ivins, G. A, V. R. Barletta, M. J. Bentley, S. Bettadpur, K. H. Briggs, D. H. Bromwich, R. Forsberg, N. Galin, M. Horwath, S. Jacobs, I. Joughin, M. A. King, J. T. M. Lenaerts, J. Li, S. R. M. Ligtenberg, A. Luckman, S. B. Luthcke, M. McMillan, R. Meister, G. Milne, J. Mouginot, A. Muir, J. P. Nicolas, J. Paden, A. J. Payne, H. Pritchard, E. Rignot, H. Rott, L. S. Sørensen, T. A. Scambos, B. Scheuchl, E. J. O. Schrama, B. Smith, A. V. Sundal, J. H. van Angelen, W. J. van de Berg, M. R. van den Broeke, D. G. Vaughan, I. Velicogna, J. Wahr, P. L. Whitehouse, D. J. Wingham, D. Yi, D. Young, and H. J. Zwally (2012), A reconciled estimate of ice-sheet mass balance, *Science*, *338*(6111), 1183-1189, doi:10.1126/science.1228102.

Shfaqat, A. K., A. Andy, A. B. Anders, W. John, K. K. Kristian, and H. K. Kurt (2015), Greenland ice sheet mass balance: A review, *Reports on Progress in Physics*, *78*(4), 046801, doi:10.1088/0034-4885/78/4/046801.

Slingerland, R., and L. Kump (2011), *Mathematical modeling of Earth's dynamical systems: A primer*, Princeton University Press.

Straneo, F., G. S. Hamilton, D. A. Sutherland, L. A. Stearns, F. Davidson, M. O. Hammill, G. B. Stenson, and A. Rosing-Asvid (2010), Rapid circulation of warm subtropical waters in a major glacial fjord in East Greenland, *Nature Geosci*, *3*(3), 182-186, doi: 10.1038/ngeo764.

Sun, S., S. L. Cornford, Y. Liu, and J. C. Moore (2014), Dynamic response of Antarctic ice shelves to bedrock uncertainty, *The Cryosphere*, *8*(4), 1561–1576, doi: 10.5194/tc-8-1561-2014.

Sun, S., S. Cornford, R. Gladstone, L. Zhao, and J. Moore (2017), Ice shelf fracture parameterization in an ice sheet model, *The Cryosphere Discussions*, *2017*, 1–23, doi: 10.5194/tc-2017-53.

Taylor, K. E., R. J. Stouffer, and G. A. Meehl (2011), An overview of CMIP5 and the experiment design, *Bulletin of the American Meteorological Society*, *93*(4), 485-498, doi:10.1175/BAMS-D-11-00094.1.

Thoma, M., A. Jenkins, D. Holland, and S. Jacobs (2008), Modelling Circumpolar Deep Water intrusions on the Amundsen Sea continental shelf, Antarctica, *Geophysical Research Letters*, *35*(18), L18602, doi:10.1029/2008GL034939.

Thomas, I. D., M. A. King, M. J. Bentley, P. L. Whitehouse, N. T. Penna, S. D. P. Williams, R. E. M. Riva, D. A. Lavallee, P. J. Clarke, E. C. King, R. C. A. Hindmarsh, and H. Koivula (2011), Widespread low rates of Antarctic glacial isostatic adjustment revealed by GPS observations, *Geophysical Research Letters*, *38*(22), L22302, doi:10. 1029/2011GL049277, l22302.

Thomas, R., E. Rignot, P. Kanagaratnam, W. Krabill, and G. Casassa (2004), Force-perturbation analysis of Pine Island Glacier, Antarctica, suggests cause for recent acceleration, *Annals of Glaciology*, *39*(1), 133-138, doi:10.3189/172756404781814429.

Thomas, R. H., and C. R. Bentley (1978), A model for Holocene retreat of the West Antarctic ice sheet, *Quaternary Research*, *10*(2), 150-170, doi:10.1016/0033-5894(78) 90098-4.

Trusel, L. D., K. E. Frey, S. B. Das, K. B. Karnauskas, P. Kuipers Munneke, E. van Meijgaard, and M. R. van den Broeke (2015), Divergent trajectories of Antarctic surface melt under two twenty-first-century climate scenarios, *Nature Geosci*, *8*(12), 927-932, doi:10.1038/ngeo2563.

Tsai, V. C., A. L. Stewart, and A. F. Thompson (2015), Marine ice-sheet profiles and stability under Coulomb basal conditions, *Journal of Glaciology*, *61*(226), 205-215, doi:10.3189/2015JoG14J221.

Turner, J., T. A. Lachlan-Cope, G. J. Marshall, E. M. Morris, R. Mulvaney, and W. Winter (2002), Spatial variability of Antarctic Peninsula net surface mass balance, *Journal of Geophysical Research: Atmospheres*, *107*(D13), doi:10.1029/2001JD000755.

Turner, J., N. E. Barrand, T. J. Bracegirdle, P. Convey, D. A. Hodgson, M. Jarvis, A. Jenkins, G. Marshall, M. P. Meredith, H. Roscoe, J. Shanklin, J. French, H. Goosse, M. Guglielmin, J. Gutt, S. Jacobs, M. C. I. Kennicutt, V. Masson-Delmotte, P. Mayewski, F. Navarro, S. Robinson, T. Scambos, M. Sparrow, C. Summerhayes, K. Speer, and A. Klepikov (2013), Antarctic climate change and the environment: An update, *Polar Record*, *50*(03), 237-259, doi:10.1017/S0032247413000296.

van de Berg, W. J., M. R. van den Broeke, C. H. Reijmer, and E. van Meijgaard (2006), Reassessment of the antarctic surface mass balance using calibrated output of a regional atmospheric climate model, *Journal of Geophysical Research: Atmospheres*, *111*(D11), D11104, doi:10.1029/2005JD006495.

van den Broeke, M. (2005), Strong surface melting preceded collapse of Antarctic Peninsula ice shelf, *Geophysical Research Letters*, *32*(12), L12815, doi:10.1029/2005GL023247.

van den Broeke, M. R., J. Bamber, J. Lenaerts, and E. Rignot (2011), Ice sheets and sea level: Thinking outside the box, *Surveys in Geophysics*, *32*(4), 495-505, doi:10.1007/s10712-011-9137-z.

Van der Veen, C., and A. Payne (2004), *Modelling land-ice dynamics*, pp. 169–219.

van der Veen, C. J. (1996), Tidewater calving, *Journal of Glaciology*, *42*(141), 375-385, doi:10.3198/1996JoG42-141-375-385.

Van der Veen, C. J. (2013), *Fundamentals of glacier dynamics*, CRC Press.

van Lipzig, N. P. M., J. C. King, T. A. Lachlan-Cope, and M. R. van den Broeke (2004), Precipitation, sublimation, and snow drift in the Antarctic Peninsula region from a regional atmospheric model, *Journal of Geophysical Research: Atmospheres*, *109*(D24), D24106, doi:10.1029/2004JD004701.

van Wessem, J. M., S. R. M. Ligtenberg, C. H. Reijmer, W. J. van de Berg, M. R. van den Broeke, N. E. Barrand, E. R. Thomas, J. Turner, J. Wuite, T. A. Scambos, and E. van Meijgaard (2016), The modelled surface mass balance of the Antarctic Peninsula at 5.5 km horizontal resolution, *The Cryosphere*, *10*(1), 271-285, doi:10.5194/tc-10-271-2016.

Vaughan, D., G. Marshall, W. Connolley, C. Parkinson, R. Mulvaney, D. Hodgson, J. King, C. Pudsey, and J. Turner (2003), Recent rapid regional climate warming on the Antarctic Peninsula, *Climatic Change*, *60*(3), 243-274, doi:10.1023/A:1026021217991.

Vaughan, D. G. (2006), Recent trends in melting conditions on the Antarctic Peninsula

and their implications for ice-sheet mass balance and sea level, *Arctic, Antarctic, and Alpine Research*, *38*(1), 147-152, doi:10.1657/1523-0430(2006)038[0147:RTIMCO]2.0.CO;2.

Vaughan, D. G., and R. Arthern (2007), Why is it hard to predict the future of ice sheets?, *Science*, *315*(5818), 1503-1504, doi:10.1126/science.1141111.

Vaughan, D. G., and C. S. M. Doake (1996), Recent atmospheric warming and retreat of ice shelves on the Antarctic Peninsula, *Nature*, *379*(6563), 328-331, doi:10.1038/379328a0.

Vaughan, D. G., J. L. Bamber, M. Giovinetto, J. Russell, and A. P. R. Cooper (1999), Reassessment of net surface mass balance in Antarctica, *Journal of Climate*, *12*(4), 933-946, doi:10.1175/1520-0442(1999)012⟨0933:ronsmb⟩2.0.co;2.

Velicogna, I., and J. Wahr (2013), Time-variable gravity observations of ice sheet mass balance: Precision and limitations of the GRACE satellite data, *Geophysical Research Letters*, *40*(12), 3055-3063, doi:10.1002/grl.50527.

Velicogna, I., T. C. Sutterley, and M. R. van den Broeke (2014), Regional acceleration in ice mass loss from Greenland and Antarctica using GRACE time-variable gravity data, *Geophysical Research Letters*, *41*(22), 8130-8137, doi:10.1002/2014GL061052.

Vieli, A., and A. J. Payne (2005), Assessing the ability of numerical ice sheet models to simulate grounding line migration, *Journal of Geophysical Research*, *110*(F1), F01003, doi:10.1029/2004JF000202.

Vieli, A., M. Funk, and H. Blatter (2001), Flow dynamics of tidewater glaciers: A numerical modelling approach, *Journal of Glaciology*, *47*(159), 595-606, doi:10.3189/172756501781831747.

Vuuren, D. P., J. Edmonds, M. Kainuma, K. Riahi, A. Thomson, K. Hibbard, G. C. Hurtt, T. Kram, V. Krey, J.-F. Lamarque, T. Masui, M. Meinshausen, N. Nakicenovic, S. J. Smith, and S. K. Rose (2011), The representative concentration pathways: An overview, *Climatic Change*, *109*(1), 5-31, doi:10.1007/s10584-011-0148-z.

Weertman, J. (1974), Stability of the junction of an ice sheet and an ice shelf, *Journal of Glaciology*, *13*(67), 3-11, doi:10.1017/S0022143000023327.

Williams, C. R., R. C. A. Hindmarsh, and R. J. Arthern (2012), Frequency response of ice streams, *Proceedings of the Royal Society of London A: Mathematical, Physical and Engineering Sciences*, *468*, 3285-3310, doi:10.1098/rspa.2012.0180.

Williams, S. D. P., P. Moore, M. A. King, and P. L. Whitehouse (2014), Revisiting GRACE Antarctic ice mass trends and accelerations considering autocorrelation, *Earth and Planetary Science Letters*, *385*, 12-21, doi:10.1016/j.epsl.2013.10.016.

Winkelmann, R., M. A. Martin, M. Haseloff, T. Albrecht, E. Bueler, C. Khroulev, and A. Levermann (2011), The Potsdam Parallel Ice Sheet Model (PISM-PIK) – Part 1: Model description, *The Cryosphere*, *5*(3), 715-726, doi:10.5194/tc-5-715-2011.

Wouters, B., A. Martín-Español, V. Helm, T. Flament, J. M. van Wessem, S. R. M. Ligtenberg, M. R. van den Broeke, and J. L. Bamber (2015), Dynamic thinning of glaciers on the southern Antarctic Peninsula, *Science*, *348*(6237), 899-903, doi:10.1126/science.aaa5727.

Wuite, J., H. Rott, M. Hetzenecker, D. Floricioiu, J. De Rydt, G. H. Gudmundsson, T. Nagler, and M. Kern (2015), Evolution of surface velocities and ice discharge of Larsen B outlet glaciers from 1995 to 2013, *The Cryosphere*, *9*(3), 957-969, doi:10.5194/tc-9-957-2015.

Yang, Q., T. H. Dixon, P. G. Myers, J. Bonin, D. Chambers, M. Van Den Broeke, M. H. Ribergaard, and J. Mortensen (2016), Recent increases in Arctic freshwater flux affects Labrador Sea convection and Atlantic overturning circulation, *Nat Comm*, *7*, 10525.

Yin, J., J. T. Overpeck, S. M. Griffies, A. Hu, J. L. Russell, and R. J. Stouffer (2011), Different magnitudes of projected subsurface ocean warming around Greenland and Antarctica, *Nature Geosci*, *4*(8), 524-528, doi:10.1038/ngeo1189.

Zwally, H. J., J. Li, J. W. Robbins, J. L. Saba, D. Yi, and A. C. Brenner (2015), Mass gains of the Antarctic ice sheet exceed losses, *Journal of Glaciology*, *61*(230), 1019-1036, doi:10.3189/2015JoG15J071.